FVV

FINAL REPORT

1249 | 2021 – Frankfurt am Main

Initiale Vorentflammung

Initial Pre-ignition

Identifikation des Mechanismus zur initialen Vorentflammung mittels Kombination von experimentellen Untersuchungen und Simulation der Tropfenzündung

Identification of the mechanism for initial pre-ignition by a combination of experimental investigations and simulation of drop ignition

Initial Pre-ignition

Project no. 1328

Identification of the mechanism for initial pre-ignition by a combination of experimental investigations and simulation of drop ignition

Final report

Abstract:

In the framework of this research project, the fundamental mechanism of the initial pre-ignition in highly charged gasoline engines was investigated at low engine speeds. In order to get insight into the characteristics of this stochastically occurring, irregular phenomenon, testbed experiments in combination with numerical simulations were conducted. Besides the thermodynamic characterization of the LSPI frequency (LSPI: Low-speed pre-ignition) under varying engine conditions, processes inside the combustion chamber are optically recorded. Additionally, the influence of the liquid fuel on the pre-ignition mechanism is investigated by modifying the engine configuration to CNG operation. Furthermore, the possibility of oil droplet induced ignitions was investigated by supplying lubricating oil to the engine manifold.

In order to investigate the LSPI phenomenon numerically, the thermodynamic conditions inside the combustion chamber are calculated using a 3D-CFD engine model. On top of this, a detailed 11-component fuel surrogate approach was used to investigate the wetting of the combustion chamber walls by the fuel spray. Based on this data, comprehensive numerical studies on oil-droplet-induced ignitions and hot-particle-induced ignitions are carried out.

The performed investigations showed that all initial pre-ignitions are induced by light-emitting surface deposits or flying objects. The areas of deposit formation and detachment events could be correlated with regions of intensive fuel wall wetting. Further on, there was no experimental or simulative evidence of oil-droplet-induced pre-ignitions. In the case of inert particles, numerical studies showed that they were not able to surpass the necessary minimum surface temperature to initiate a pre-ignition within two consecutive cycles.

Based on the results obtained, a fundamental formation mechanism could be synthesized, which suggests that accumulations of oil and fuel in the combustion chamber are processed through multiple combustion processes in such a way that highly reactive deposits can arise. These can be heated up in such a way that they can trigger premature ignition of the mixture directly at the wall or in the gas phase.

The objective of the research project was achieved.

Scope of report:	126 pages, 116 figures, 18 tables, 66 references
Duration:	01.05.2018 – 31.12.2020
Funding organisations:	BMWi / IGF no. 224 EN, FVV Funds, BMVIT and FFG

RTD performers:	Institute of Internal Combustion Engines (IFKM), Karlsruhe Institute of Technology Head: Prof. Dr. sc. techn. Thomas Koch
	Institute of Powertrains and Automotive Technology (IFA), Technische Universität Wien Head: Univ.-Prof. Dipl.-Ing. Dr. techn. Bernhard Geringer
	Institute of Internal Combustion Engines and Thermodynamic (IVT), Graz University of Technology Head: Univ.-Prof. Dipl.-Ing. Dr. techn. Helmut Eichlseder
	Institute of Technical Thermodynamics (ITT), Karlsruhe Institute of Technology Head: Prof. Dr. rer. nat. habil. Ulrich Maas
Research associates / authors:	Thorsten Schweizer, M.Sc. (IFKM) Dr.-Ing. Heiko Kubach (IFKM)
	Dipl.-Ing.Norbert Zöbinger (IFA) Assoc. Prof. Dipl.-Ing. Dr. techn. Thomas Lauer (IFA)
	Dipl.-Ing. Markus Eder (IVT) Dr. techn. Peter Grabner (IVT)
	Dr.-Ing. Robert Schießl (ITT) Dr. Chien Chia Liu (ITT)
Project user committee chair:	Dipl.-Ing. Albert Breuer (Ford-Werke GmbH)
Scientific advisory committee chair:	Dr.-Ing. Ekkehard Pott (Volkswagen AG)
Related reports:	R597 (2021)

Acknowledgement

This report is the scientific result of a research project undertaken by the FVV (The Research Association for Combustion Engines eV) and performed by the Institute of Internal Combustion Engines (IFKM) at Karlsruhe Institute of Technology under the direction of Prof. Dr. sc. techn. Thomas Koch, the Institute of Powertrains and Automotive Technology (IFA) under the direction of Univ.-Prof. Dipl.-Ing. Dr. techn. Bernhard Geringer at Technische Universität Wien, the Institute of Internal Combustion Engines and Thermodynamic (IVT) under the direction of Univ.-Prof. Dipl.-Ing. Dr. techn. Helmut Eichlseder at Graz University of Technology and the the Institute of Technical Thermodynamics (ITT) at Karlsruhe Institute of Technology under the direction of Prof. Dr. rer. nat. habil. Ulrich Maas.

The FVV and the AC-Styria mobility cluster would like to thank Professors Koch, Geringer, Eichlseder and Maas and their scientific assistants – M.Sc. Thorsten Schweizer, Dr.-Ing. Heiko Kubach (all IFKM), Dipl.-Ing. Norbert Zöbinger and Assoc.Prof. Dipl.-Ing Dr.techn. Thomas Lauer (all IFA), Dipl.-Ing. Markus Eder, Dr. techn. Peter Grabner (all IVT), Dr.-Ing. Robert Schießl, Dr. Chien Chia Liu, (all ITT) – for the implementation of the project. Special thanks are due to the AiF (German Federation of Industrial Research Associations eV) and FFG (Austria Research Promotion Agency) for funding the project within the framework of the collective research networking (CORNET) programme. The project was conducted by an expert group led by Dipl.-Ing. Albert Breuer (Ford-Werke GmbH). We gratefully acknowledge the support received from the chairman and all members of the project user committee. The presented computational results of Technische Universität Wien have been achieved using the Vienna Scientific Cluster (VSC).

In addition, we would like to thank Ford-Werke GmbH for the provision of test engines, KS Kolbenschmidt GmbH for the provision of pistons, Fuchs Schmierstoffe GmbH for the provision of engine oil, Coryton Advanced Fuels Ltd. for the provision of LSPI fuel, OMV for the provision of RON95 fuel, IoLiTec for the provision of ionic liquids, NAGEL Maschinen- und Werkzeugfabrik GmbH for the cylinder honing and Siemens for the provision of CFD simulation licenses.

The research was carried out in the framework of the industrial collective programme (IGF/CORNET no. 224 EN). It was supported by the Federal Ministry for Economic Affairs and Energy (BMWi) through the AiF (German Federation of Industrial Research Associations eV) based on a decision taken by the German Bundestag. The work of the Technische Universitäten Graz and Wien was funded by the Federal Ministry of Transport, Innovation and Technology (BMVIT) through the Austria Research Pro-motion Agency (FFG, grant number 865261).

Supported by:

Federal Ministry for Economic Affairs and Energy

on the basis of a decision by the German Bundestag

AiF Forschungsnetzwerk Mittelstand

IGF Industrielle Gemeinschaftsforschung

FVV Research Association for Combustion Engines

Table of contents

1 Executive summary

1.1 Executive summary (EN)

The overall research objective of the project is the explanation of the fundamental mechanism leading to initial pre-ignitions in highly boosted gasoline engines at low engine speeds. In order to get insight into the stochastic irregular combustion phenomenon, experimental investigations and accompanying numerical studies are carried out.

The testbed investigations are performed at the Institute of Internal Combustion Engines and Thermodynamic (IVT) at the Graz University of Technology, focusing on the thermodynamic and hardware parameter variations as well as sources of oil entrainment and at the Institute of Internal Combustion Engines (IFKM) at Karlsruhe Institute of Technology focusing on the optical pre-ignition characterization and additional key experiments. The accompanying numerical studies are carried out at the Institute of Powertrains and Automotive Technology (IFA) at the Technische Universität Wien and at the Institute of Technical Thermodynamics (ITT) at Karlsruhe Institute of Technology. The focus of the investigation at the ITT was modeling the oil-fuel droplet-induced ignition on a microscopic scale. Whereas the development of a CFD-model to determine the ignition risk of stochastic released objects was the aim at IFA. Additionally, the possibility of hot particle-induced ignitions was investigated.

With this holistic approach, a broad data basis was achieved and enabled the synthesis of a fundamental mechanism explaining the initial pre-ignition phenomenon. As a result, efficient pre-ignition prevention strategies could be derived.

As a first step, a thermodynamic pre-ignition characterization was performed to identify critical oil and fuel parameters and engine operation modes. The investigations showed that the used lubricating oil had a significant impact on the pre-ignition frequency. Furthermore, engine operation modes that enhanced the fuel spray/ liner interaction, as well as an elevated air-fuel-ratio, increased the pre-ignition frequency. Overall, the pre-ignition promoting parameters confirms the data reported in the literature. The wave-like occurrence of pre-ignition events during the engine operation suggested a multi-cyclic developing process. The gained knowledge and data were the basis for the subsequent optical Investigation and key experiments as well as the accompanying simulations.

The optical pre-ignition characterization revealed that the ignition initiation was caused either by glowing objects moving inside the combustion chamber or, in rarer cases, by light-emitting deposits on the in-cylinder walls. These flying objects are most likely solid substances since rebounds from the intake valve could be observed. The appearance of differences in glowing intensity and the observation of glowing particles during the intake stroke indicates a chemical reactivity. Additionally, a dynamic deposit formation behavior was observed, especially in regions of pronounced fuel spray/ liner interaction. This suggests a correlation between liquid film formation and pre-ignition frequency. As a result, the optical investigations extended the knowledge gained in the thermodynamic characterization process. Further on, there was no evidence of a droplet-induced pre-ignition.

Key experiments are performed to get further insight into the initiation mechanism. The modification to the CNG operation confirmed the influence of the spray/ wall interaction. No PI events could be detected while operating on gaseous fuel. By using a light-induced fuel fluorescence tracking method, the areas of deposit formation can be correlated with fuel wall-wetted regions. No droplet ignitions could be observed. The introduction of lubricating oil into the manifold could not trigger a droplet-induced PI. Although, a multi-cycle deposit formation process was observed. In the following, these deposits initiated the pre-ignition. The occurrence of glowing particles during the expansion phase and the air-fuel-ration influence confirms the assumption of reactive particles. The increased partial pressure of oxygen enhances the particle’s reactivity.

Finally, inorganic substances coming from lubricating oil additives on the reactivity of deposits are analyzed using a chemical characterization. Deposits formed from lubricating oil showed a higher reactivity compared to deposits formed from gasoline.

In order to determine the thermodynamic conditions inside the combustion chamber, a 3D-CFD engine model was established and calibrated by using measurement data. An 11-component fuel surrogate model was developed to analyze the mixture preparation and possible fuel wall-wetting. By using this model, an interaction between the liquid fuel and the lubricating oil was confirmed. The location of fuel-wetted regions could be correlated with areas on the liner and piston top land. At these positions, reactive deposits could be found.

A statistical object release approach was established and implemented into the CFD engine model to describe the experimentally observable detachments based on the previous modeling activities. The properties of the released parcels were set according to oil droplets or solid particles, depending on the investigations' objective. The post-processed histories were coupled with the detailed two-phase ignition sub-models.

No droplet-induced pre-ignitions could be found under the investigated thermodynamic conditions. Even the consideration of accumulated semi-stable intermediates, like Ketohydroperoxides, could not accelerate the reactivity enough to trigger a PI. In the case of carbon-based particles, the minimum surface temperature to ignite ambient gas was not reached during two consecutive engine cycles. This result is in agreement with the experimental investigations and leads to the requirement of reactive particles.

Based on the experimentally and numerically obtained results, a fundamental pre-ignition mechanism could be synthesized. This mechanism suggests the accumulation and generation of deposits over several engine cycles based on partially oxidized fuel and lubricating oil. As a result, highly reactive detachments or deposits were formed, which can surpass the necessary minimum surface temperature during the compression phase.

1.2 Executive Summary (DE)

Im Rahmen dieses Forschungsvorhabens wurden die grundlegenden Entstehungsmechanismen von (initialen) Vorentflammungen an hochaufgeladenen Ottomotoren bei niedrigen Motordrehzahlen untersucht. Zur Entschlüsselung dieses Phänomens stochastisch auftretender, irreguläre Verbrennungsvorgänge wurden Untersuchungen am Motorenprüfstand sowie begleitende numerische Studien durchgeführt.

Die experimentellen Motorversuche fanden am Institut für Verbrennungskraftmaschinen und Thermodynamik (IVT) der Technischen Universität Graz mit dem Fokus auf thermodynamischen/ Hardware Parametervariation und Brennraumöleintragungsquellen sowie am Institut für Kolbenmaschinen (IFKM) des Karlsruher Institut für Technologie mit dem Fokus auf optischen Vorentflammungscharakterisierungen und ausgewählten Schlüsselexperimenten statt.

Die begleitenden simulativen Untersuchungen wurden am Institut für Fahrzeugantriebe und Automobiltechnik (IFA) der Technischen Universität Wien sowie am Institut für Technische Thermodynamik (ITT) des Karlsruher Institut für Technologie durchgeführt.

Der Schwerpunkt der Modellierung am ITT lag in der mikroskopischen Beschreibung der Öl-Kraftstoff-induzierten Zündung.

Am IFA wurde der Fokus auf die Entwicklung eines CFD-Modells gelegt, dass das Zündrisiko von stochastisch abgelösten Objekten ermittelt. Weiters wurde die Möglichkeit der Zündung an festen Partikeln näher beleuchtet.

Mit diesem ganzheitlichen Ansatz wird eine große Ergebnisbasis geschaffen auf Grundlage derer eine effiziente Mechanismus-Synthese stattfindet. Folgend können gezielte Vorentflammungs-Vermeidungsstrategien entwickelt werden.

In einem ersten Schritt wurde eine thermodynamische Vorentflammungscharakterisierung der Versuchsträger zur Identifikation von vorentflammungskritischen Motorbetriebsmedien (Kraftstoff + Öl) und Motorparameterausprägungen vorgenommen. Es zeigt sich ein überproportionaler Öleinfluss auf das Vorentflammungsauftreten. Motorparameterausprägungen, welche zu einer erhöhten Kraftstoffstrahl/ Zylinderwandinteraktion führen, zeigen die größte Wahrscheinlichkeit für das Auftreten von Vorentflammungen. Überdies zeigt eine Anhebung des Verbrennungsluftverhältnis einen signifikanten negativen Einfluss auf das Vorentflammungsgeschehen. Insgesamt konnten aus der Literatur bekannte Vorentflammungstendenzen an den Versuchsträgern bestätigt werden. Ein wellenartiges Vorentflammungsauftreten innerhalb einzelner Versuchsreihen lässt auf einen multizyklischen Entstehungsprozess schließen. Die Untersuchungen stellen die Ausgangsbasis für die anschließenden optischen Charakterisierungen und Schlüsselexperimente sowie die begleitenden Simulationen dar.

Optischen Vorentflammungscharakterisierungen zeigen die Initiierung von Vorentflammungen bei allen untersuchten Motorparameterausprägungen entweder durch sich im Brennraum bewegende glühende Objekte oder in selteneren Fällen durch lichtemittierende Ablagerungen. Das Abprallen dieser Objekte an den Einlassventilen lässt auf eine partikelartige festere Substanz schließen. Ein deutlich unterschiedliches Glühverhalten dieser Partikel bedingt die Annahme von unterschiedlichen Partikeleigenschaften. Glühende Partikel in kalten Zyklusphasen legen einen reaktiven Charakter nahe. Zusätzlich wird ein sehr dynamisches Ablagerungsbildungsverhalten insbesondere bei Kraftstoffstrahl/ Zylinderwandinteraktionsstellen in Korrelation zur Vorentflammungshäufigkeit beobachtet. Damit konnten die Annahmen aus den thermodynamischen Charakterisierungen bestätigt und erweitert werden. Es zeigt sich keine Evidenz für eine direkte Tropfenzündung.

Gezielte Schlüsselexperimente vertiefen das Prozessverständnis. Der Motorbetrieb mit CNG ohne Vorentflammungsereignisse bestätigt den Zusammenhäng von Kraftstoffstrahl/ Zylinderwandinteraktion und Vorentflammungsauftreten. Durch lichtinduzierte Kraftstofffluoreszenzverfolgung kann die beobachtete Ablagerungsbildung mit den spezifischen Kraftstoffstrahl/ Zylinderwandinteraktionsstellen korreliert werden. Auch bei Untersuchungen mit zusätzlicher Öleindosierung in spezifische Zylinder konnte keine Tropfenzündung beobachtet werden. Allerdings kann ein multizyklischer Ablagerungsprozess mit anschließender Vorentflammungsinitiierung durch Oberflächenzündung beobachtete werden. Das überproportionale Auftreten glühender Partikel in den Expansionsphasen bestätigt die Annahme reaktiver Partikel. Auch der starke Verbrennungsluftverhältniseinfluss auf die Vorentflammungshäufigkeit wird durch die Beobachtung glühender Partikel während der Verbrennung erklärbar. Das Oxidationsverhalten wird hierbei maßgeblich durch die Sauerstoffverfügbarkeit bestimmt. Finale Ablagerungscharakterisierungen von spezifischen Brennraumpositionen können mit Ölreferenzablagerungen korreliert werden und es zeigt sich ein eindeutiger Zusammenhang zwischen Vorentflammungsauftreten und Oxidations-Reaktivitäten von spezifischen Ablagerungen.

Auf Basis der experimentellen Messdaten wurde die thermodynamischen Bedingungen im Brennraum mithilfe eines 3D-CFD Motormodells ermittelt. Um die Gemischaufbereitung und die Benetzung der Brennraumwände durch das Kraftstoffspray möglichst genau abbilden zu können, wurde ein 11-Komponenten Kraftstoffmodell entwickelt und eingesetzt. Mit diesem Modell konnte der Einfluss der Interaktion zwischen flüssigen Kraftstoff und dem Schmieröl nachgewiesen werden. Die kraftstoffbenetzten Regionen an der Zylinderwand korrelierten eindeutig mit der experimentell beobachtbaren Bildung reaktiver Ablagerungen am Kolbenboden sowie an der Zylinderwand selbst.

Ausgehend von diesen Untersuchungen wurde ein CFD-Modell entwickelt, dass die experimentell beobachtbaren Ablösungen von Objekten im Rahmen eines statistischen Ansatzes beschreibt. Die Eigenschaften der Objekte wurden abhängig vom Untersuchungsziel als Öltropfen oder als feste Partikel beschrieben. Die damit gewonnen Objekthistorien wurden anschließend mit den detaillierten Submodellen zur Zweiphasen-Zündung gekoppelt.

Unter den untersuchten thermodynamischen Randbedingungen konnte numerisch keine öltropfeninduzierte Zündung nachgewiesen werden. Selbst unter der Berücksichtigung von semi-stabilen reaktiven Zwischenprodukten, wie Ketohydroperoxide, war keine

Vorentflammung möglich. Im Fall von inerten kohlenstoffbasierten Partikeln konnte gezeigt werden, dass die notwendige minimale Oberflächentemperatur innerhalb zwei aufeinanderfolgender Zyklen nicht erreicht werden konnte.

Dies steht im Konsens mit den experimentellen Erkenntnissen und untermauert die Bedingung nach reaktiven Partikeln als Auslöser von Vorentflammungen.

Basierend auf den experimentell sowie simulativ erzielten Ergebnissen konnte ein grundlegender Entstehungsmechanismus synthetisiert werden, der nahelegt, dass im Brennraum befindliche Ansammlungen von Öl und Kraftstoff durch mehrfache Verbrennungsvorgänge so aufbereitet werden, dass hochreaktive Ablagerungen entstehen können. Diese erreichen während der Kompressionsphase eine ausreichend hohe Temperatur, sodass sie direkt an der Wand oder auch als fliegende glühende Objekte in der Gasphase zu einer vorzeitigen Gemischentflammung führen können.

2 Introduction

This project was developed as a cooperative project between four university institutes, funded by the "The Research Association for Combustion Engines eV" (FVV). The investigation's primary goal was to find a holistic explanation about low-speed-pre-ignition (LSPI), which mainly occur in highly supercharged direct-injection gasoline engines at low engine speed.

The concept of downsizing is a successful approach to solve the conflict between efficiency and emission behavior of SI engine drive units for passenger cars. This leads to highly charged SI engines with direct injection and high specific power densities. These boundary conditions promote a stochastic combustion anomaly known as low-speed pre-ignition (LSPI), particularly in the high-load and low-speed ranges. This complex multi-cycle phenomenon, which is not yet understood in its entirety, limits further efficiency gains. Only with a comprehensive understanding of the mechanism behind pre-ignitions can countermeasures be targeted and further efficiency gains achieved.

With the reduction of the displacement and/or decreasing of the number of cylinders with simultaneously forced induction, considerable advantages can be achieved in the degree of efficiency [1]. This technology could provide a significant contribution in reaching the ambitious targets set for an average CO_2 emission level from car engines of 95 g/km by 2020. This and the additional lowering of the fuel consumption are required in order to continue to maintain combustion engines as an accepted power source, especially in the context of electrification. However, the so-called degree of downsizing is mainly limited by the occurrence of combustion anomalies such as knocking and pre-ignitions. In particular, the latter are critical, as their occurrence, on the one hand, is distributed stochastically and, as a result, cannot be managed by means of control technology. On the other hand, the very high peak pressures experienced during a pre-ignition can possibly lead to engine damage. In order to prevent such damage, the theoretical potential of downsizing cannot be fully exploited.

These so-called pre-ignitions cannot always be clearly distinguished from surface ignitions. These are to be understood as self-ignitions before the ignition by the spark plug, which, however, differ from the surface ignition in regard to the ignition mechanism. Depending on the surface ignition time, this can result in extreme knocking with extremely high pressure-gradients and peak pressures (> 350 bar), which can lead to a quick or even spontaneous damaging of the engine. Often damages are observed at the first piston ring [2].

Pre-ignitions occur distributed stochastically and unpredictably. The frequency strongly depends on the boundary conditions. Frequently, values in the range of 5 to 30 pre-ignitions per 10,000 cycles are specified [3]. In this, pre-ignitions either occur as individual events or in so-called series. In the process, either several pre-ignitions can occur consecutively or – which is more often the case – an “initial” first pre-ignition is followed by a normal combustion, and then several times alternately, a pre-ignition is followed by a normal combustion. In the determination of the triggering mechanisms, a distinction must be made between the initial pre-ignition and the so-called subsequent pre-ignitions.

With the use of optical measurements, several publications show that due to the initial pre-ignition, deposits are flaked off, and subsequently, a high number of particles are present in the combustion chamber [1] [4]. A part of these particles can remain in the combustion chamber after the charge exchange process and heat up strongly during the next normal combustion. When these particles remain present in the combustion chamber after a renewed charge exchange process, they can cause an ignition during the next cycle [6]. A number of papers make the assumption that no solid deposits are loosened, but instead, oil is separated from the top land area in particular and burnt during the expansion phase. Most lubricating oils contain calcium in the form of CaCO3 as an additive, which is split up into CaO and CO2 during the hot expansion phase. During the compression phase of the next cycle, CaO can react with

CO2 in an exothermic reaction and trigger a pre-ignition. It is not necessary in this regard that a normal combustion occurs between two pre-ignitions [6].

The situation is more complex during the initial pre-ignitions. Current knowledge suggests that a pure gas-phase ignition, for example, due to inhomogeneities in the combustion chamber, is unlikely. This is shown both in the reaction-kinetic calculations by Schießl as well as in experiments by Dahnz from the FVV project "*Vorentflammung I und II*" (Pre-ignition I and II). In the event tree prepared there, the assumption is made that it is a two-phase phenomenon [7]. According to this, liquid or solid particles are involved in self-ignition. In regard to liquid particles, various studies show a dependency of the pre-ignition frequency on the lubricating oil, in which both base oils, the additive as well as the dilution with fuel are critical. Because solid particles or deposits also depend on the fuels and lubricants, in this regard, an indirect dependency of the pre-ignition on the system of lubricating oil/fuel must be noted here.

Due to the fact that oil has a higher ignition propensity than fuel, under certain conditions, self-ignition can occur at such a droplet [7] [8] [9]. However, this is counteracted by the vaporization on the droplet surface because the enthalpy of vaporization causes local cooling. Takeuchi and Luef [10] [11] have performed extensive studies on the influence of the base oil composition and additives. It emerged that in particular low viscosities and high calcium content benefit the pre-ignition rate. The low viscosity promotes the detachment of oil droplets. The influence of calcium has not been clarified yet. According to Moriyoshi [6], a chemical conversion into an exothermic reaction may be responsible. Luo et al. also describe the influence of oil on the turbocharger lubrication and the crankcase ventilation on pre-ignition [12].

Direct proof of oil droplet ignition, e.g. by visualization, has not been published yet. However, many papers report on the dependency of the pre-ignition rate of the fuel-oil interaction [3] [12] [13] [14] [15]. For example, the deposition of fuel on the cylinder wall varies with fuel injection timing. The mixture of fuel with lubricating oil differs from pure fuel in both its chemical as well as its physical properties. The rare occurrence of the pre-ignition is explained thus: The deposit in the top land must first build up again following a pre-ignition that has taken place.

Modeling studies on chemical kinetics which were performed in the preceding phase, suggest a chemical change of the oil as the cause of the pre-ignition. In particular, these investigations show that under the conditions of the quasi-periodical heating up and cooling down in the top land, extremely reactive substances can be formed by chemical conversion from poorly ignitable substances with advancing time. The chemical mechanism for this is the temporary formation of radicals in high-temperature phases, which recombine during the subsequent low-temperature phases, in the course of which other substances are formed as source materials. This means that the engine itself can potentially create substances that can trigger pre-ignitions and also form deposits (e.g. in the top land) of such highly reactive substances. For example, keto-hydroperoxides form a class of such substances.

During LSPI, a sequence of coupled, interacting chemical and physical processes occurs. A source of auto-ignition is required, and the ignited region must evolve into a self-propagating flame before top dead center is reached. Different scenarios are plausible explanations for the occurrence of auto-ignition.

Figure 2-1 summarizes phenomena that might be underlying mechanisms of LSPI in the form of a tree structure. These tree-structures help to collect the broad spectrum of empirical findings, as well as numerous results from modeling studies, and arrange them into a system endowed with a logical structure; e.g., one branch can only be put in a causal relationship to LSPI if one of its sub-branches can.

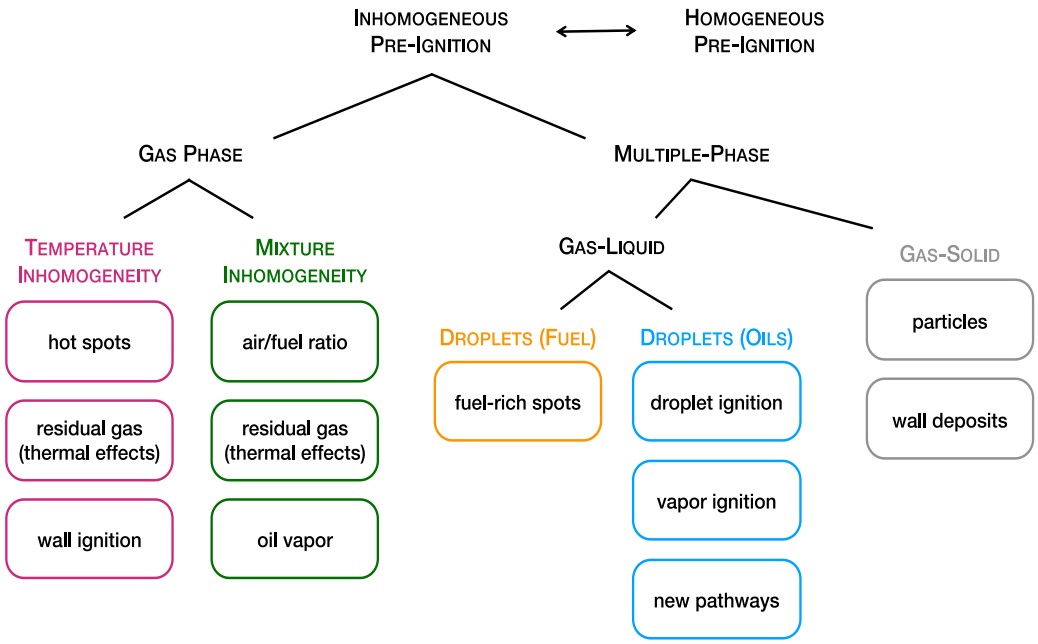

Figure 2-1:Classification tree of putative mechanisms underlying pre-ignition.

This strategy can provide physics-based support for an understanding of the LSPI phenomenon and aids the interpretation for experimental observations and engine CFD simulations.

The results of previous projects, which also studied the causes of the LSPI phenomenon, were carefully checked together with an updated, expanded literature review. A good level of background knowledge was acquired at the start of the current period.

3 Investigation methodologies

In the following, the common overall project structure is introduced. From this, the specific methodologies of the individual research units are presented to address the individual project objectives.

3.1 Project structure

The project was performed as cooperation between four university institutes. The main goal of the investigations was to define a holistic explanation about low-speed-pre-ignitions (LSPI) with a combination of experimental tests on the testbed and simulative investigation. The experimental investigations were divided between the two institutes, the IFKM in Karlsruhe and the IVT in Graz. The simulative investigations included 1D process- and 3D CFD-simulations by the IFA as well as physical and chemical reaction simulations about the droplet gas interaction by the ITT.

Figure 3-1 shows the thematic distribution of the specific questions among the individual research institutes as well as the flow of information to the fundamental pre-ignition (PI) mechanism exploration.

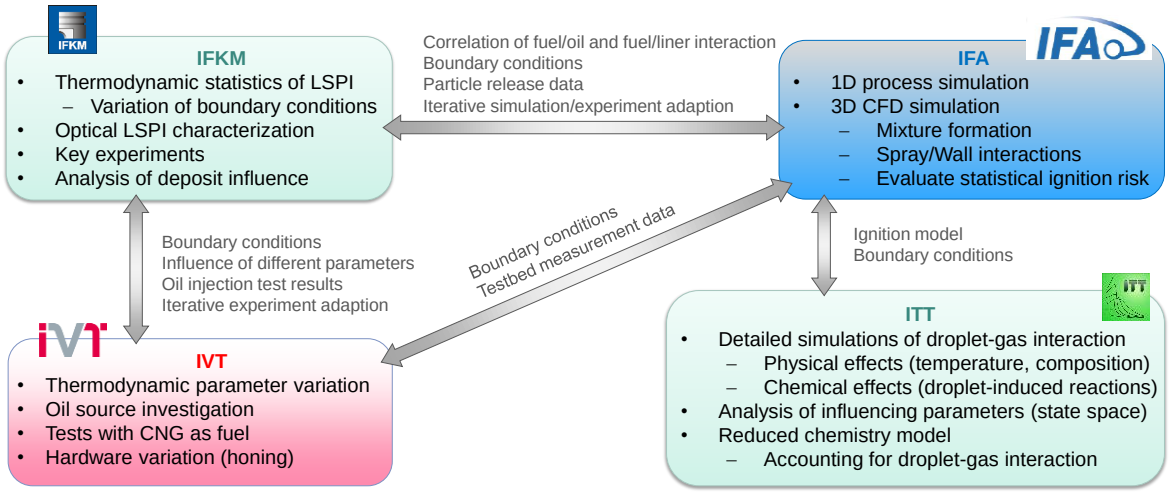

Figure 3-1: Project structure initial pre-ignition.

3.2 IVT investigation methodology

A part of the investigations on the testbed has been carried out together with the IFKM in Karlsruhe. For this reason, there are overlaps in the content of some test methods in the following chapters.

3.2.1 LSPI detection

In gasoline engines, different combustion anomalies are detected. In Figure 3-2, the most common combustion anomalies are shown in comparison to regular combustions. The regular combustion is shown as a grey dashed curve. The orange cylinder pressure curve shows a knocking combustion cycle, and the black curve shows a pre-ignition cycle. The center of gravity (MFB) of pre-ignition combustion cycles is shifted forward compared to regular combustion cycles. The maximum cylinder pressure of pre-ignition cycles can reach a high level because, in this case, the combustion starts before the piston has reached the top dead center (TDC). The challenge was to find a methodology to detect pre-ignitions and differentiate them from other combustion anomalies.

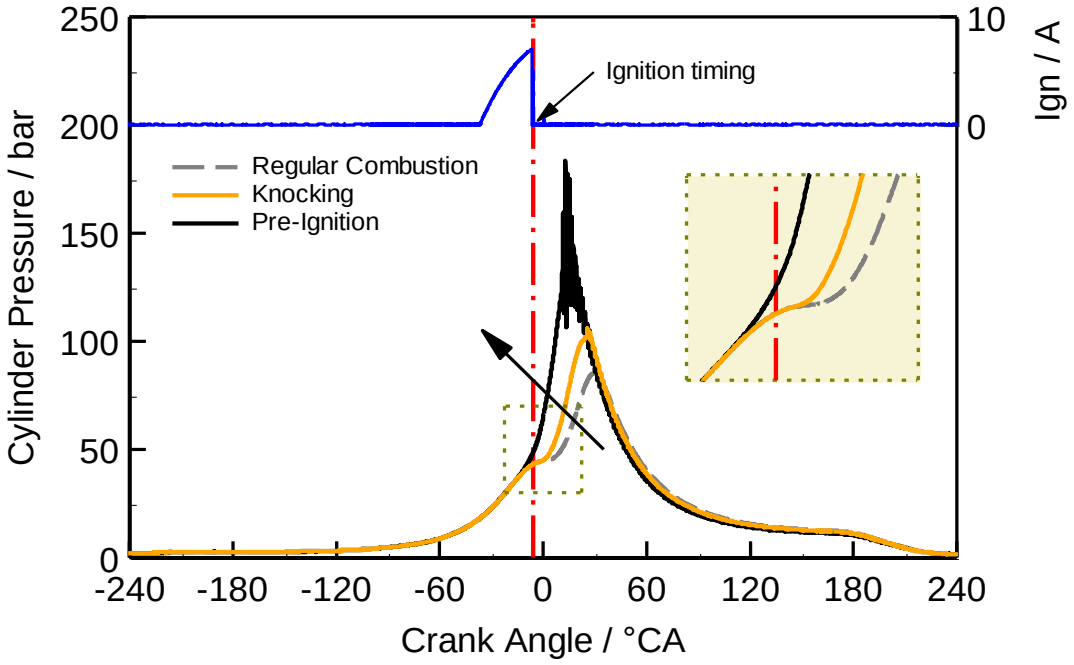

Figure 3-2: Cylinder pressure signal of combustion phenomena [16].

To detect all LSPI events reliably, we used an automated pre-ignition detection on the testbed as a first step methodology. Therefore, the indication system's function was used to observe combustion relevant parameters online during the measurements. With this function, combustion cycles, which exceed thresholds of cylinder pressure or knock peaks, were stored automatically with their pre-and post-history. The trigger borderline for cylinder pressure was set at 140 bar and the knocking peak pressure at 1.5 bar.

Afterward, these stored combustion anomalies have been post-processed with an automated tool to separate pre-ignition from knocking events, shown in the diagrams below. The evaluation method is based on the detection of outliers in the recorded cycle data. With this evaluation, the parameters maximum cylinder pressure ($p_{cyl\ [max]}$) mass fraction burned ($MFB_{5\%}$) and cylinder pressure at ignition ($p_{cyl\ [IG]}$) have been monitored. For each parameter, the stored 260 cycles were statistically evaluated. Because we assumed normal distribution for these parameters with $\mu+3\sigma$, the pre-ignition cycle can be detected reliably between the lower and upper border. If two criteria for one combustion anomaly were met in the post-processing, the cycle counted as an LSPI event. In the beginning, we reviewed this evaluation process also with

other combustion parameters like mass fraction burned of 1% and 5%. All parameters returned the same result, so we focused on p_{cyl} and MFB 5% for further investigations.

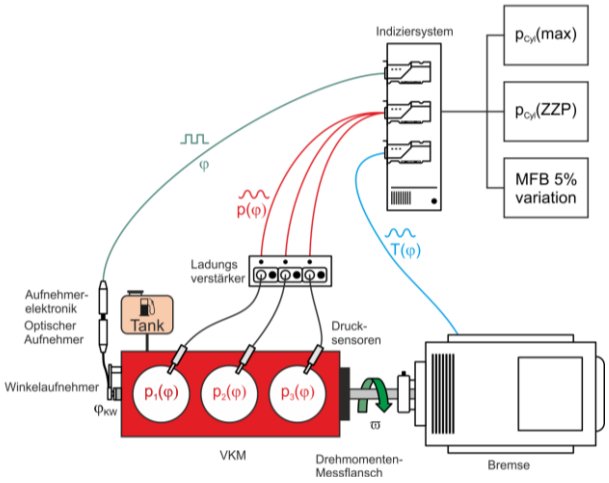

Figure 3-3: Indication System to detect pre-ignitions.

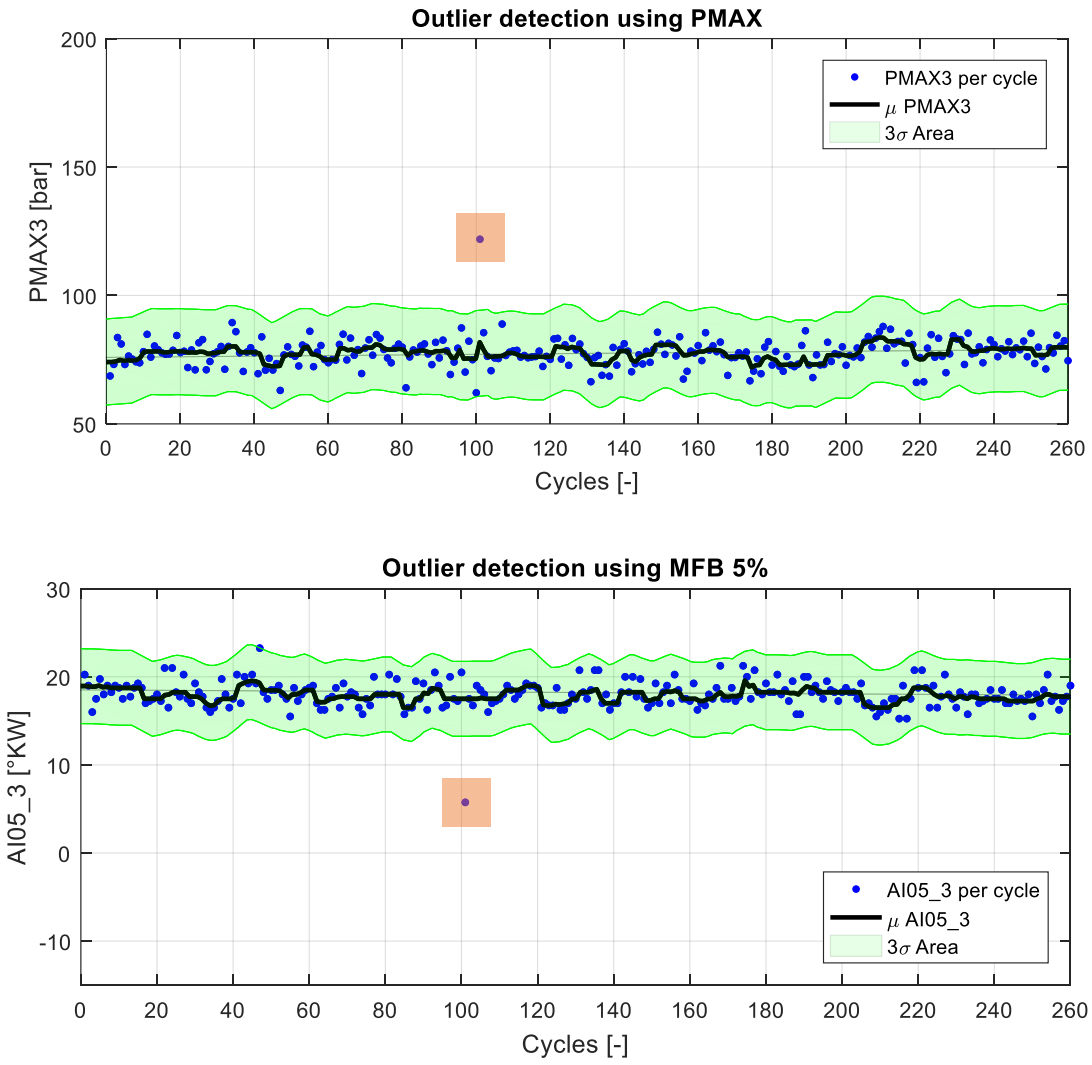

Figure 3-4: Post-processing for pre-ignition cycles.

3.2.2 Parameter variation

The first work package includes a thermodynamic parameter variation. We tried to find a thermodynamic parameter setting with a relatively constant and reproducible number of pre-ignitions. For these variations, we investigated the influence of different parameters, shown in Table 3-1, on their effect on the occurrence of low-speed-pre-ignitions.

Table 3-1: Variation parameters.

Parameter	Variation
engine speed	1400rpm - 2000rpm
engine load	19bar - 25bar BMEP
ignition timing	Spark sweep
start of injection	330°CA BTDC - 250°CA BTDC
intake air temperature	30°C - 60°C
coolant temperature	70°C - 100°C
fuel temperature	20°C - 40°C
fuel injection pressure	10MPa - 20MPa

For the parameter variation, we defined a number of cycles, which have to be measured during the test sequence. The measuring time has been adjusted to match a cycle number of 30.000 cycles depending on the engine speed. The number of 30.000 cycles has been chosen to increase the test engine's durability and increase the lifetime of the optical investigation equipment in Karlsruhe. The measuring time for different engine speeds, shown in Table 3-2, was calculated with:

$$measuring\ time = \frac{2\ x\ cycle\ number}{engine\ speed}\ [min]$$

Table 3-2: Measuring duration for investigated engine speeds.

Engine speed [min^{-1}]	**Cycles [#]**	**Measuring time**
1500	**30 000**	**40 min**
1600	**30 000**	**38 min**
1700	**30 000**	**35 min**
1800	**30 000**	**33 min**
1900	**30 000**	**31 min**
2000	**30 000**	**30 min**
2300	**30 000**	**26 min**

Before we started the measurement sequence for each parameter variation, a conditioning phase of 10 minutes was performed. During this conditioning phase, the ignition timing was changed to slightly knocking combustion behavior to remove contaminations in the combustion chamber. Also, the engine load was decreased during the conditioning phase to protect the hardware, especially at low engine speeds. Subsequently, the pre-ignition testing was executed with the given parameter settings. The results of these investigations are shown in chapter results.

3.2.3 Oil injection

To test the effects of different substances on their tendency to pre-ignite, we have chosen an experimental setup with which these different liquids can be compared in a reasonable time frame. We also used this experimental setup at the beginning of the LSPI investigations to provoke pre-ignitions at operation points with low LSPI decency. We started to compare different engine oils with this injection system on their LSPI behavior to find our basic setup. Information regarding the positioning of the oil dosing system is shown in chapter 4.1.3.

Initially, we had to define a methodology for the oil injection tests. Therefore, during the commissioning phase, we increased the oil amount at a specified operating point until LSPI's could be detected. So we found an oil amount that reliably leads to pre-ignitions. With this specified oil injection mass flow, the different oil probes were compared with the same test methodology.

$$\dot{m}_{OIL}\left[{}^{g}/_{h}\right] = \boldsymbol{OIL_{consumption}}\left[{}^{g}/_{\boldsymbol{kWh}}\right] \times \boldsymbol{P_e}\,[\boldsymbol{kW}]$$

Example:

$$0{,}45\ {}^{g}/_{kWh} \times 38{,}7\ kW = 11{,}61\ {}^{g}/_{h} = 0{,}29\ {}^{g}/_{min}$$

$$\mathbf{0{,}22}\ \boldsymbol{ml}/_{\boldsymbol{min}}\ with\ \varrho_{Oil} \sim \mathbf{0{,}85}\ \ {}^{\boldsymbol{g}}/_{\boldsymbol{cm^3}}$$

Using the equation below for an engine power of 38.7 kW, the dosing system has to be set to a mass flow of 0.19 g/min to reach an oil consumption of 0.45 g/kWh through the intake system. With this calculation, the oil amount was adapted to different operating points during the injection tests.

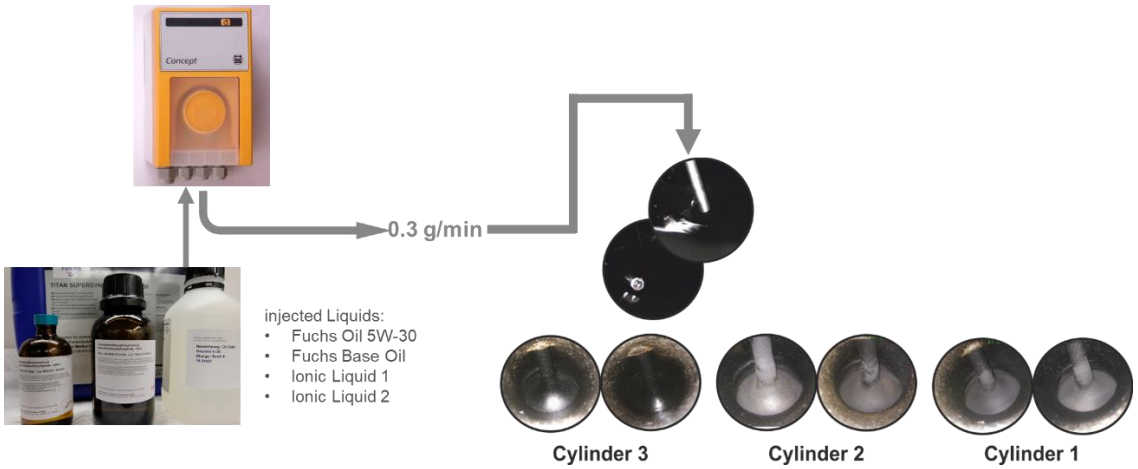

Figure 3-5: Oil dosing methodology.

The tested lubricants were the standard engine oil Fuchs 5W-30, a base oil with fewer additives and ionic liquids. The two ionic liquids used for the injection tests are described in Table 3-3. All injection tests to compare different lubricants on their LSPI behavior have been carried out at an engine speed of 1850rpm and the rated power of 38kW, with a coolant temperature of 80°C and an intake air temperature of 40°C.

Table 3-3: Ionic liquids [17].

Ionic Liquid 1	Ionic Liquid 2
Molecular formula: $C_{34}H_{68}F_6NO_4PS_2$ Viscosity: 304 cP (25 °C) 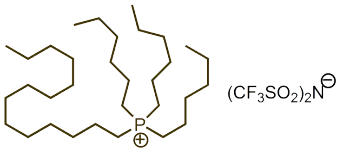	Molecular formula: $C_{48}H_{102}O_4P_2$ Viscosity: 1120 cP (25 °C) 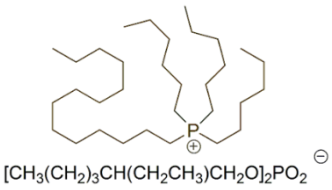

3.2.4 Oil consumption measurements

Blow-by system

One part of the investigations was to determine the oil consumption of the test engine. To split the overall oil consumption into their origin, we set up a special measurement method for the turbocharger oil consumption and the oil content transported by the crankcase ventilation system. Also, we needed to measure the test engine's overall oil consumption to execute a breakdown of the oil quantities.

At first, we measured the oil content in the crankcase ventilation gas, also called blow-by gas. Therefore, we used the measurement device explained in chapter 4.1.4. The procedure started with the weighing of the empty filters. After the filters were inserted into the measurement device and the filtration device was by-passed, the test began. After ten minutes of conditioning, the switch valve was actuated to pass the blow-by gas through the filtration unit. At the end of each operating point's measurements, the blow-by gas was again routed through the by-pass hose. Finally, the two filters were weighed, and the oil consumption per minute was calculated using the delta weight of both filters.

The blow-by oil measurement's operating points are shown in Figure 3-6. Below 9 bar BMEP, no blow-by mass flow was detected in the high-pressure blow-by recirculation system.

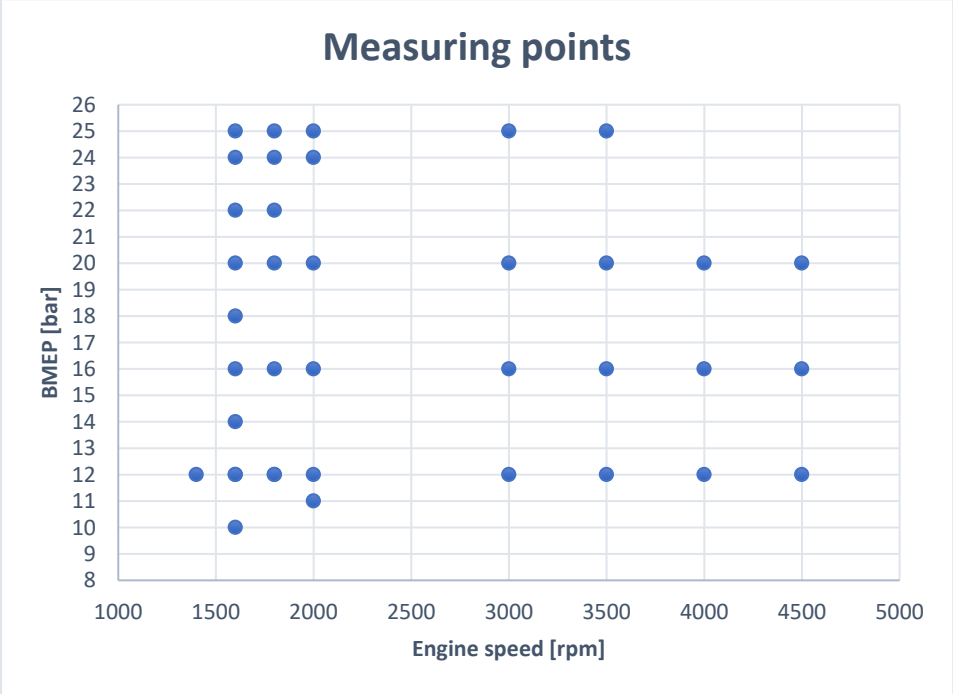

Figure 3-6: measured operating points for the blow-by oil content determination.

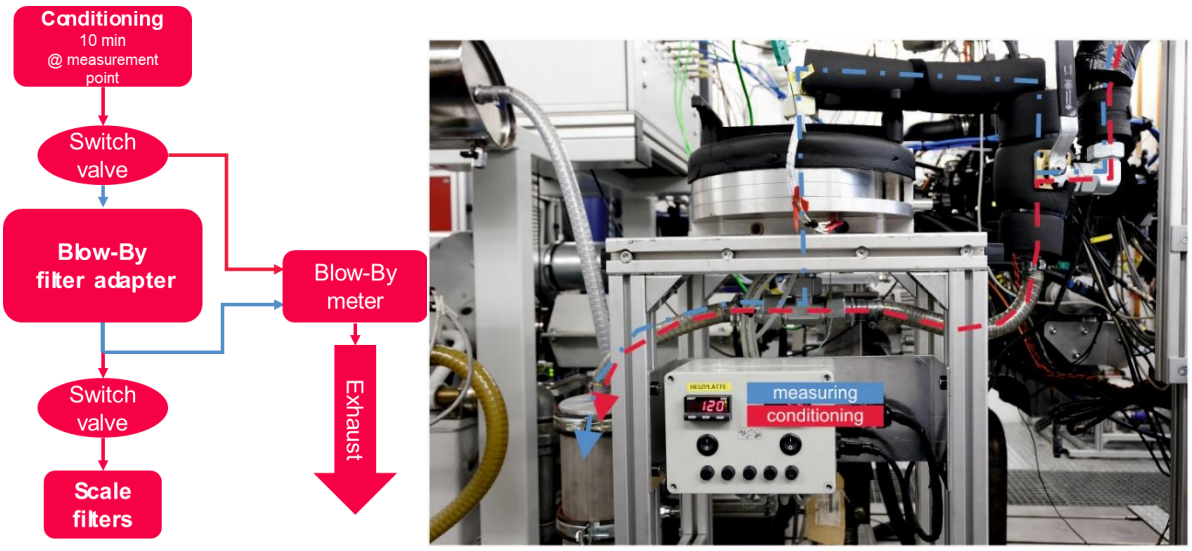

Figure 3-7: Blow-by measurement methodology.

Figure 3-7 shows the blow-by oil content detection methodology and the measurement device's picture with the sketched blow-by gas routes during conditioning and measuring.

Turbocharger

The oil consumption of the turbocharger unit has been detected with an external oil consumption measurement unit. It is possible to precisely adjust the turbocharger's oil supply with the external supply unit and adapt it to the operating point. Because the measurement system operated online, it was essential to keep the oil temperature stable to exclude changes in the oil density. Figure 3-8 shows the influence of temperature changes on the measured oil consumption. These investigations' measurement time varied between 1 hour and 3 hours to obtain good results depending on the operating point. The oil consumption was calculated using the measured delta oil mass, as shown below.

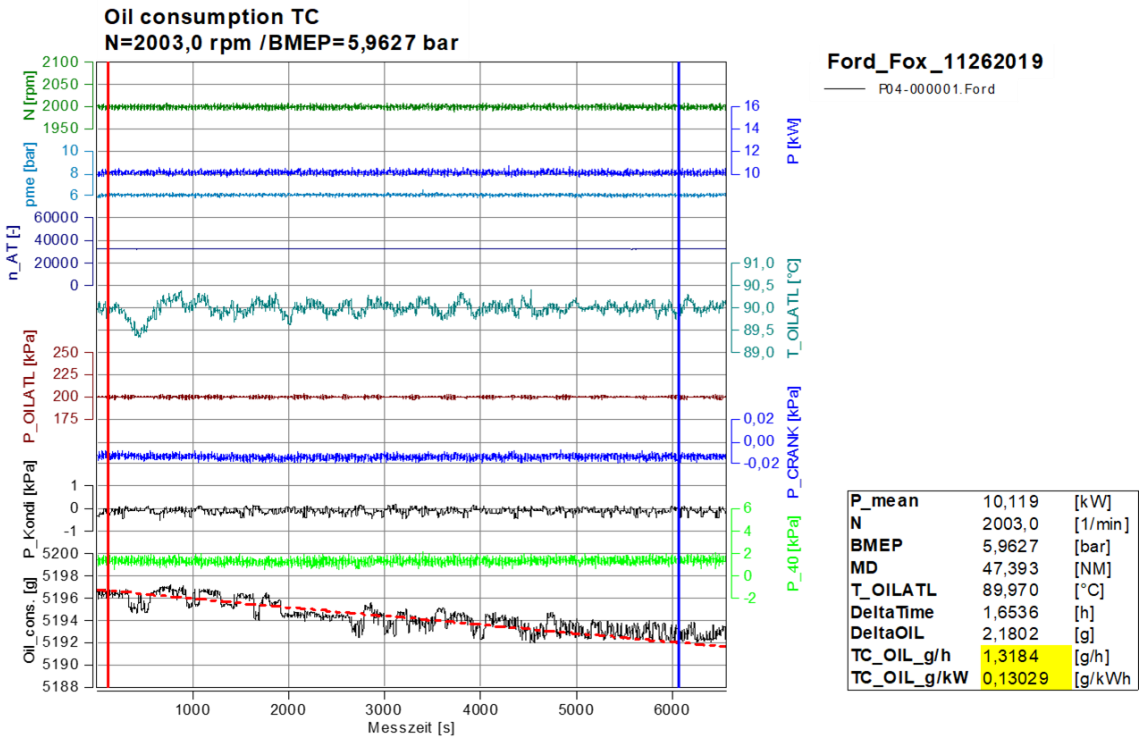

Figure 3-8:Turbocharger oil consumption measurement.

Overall oil consumption

The test engine's overall oil consumption measurements have been executed with a tracer method, explained in chapter 3.2.4. Therefore a map screening with the connected measurement device has been performed. The train and weight method results did not provide sufficient accuracy in reproducibility and were very time-consuming to gain results for a specific operating point. So we decided to use the tracer method instead.

With the different oil consumption results, a split of the test engine's different oil-consuming origins could be calculated. Therefore, the overall oil consumption was divided into the crankcase ventilation's oil consumption, the turbocharger, and the combustion chamber oil consumption. Figure 3-9 shows an example of the calculated oil split from the test engine's measured oil consumptions.

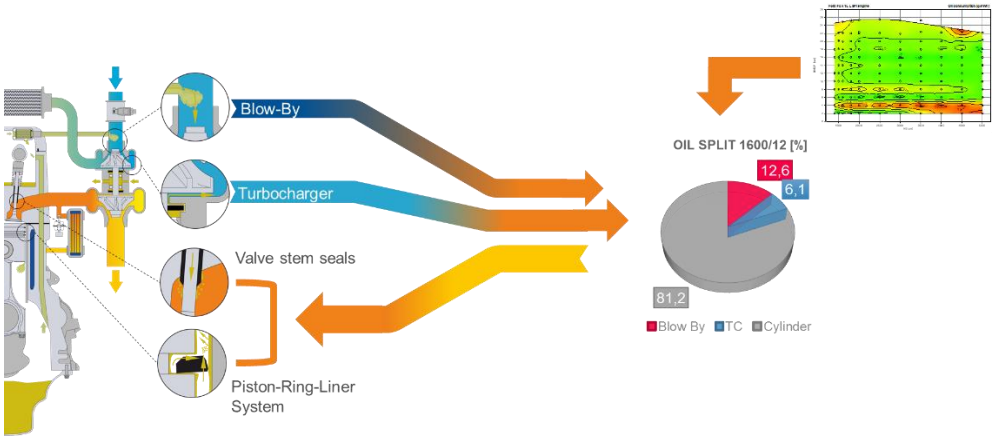

Figure 3-9: Example oil split methodology.

3.2.5 CNG Investigations

We were not able to reach the ISO operating point with the existing engine setup for the investigations with CNG as fuel. We increased the engine speed for the CNG investigations compared to the ISO operating point from 1600 rpm to 1850 rpm. Through this measure, we were able to reach the goal torque of 200 Nm. The idea behind the CNG investigations was to exclude the interaction between the injection spray and the liner. With a gaseous fuel, no interaction between the liner surface and the fuel spray occurs, so the dilution of the engine oil or the oil fuel mixture's building can be excluded. With this key-experiment, the influence of the spray liner interaction on the occurrence of LSPI can be shown. The CNG operating point has been investigated to compare the gaseous and the liquid fuel measurements for the gasoline setup. These measurements at 1850 rpm engine speed have been compared with the CNG measurements shown in chapter 5.1.4.

3.2.6 Hardware variations

For the variation of the engine hardware, the cylinder liner honing has been changed. The investigation process was similar to the parameter variation investigations. Therefore, the new engine block has been investigated at the ISO operating point to compare the different cylinder honing patterns to the standard honing. During these investigations, all thermodynamic parameters were the same as at the first investigations with the original engine block. To compare the different hardware, the number of pre-ignitions during the test sequence has been counted. With this methodology, we saw the influence of the liner surface quality on the number of LSPI events.

3.3 IFKM investigation methodology

In order to meet the shown objectives, a novel holistic investigation methodology for mechanism analysis was set up to accompany the entire LSPI development path by means of a multi-experimental approach.

Figure 3-10 shows the schematic of the methodology used at IFKM. The test engine is characterized iteratively under different engine parameters and operating materials with regard to its stochastic "macroscopic" PI tendency in order to uncover PI-critical engine operating conditions as a basis for further detailed "microscopic" analysis. These consist of a comprehensive optical in-cylinder PI characterization and subsequent key experiments to generate in-depth knowledge about relevant (sub-) processes. All this takes place on a minimally invasive optical engine system, which offers the possibility to detect fuel and oil in the combustion chamber with the help of upstream ex-situ light-induced fluorescence (LIF) investigations. In the final step, a multidimensional pre-ignition mechanism is derived by synthesizing all data obtained.

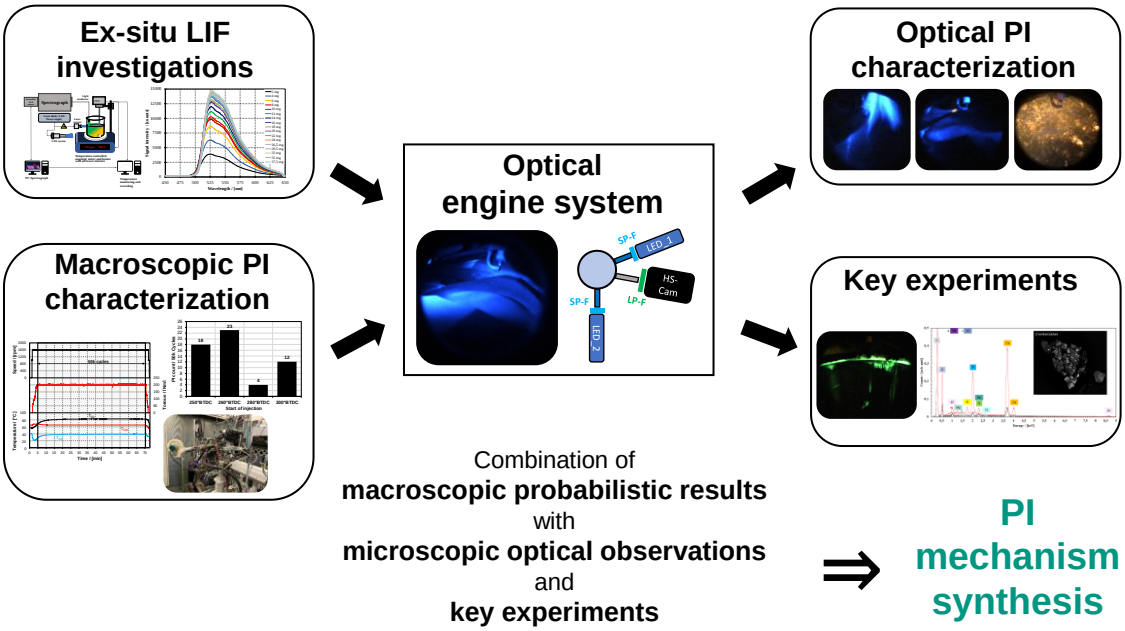

Figure 3-10: IFKM investigation methodology.

3.3.1 Ex-situ LIF investigations

The characterization of the fuel and oil behavior in the combustion chamber system under pre-ignition boundary conditions can lead to a deeper pre-ignition mechanism understanding. To implement this on the optical engine system and to find a suitable LIF setup for the detection of oil and fuel in the combustion chamber, the preparatory investigations follow the methodology presented in Figure 3-11. Using a developed test system, the interaction of light radiation with fluorescent dyes (tracer) in fuel and oil is investigated under different boundary conditions. By knowing the specific properties, a light/ tracer combination can be selected for the detection of fuel and oil. The optical feasibility of the engine system is validated by means of a cylinder head replica for endoscopic fluorescence detection, and thus a LIF setup is defined.

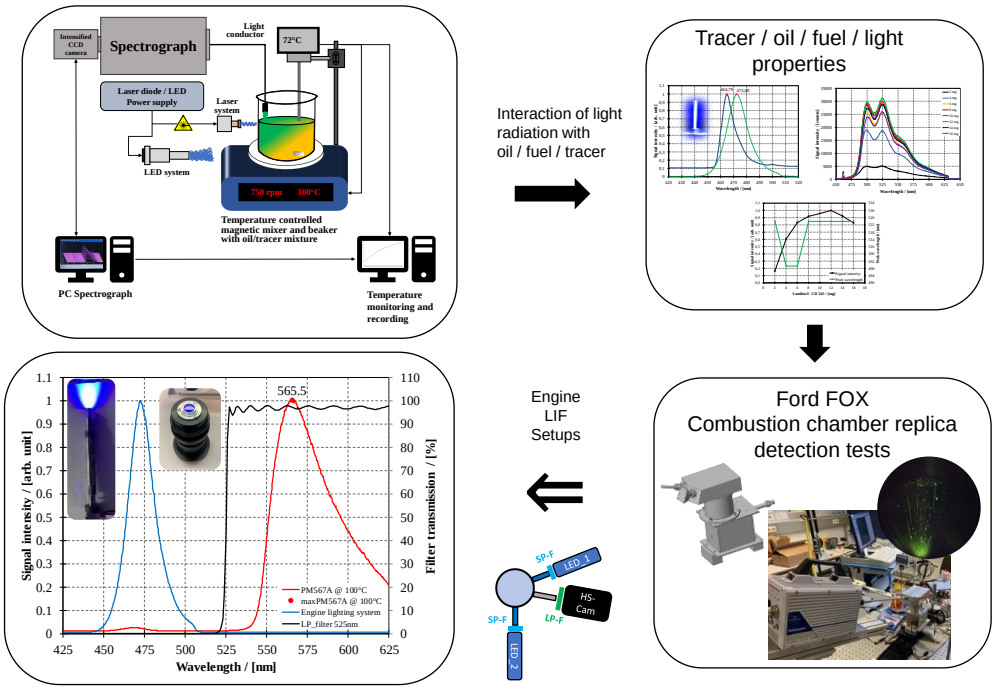

Figure 3-11: Ex-situ LIF investigation methodology.

3.3.2 Macroscopic PI characterization: Generation of pre-ignitions

For the implementation of the optical pre-ignition characterization, a reproducible pre-ignition level in the engine cycle range of 10k to 15k is necessary [18]. This results from the fouling tendency of the optical accesses under high load conditions and the associated need for cleaning. Figure 3-12 shows the test cycle used to find an engine operating media combination for a reproducible base pre-ignition level. For this purpose, the engine is operated stationary at a speed of 1600 rpm under a near-standard parameter-setup (see Figure 5-22) at an increased maximum torque of 200 Nm (MEP=25.2 bar) for 15k cycles each. In between, there is a one-minute operation at the maximum standard torque level of 170 Nm. The engine operation via using a prototyping engine control unit (ECU) enables full parameter control and access. All tests were performed without the use of knock control. The cooling water was preconditioned to 80° C and the engine was then brought to suction full load. The target torque is adjusted at a constant maximum valve overlap through the wastegate position. Here, an oil change between the individual runs did not take place here. The first basic requirements for the occurrence of pre-ignition can be derived. The pre-ignition detection took place via the event detection from a Kistler KiBox using cylinder pressure signals. Water-cooled Kistler pressure sensors of type 6041 were used at a near central combustion chamber position (see Figure 4-10). The scanning rate of the combustion analysis system is 0.1° CA. The detection criterion consists of exceeding a cylinder pressure threshold of 120 bar and a 5% mass fraction burned (MFB) earlier than 11° CA after top dead center (ATDC). This corresponds in each case to the average values at the load point plus four Sigma of the standard deviation. The event is then stored from the ring buffer for the respective cylinders with a defined (±) number of cycles (50). (Optical pre-ignition results show the general challenge/validity of macroscopic pre-ignition characterization by means of pressure detection.)

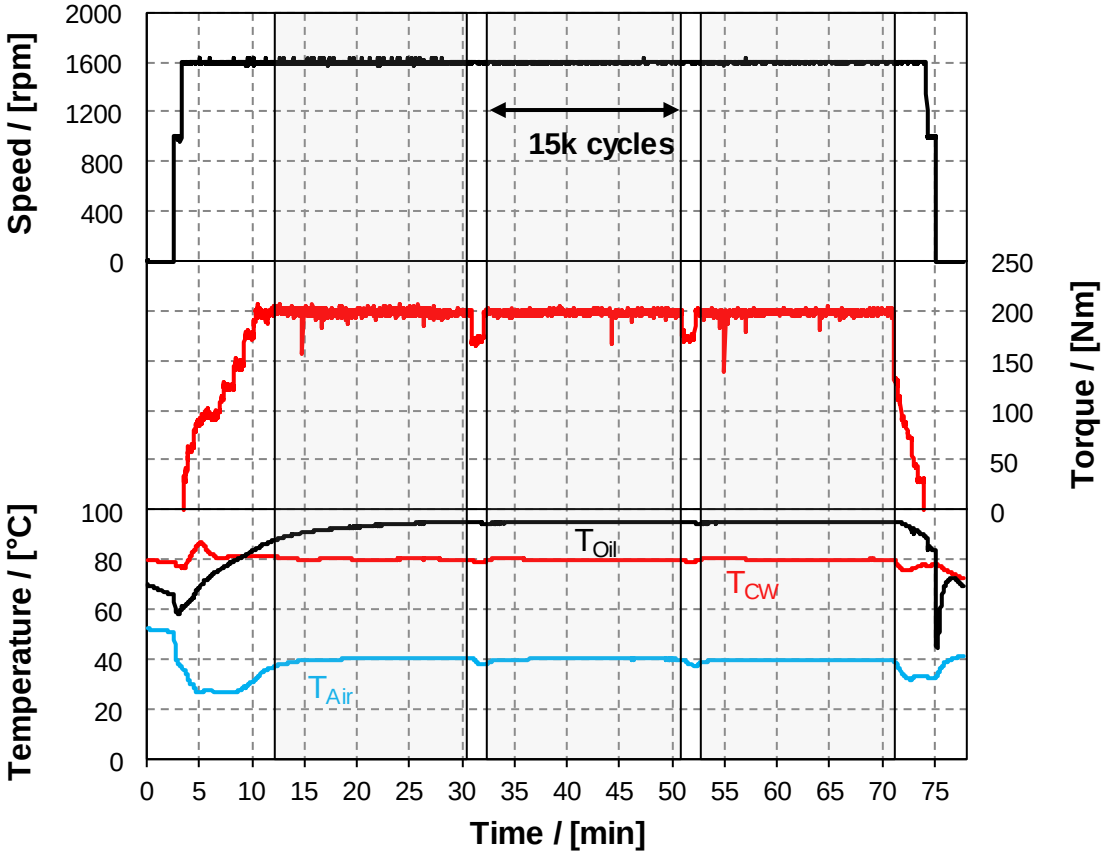

Figure 3-12: Pre-ignition generation test cycle.

3.3.3 Macroscopic PI characterization: PI critical engine operating conditions

The test cycle from Figure 3-13 was used to analyze and evaluate different engine parameter setups that lead to pre-ignition critical operating conditions. It consists of a steady-state load point at a speed of 1600 rpm and a torque of 200 Nm (MEP=25.2 bar) for a period of 50k cycles for each specific parameter setup. The driving style, as well as the pre-ignition detection via an event recognition, took place in the same way as in the previous section. However, in order to maintain comparable initial conditions, the motor oil was drained from the oil sump after each test cycle and replaced with approx. 4 liters of fresh oil. (Visual deposition impressions show the general challenge/validity of equal initial conditions) In addition, there were test series of constant engine parameter-setups, which each run through the test cycle three times without an oil change in order to demonstrate the influence of increasing oil dilution. A continuous iterative engine parameter adjustment was carried out for maximum pre-ignition generation in order to determine particularly critical states and to form an operating state basis for the subsequent optical investigations. From these pre-ignition characterizations, in particular in combination with the accompanying CFD simulation, first findings on critical "pre-ignition enabling processes" can be generated.

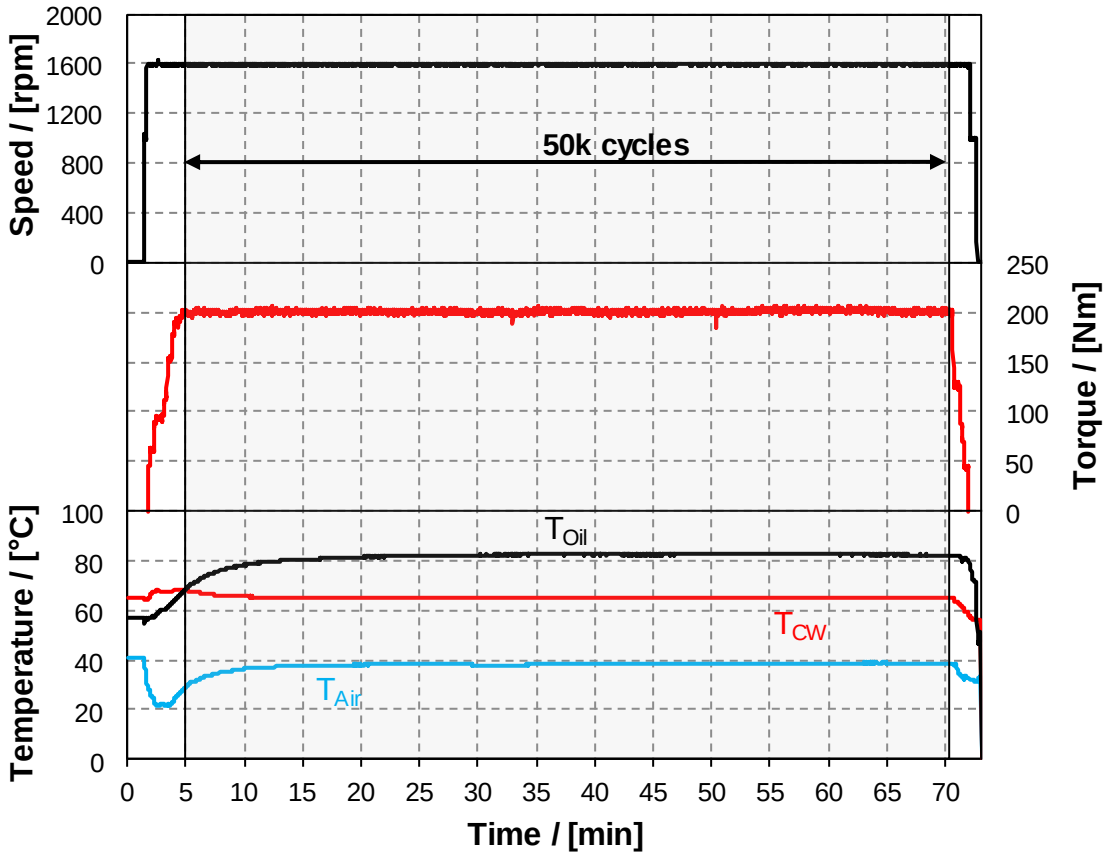

Figure 3-13: Pre-ignition characterization test cycle.

3.3.4 Optical pre-ignition characterization

The test cycle for optical pre-ignition characterization in Figure 3-14 corresponds to the previous test cycle. The preconditioned test engine is brought to the relevant load point with its specific engine parameter setup as quickly as possible and monitored by means of pre-ignition detection. In the case of an event detection, the combustion analysis system outputs a trigger signal to the HS camera controller in addition to storing the pressure data from the ring buffer. The camera system also records data in a ring buffer system and then stores the image data of (±) 8.3 cycles at 1600 rpm on the camera computer. For each image recording, the camera controller, in turn, sends a TTL signal to the combustion analysis system in order to guarantee a crank angle assignment. The camera is not available for further recordings while the camera data is being transferred. It has been shown that a maximum of two pre-ignition events can sensibly be recorded before the fouling of the access window no longer makes meaningful image data interpretation possible insofar as these occur within a maximum of 10k cycles. The engine parameter setup with the maximum pre-ignition frequency allows a useful optical measurement window of around 7k cycles. This procedure was used for all applied optical engine setups as well as all specific engine parameter setups. The optical characterization provides further databases for the accompanying simulations, which are iteratively adapted. On the basis of the optical recordings in combination with the macroscopic examination results and the simulation results, a deeper understanding of the pre-ignition mechanisms can be built up.

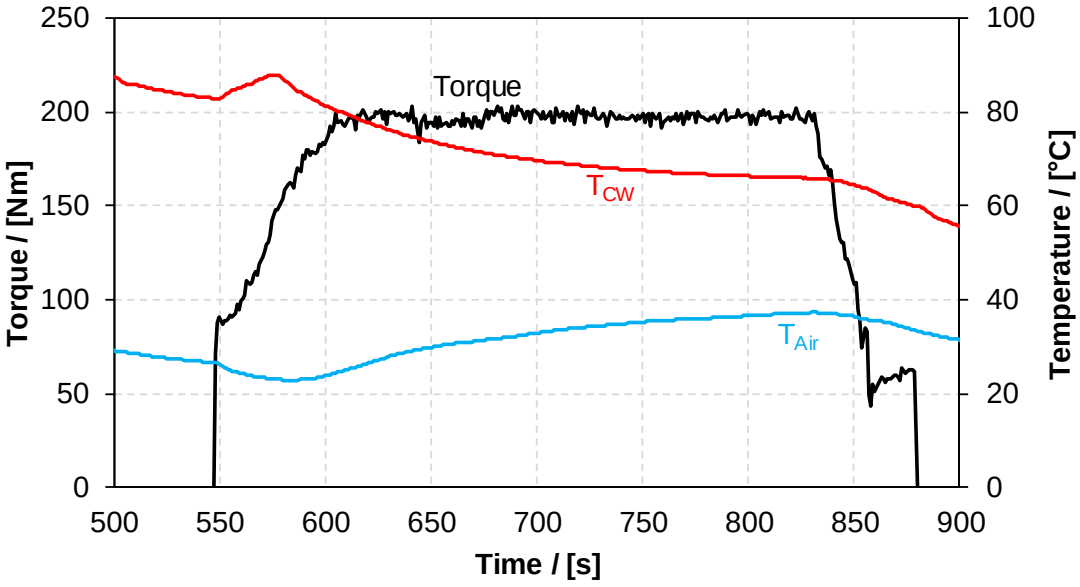

Figure 3-14: Exemplary optical pre-ignition run test cycle.

3.3.5 Key experiments

With the help of three key experiments, individual phenomena are to be specifically investigated in order to expand the data basis for the pre-ignition mechanism synthesis.

3.3.5.1 LIF detection of engine fluids

With the knowledge from the ex-situ LIF investigations, both fuel and engine oil are mixed with an efficient amount of fluorescent dye (tracer). With a LIF setup adapted to the optical test engine (Figure 3-15), information about the fuel and oil behavior in the combustion chamber can be obtained. For this purpose, the high-power LED combustion chamber illumination system is spectrally truncated by means of short-pass filters in order to be able to detect an unambiguous fluorescence response of oil or fuel via the long-pass filtered observation. Global combustion chamber fluorescence detection on an engine system under pre-ignition conditions via endoscopic observation represents an extreme challenge. The fluorescence spectra for fuel and oil are in an overlapping range, which is why engine operation with traced fuel and traced oil was examined separately. The LIF setup was also used to obtain information about the combustion chamber movement of the introduced oil during oil injection key experiments.

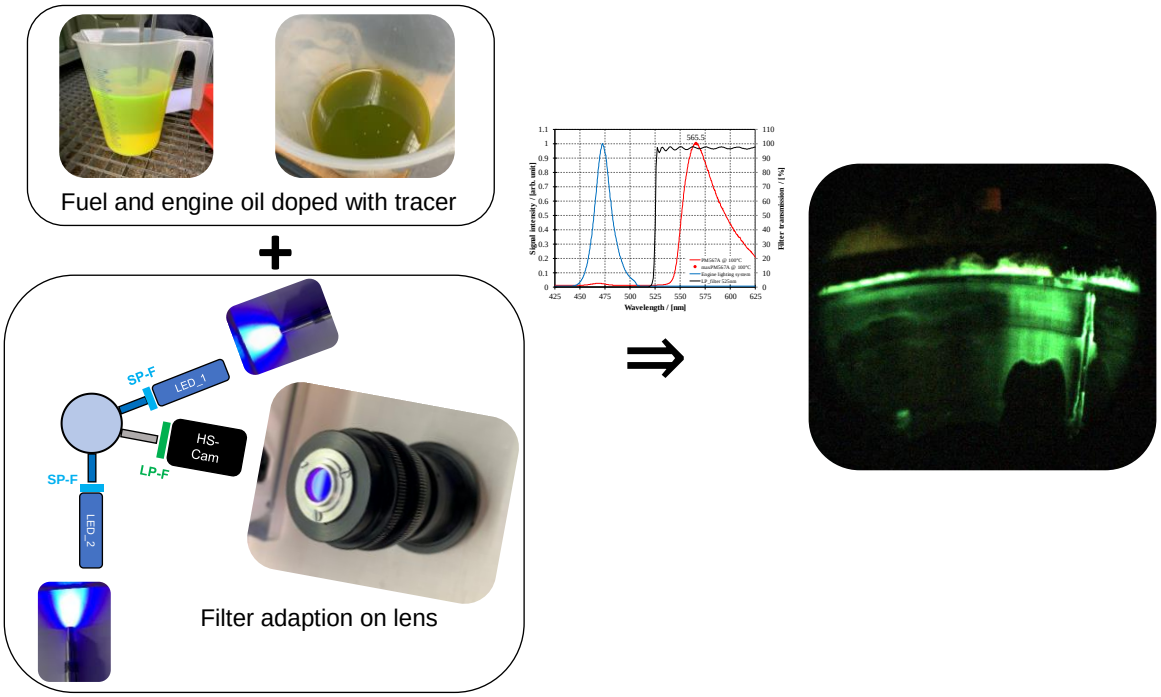

Figure 3-15: Engine LIF setup.

3.3.5.2 Oil injection investigations

Another key experiment is the targeted injection of oil quantities into the optical cylinder via the inlet valve 2. The system shown in Figure 3-16 enables the introduction of an oil mass flow, which can be adapted by an adjustable throttle via a peristaltic pump with constant speed and a cannula fixed in the air box. In upstream ex-situ investigations, the system showed negligible oil mass flow sensitivity to feed chamber pressure and oil temperature. With this, additional deposits of different oils can be generated and their global pre-ignition influence can be assessed. The possibility of droplet-induced pre-ignition can also be investigated. Due to the targeted type of oil injection, additional "reference deposits" can be generated at specific combustion chamber locations and their pre-ignition influence can be investigated, as well as a correlation analysis to naturally generated deposits can be performed. In addition, a possible air-fuel ratio pre-ignition influence process can be identified.

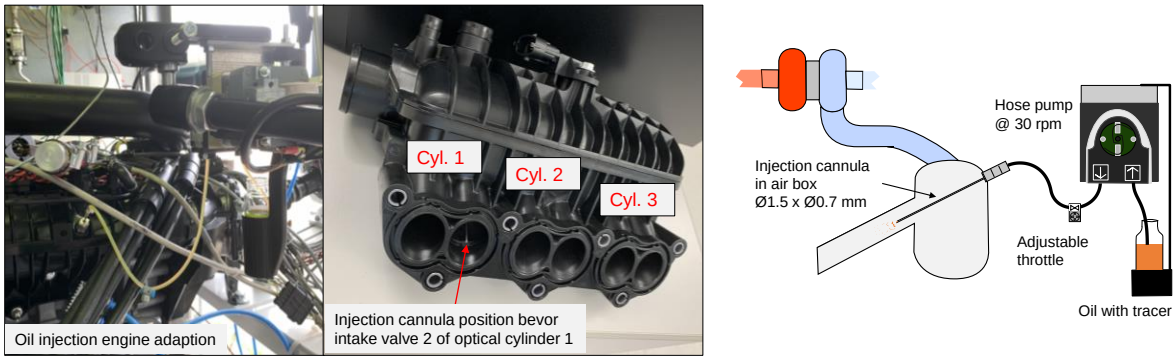

Figure 3-16: Oil injection engine setup.

3.3.5.3 Combustion chamber deposit characterization

The third key experiment includes an extensive characterization of deposits, which allows conclusions to be drawn about the formation and effect mechanisms of deposits in the context of a multidimensional pre-ignition mechanism. For this purpose, the investigation path from Figure 3-17 is applied. In a first step, deposits at specific pre-ignition-relevant combustion

chamber positions after pre-ignition runs as well as the oil reference deposit described in the previous subsection, are extracted. The positions could be localized in the course of the optical pre-ignition characterizations as well as the CFD simulations. The extracted deposits are then analyzed in two steps using a scanning electron microscope (SEM). Backscattered electron contrast (BSE) images provide qualitative statements about the element frequency of heavy elements in the samples. Since the deposits are mainly composed of carbon, BSE images provide good information about the accumulation and distribution of oil-specific components such as oil ash residues. A connected Energy Dispersive X-ray Spectroscopy (EDX) analysis provides information about which elements can be found at specific places of these deposits. A final thermal gravimetric analysis (TGA) provides information about the different oxidation reactivities and thus the potential to ignite air-fuel mixtures under certain boundary conditions. Thus, local pre-ignition phenomena, specific deposit-oxidation reactivities as well as compositional elements can be correlated and their central importance for the overall mechanism can be shown. TGA can thus be used to evaluate deposits with respect to their potential to influence pre-ignition.

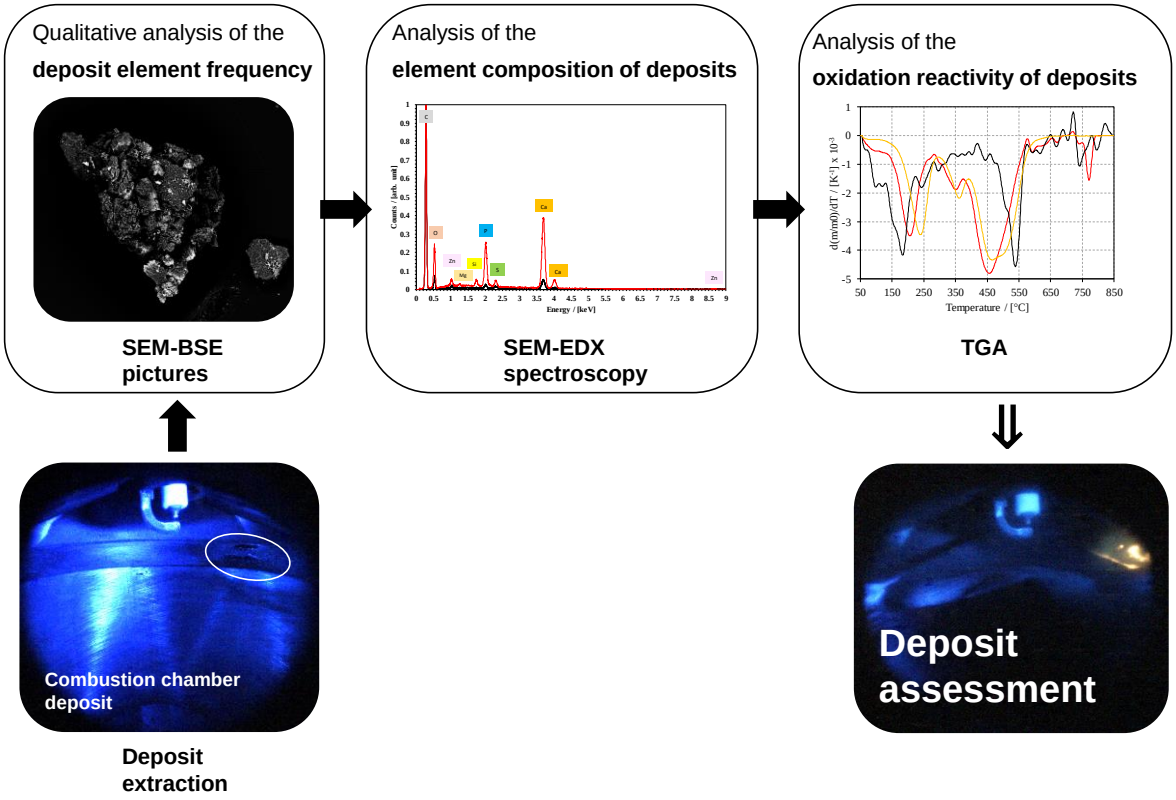

Figure 3-17: Investigation path for deposit characterization.

3.4 Numerical investigations

In addition to the measurements, numerical investigations are performed. The goal of the simulations is to confirm observations made on the optical and thermodynamic testbeds. Furthermore, the simulation is used to extend the knowledge gained from the experiments by the accessibility of data that cannot be measured.

This project focuses on the hypothesis of the two-phase induced pre-ignition, i.e., the mixture ignition by droplets or particles. A 3D CFD engine model including a stochastic parcel release was established to capture this statistical event with a numerical approach. The properties of the parcels were assumed to either represent a liquid droplet or a solid particle. The CFD simulation provides detailed information on the gas temperature and composition close to the particles by tracking these parcels' trajectories in the combustion chamber. These boundary conditions can be used to study the ignition mechanism on a particle scale, reducing the numerical effort. This allows for a more detailed mathematical description of the ignition problem.

Furthermore, the distribution of different modeling tasks is possible. In this case, the CFD-simulation was carried out by IFA, the mechanism-development by ITT.

3.4.1 1D Process simulation

Ford supplied a full engine model of a series application, including the complete air and exhaust paths in the simulation environment GT-suite v2018. Since the air and exhaust pathways at the testbeds and the engine itself were modified compared to the series application, the 1D-model had to be adjusted. Due to the fact that the pressure sensors in this project were located at the same position at both testbeds (IFKM, IVT), the model was reduced to a TPA-configuration. Figure 3-18 shows the out-line of the 1D-model.

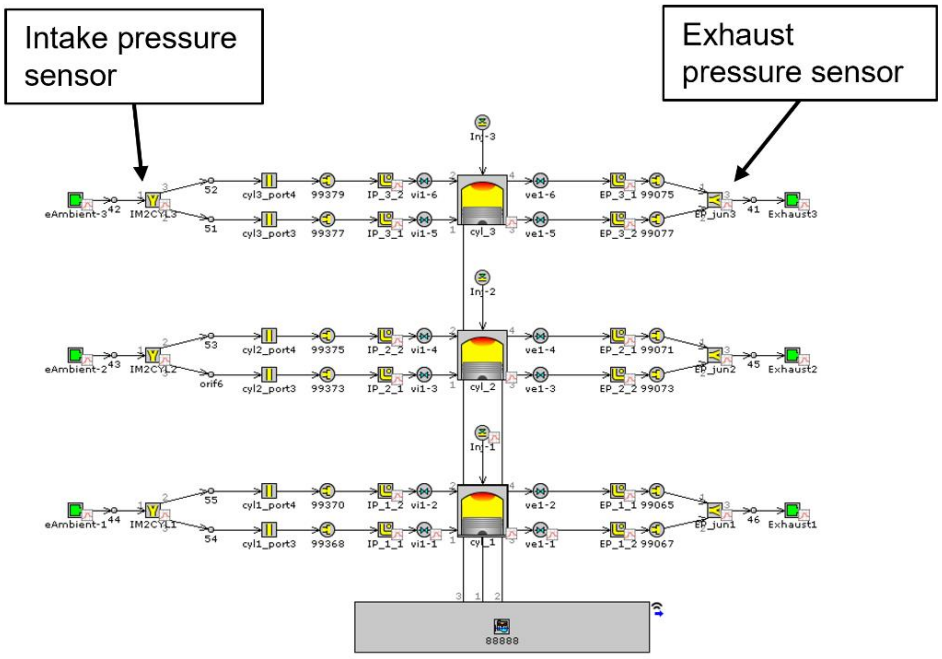

Figure 3-18: 1D-model of the testbed configuration.

Measurement data obtained from high- and low-pressure indication sensors was used as boundary conditions. Thus, a gas exchange and cylinder charge at inlet valve closing, identical to the testbed, was ensured. The heat release was modeled using an adjusted Wiebe function to meet the measured high-pressure curve. Furthermore, the wall temperatures of the engine parts were predicted using a CHT-model.

3.4.2 Engine grid generation

The numerical grid was generated using the Siemens-Software StarCD/es-ice version 4.30.029. The simulation domain included the combustion chamber, the piston crevice volume, and the intake- and exhaust-ports up to the position of the pressure sensors. The crevice volume was added to the model due to the assumed importance of fuel and oil accumulations, which was the project's premise. The grid is able to perform piston and valve motion to calculate the gas exchange and the in-cylinder flow field properly. The piston crevice volume was designed as a structured ring-shaped grid to ensure stable numerical conditions. This static mesh segment was generated in AVL FIRE version v2017d and exported to the StarCD/es-ice engine model, where it was coupled to the moving piston and liner via an interpolation interface.

Figure 3-19 shows the numerical grid at the top dead center (TDC) position.

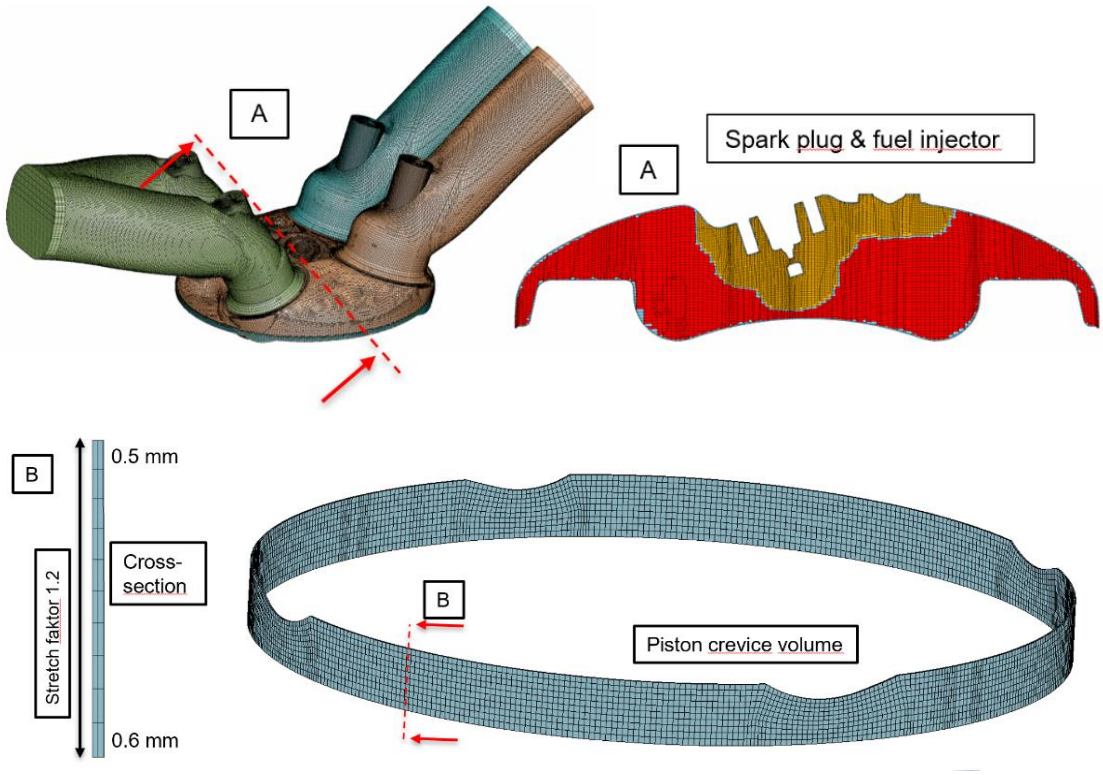

Figure 3-19: CFD-grid of the investigated engine at TDC.

The aim of the mesh was to calculate droplet trajectories and evaporation accurately. Therefore, the influence of the cell base-size on the evaporation was investigated beforehand. As a reference, literature data of evaporation measurements of a single 500 µm n-heptane droplet were taken. [19] [20] The droplet was supported by a thin wire (< 150 µm) and evaporated under defined boundary conditions. This setup was re-produced numerically with cell base-sizes of 0.5 mm up to 2 mm, although it has to be mentioned that the thin support wire was neglected. Therefore, it could be expected that the calculated evaporation rate will be similar to the measurement results from Chauveau [19] due to the very thin support fiber (14 µm). Figure 3-20 shows the sensitivity analysis results.

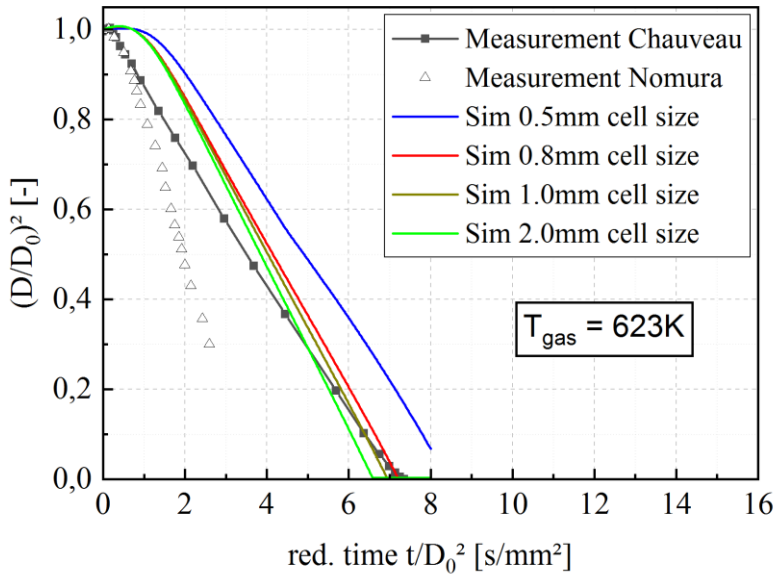

Figure 3-20: Grid sensitivity analysis on evaporation.

It could be observed that the calculated evaporation rate is underestimated at the beginning of the simulation. This delay results from the assumption that the modeled droplet temperature is assumed to be uniform. As a result, the droplet surface temperature, which determines the evaporation rate, experiences a slower heat-up. After a short period of time, the droplet reaches its constant wet-bulb temperature, where the evaporation rate is dominated by the surface area (D^2-Law). The simulations showed that the evaporation rate is modeled adequately with high grid resolution. However, a cell base size of 0.5 mm shows some minor numerical artifacts, indicating numerical instability. This effect is due to the high volume fraction of the modeled droplet inside the numerical cell ($VF = V_{Drop}/V_{Cell}$). The numeric appeared to be stable as long as the liquid volume threshold of 0.4 is not surpassed.

Based on Tanaka's optical observations [21] [22], the expected droplets released out of the piston crevice area are in the range of 250 µm. A 0.5 mm cell base-size is chosen to meet the trade-off between numerical accuracy and computational effort. This leads to an overall cell count of ~5x106 at the bottom dead center (BDC).

3.4.3 Modeling of the liquid phase

The liquid phase in engine simulations is expected to occur as small droplets or thin liquid films. Therefore, the use of simplified modeling approaches is acceptable. [23]

In both cases, the liquid phase is modeled without actual volume representation in the numerical grid. The particles and films interact with their environment only by model-based equations (energy-, mass-, momentum balance). The thermodynamic properties of the liquid phase are represented by mean values (0D-approach). This assumption is valid if the expected biot-numbers are small. In the case of droplets, diameters smaller than 500 µm are going to lead to only minor inaccuracies. [24] The same applies to thin liquid films.

3.4.3.1 Fuel liquid phase composition

The evaporation characteristic of the fuel determines the fuel vapor and temperature distribution inside the combustion chamber. To be able to model gas phase ignitions later on accurately, a detailed fuel model is necessary.

The evaporation characteristic of a given liquid can be deduced from the standardized distillation process according to ASTM D86 [25] and DIN EN ISO 3405 [26]. For the used fuel in this project, such measurement data was supplied by Coryton in addition to a fundamental chemical analysis, see Figure 3-21 and Table 3-4.

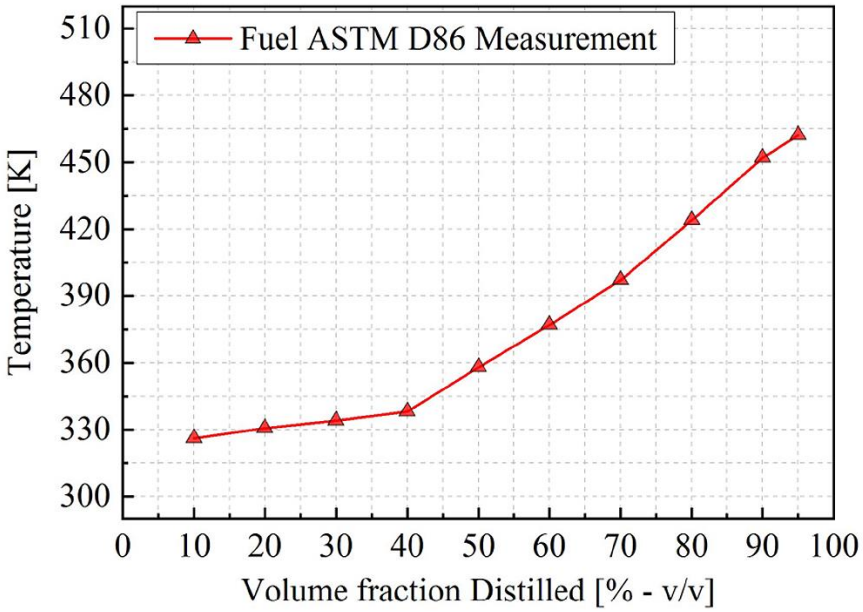

Figure 3-21: Distillation curve – Fuel.

Table 3-4: Fundamental chemical composition – Fuel.

Chemical Subgroup	Unit	Result
Paraffins	[%-v/v]	15.3
Iso-paraffins	[%-v/v]	29.7
Olefins	[%-v/v]	9.7
Naphthenes	[%-v/v]	6.9
Aromatics	[%-v/v]	28.8
Ethanol	[%-v/v]	8.3
Unknowns	[%-v/v]	1.4

Fuels consist of numerous hydrocarbons, which leads to a smooth increase of the boiling temperature during the evaporation process. In order to capture this effect in the CFD analysis, a multi-component surrogate approach was chosen. The composition of this surrogate had to be determined to represent the evaporation characteristic and meet the fundamental chemical composition of the actual fuel. Therefore, a 0D distillation model had to be established. The model described the distillation process mathematically by dividing it into three sub-stages, shown in Figure 3-22.

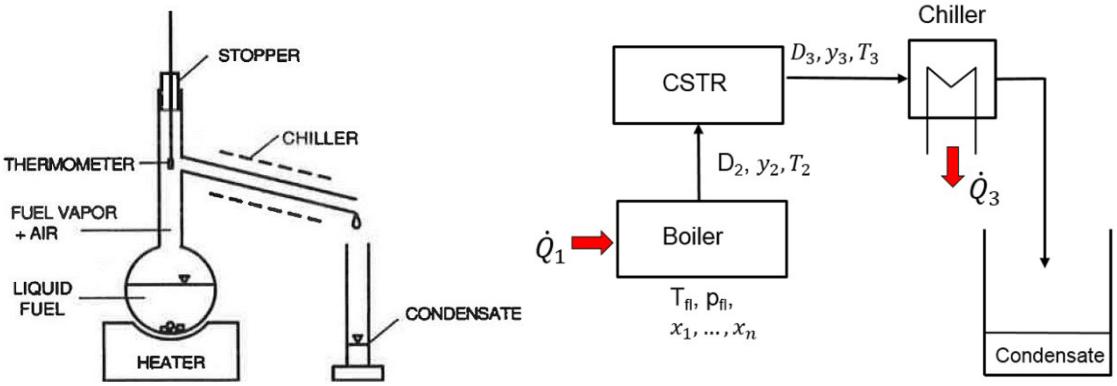

Figure 3-22: 0D distillation model [6].

In the Boiler-stage, the liquid fluid is heated up, and the vapor-liquid-equilibrium is calculated. In order to account for mixture effects in the liquid phase, activity coefficients were calculated for every species using the UNIFAC method. This correction of the vapor pressure is necessary if the fluid mixture components differ significantly in chemical structure. In this case, the hydrophilic hydroxy-group of ethanol was expected to interact with the non-polar hydrocarbon species. [23, 27, 28] The evaporated mass is then transported to the Constant Steering Reactor-stage. This stage accounts for the inherent inertia of the system. Furthermore, the gas temperature is measured at this location. The incoming gas is mixed with the residual gas and displaces it partially. Additionally, the heat transfer between the hot gas phase and the glass walls is calculated. The displaced gas mass is pushed into the Chiller, where the species are condensed and collected.

After applying this approach, 11 components could be found which meet the measurement data, displayed in Figure 3-23 and Table 3-5.

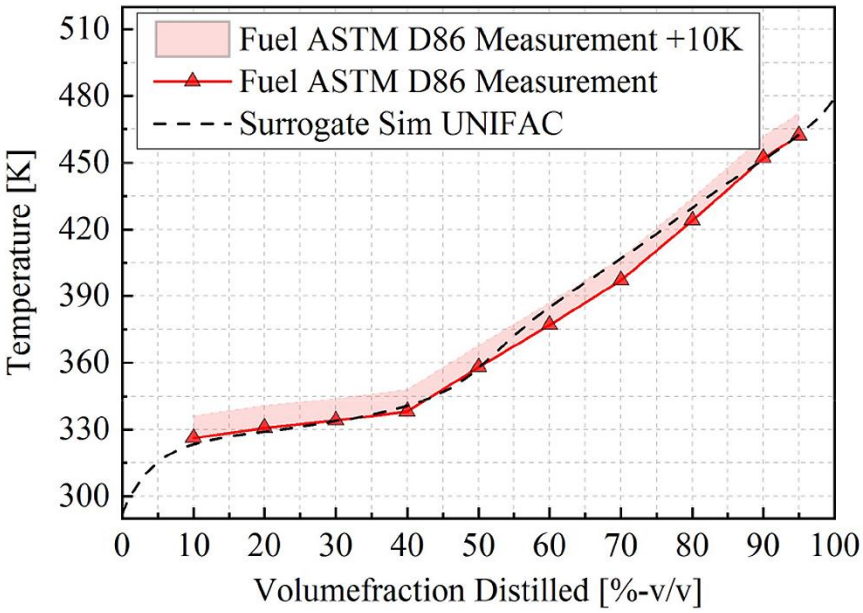

Figure 3-23: Modelled vs. measured distillation curve.

Table 3-5: Composition of the fuel surrogate.

Chemical Subgroup	Unit	Measurement	Surrogate
Paraffins	[%-v/v]	15.3	16.0
Iso-paraffins	[%-v/v]	29.7	30.3
Olefins	[%-v/v]	9.7	9.9
Naphthenes	[%-v/v]	6.9	7.0
Aromatics	[%-v/v]	28.8	28.3
Ethanol	[%-v/v]	8.3	8.5
Unknowns	[%-v/v]	1.4	0.0
Surrogate species	**Chemical Formula**	**BP @ 1bar [K]**	**Mass fraction [-]**
Iso-Pentane	C5H12	301.15	0.10
n-Pentane	C5H12	308.85	0.11
Cyclopentane	C5H10	321.95	0.07
1-Hexene	C6H12	336.25	0.09
Ethanol	C2H5OH	351.47	0.09
Iso-Octane	C8H18	372.15	0.17
Toluene	C7H8	384.15	0.02
Ethylbenzene	C8H10	408.85	0.13
1,2,3-Trimethylbenzene	C9H12	449.15	0.14
Naphthalene	C10H8	490.55	0.05
n-Tridecane	C13H28	508.15	0.03

3.4.3.2 Oil liquid phase composition

In the case of lubricant oil, the distillation method is not suitable because the fluid mixture's boiling temperature can be above the thermal decomposition temperature. Therefore, a gas chromatographic analysis was used to characterize the oil composition. Such measurement data was supplied by Fuchs Schmieröl GmbH.
For modeling purposes, a multi-component surrogate approach was chosen to be consistent with the fuel modeling strategy. The species' selection was limited to n-alkanes because fluid properties of long-chained isomers and other chemical configurations were not available. The used fluid databases were the VDI-Wärmeatlas [29], the NIST-thermophysical database [30], and the database of the CRC-Handbook of Chemistry [31]. These databases provide fluid properties up to a carbon chain length of 29. Data above this molecule size was extrapolated, which is described in [24] in detail.

Figure 3-24 and Table 3-6 show the GC-measurement result and the oil surrogate species selection. Considering the Noack volatility test [32], species with a normal boiling point above 773 K should not have any evaporation losses under actual engine conditions. Therefore, only the species with a lower normal boiling point were discretized. The species above this threshold were modeled using a single species (Tetracontane - C40H82) in order to account for the oil surrogate mixture's heat capacity.

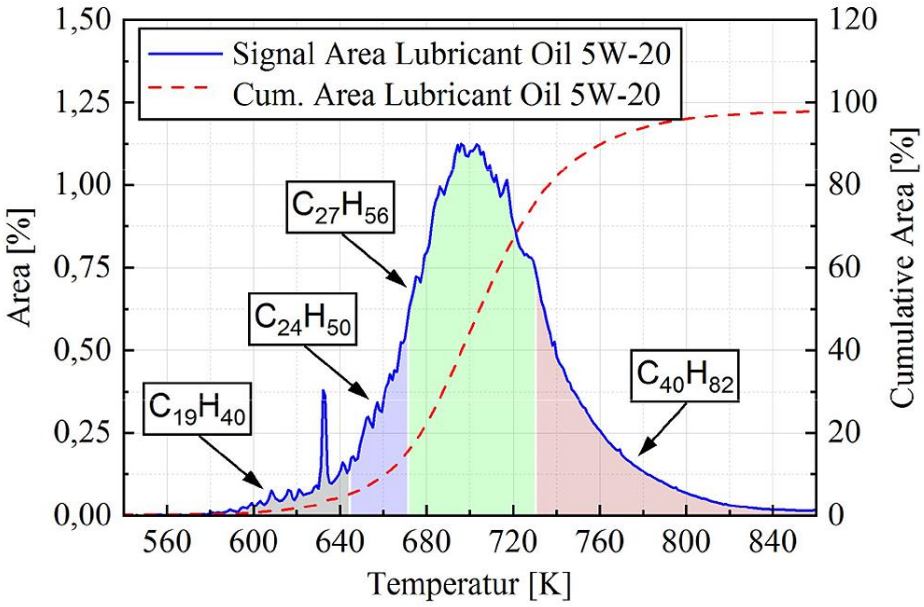

Figure 3-24: GC-measurement and surrogate species selection of the lubricant oil.

Table 3-6: Oil surrogate composition.

Surrogate species	Chemical Formula	BP @ 1 bar [K]	Mass fraction [-]
Nonadecane	C19H40	603 K	0.05
Tetracosane	C24H50	664 K	0.10
Heptacosane	C27H56	694 K	0.60
Tetracontane	C40H82	796 K	0.25

3.4.4 Modeling of the fuel injection

To properly fit the numeric models, spray measurements were supplied by BOSCH.Table 3-7 summarizes the available measurement data. The spray spectrum was characterized by a PDA analysis at a distance of 50 mm from the spray tip. The penetration length of the spray

was measured using high-speed imaging. The orientation of every spray coil was measured using the footprint method. All measurement data refer to a rail pressure of 100 bar.

Table 3-7: Spray measurement data.

Rail pressure	100 bar
Ambient pressure	1 bar
Injector mass flow	25.70 kg/h
Penetration length	High-speed imaging
PDA (SMD/DV90) - 50 mm distance	13.2 µm / 23.2 µm
Spray coil orientation	Footprint measurement
Spray cone angle (outer/inner)	11° / 0°

The numerical simulations were performed using a box-shaped grid with a cell base size of 0.5 mm. In order to capture the high velocity-gradients between the gas and the injected liquid phase, the cell size was locally (5 mm radius) refined to 0.25 mm.

The droplets were treated as Lagrangian particles according to the well-known DDM-approach. The secondary break-up due to aerodynamic forces was considered by using the Reitz-Diwakar model [33]. The primary break-up was not modeled explicitly. Instead, the initial droplet spectrum was described by using a Rosin-Rammler distribution, shown in equation 1.

$$CDF = 1 - e^{\left[-\left(\frac{D_d}{X}\right)^q\right]} \quad (1)$$

X and q represent empirical parameters to calibrate the distribution function. The initial velocity was calculated using equation 2.

$$\dot{m}_{spray} = \rho_l * v_{init} * A_{eff} \quad (2)$$

A_{eff} represents the effective nozzle hole cross-section area. The mass flow rate ($\dot{m}_{spray}$) of the injection was assumed constant. The three parameters X, q, and A_{eff} had to be calibrated to fit the spray model to the measurement data. Figure 3-25 and Table 3-8 show the results achieved for a parameter set of $X=2.7*10^{-5}$, q=1.7, and an effective nozzle hole diameter of 125 µm.

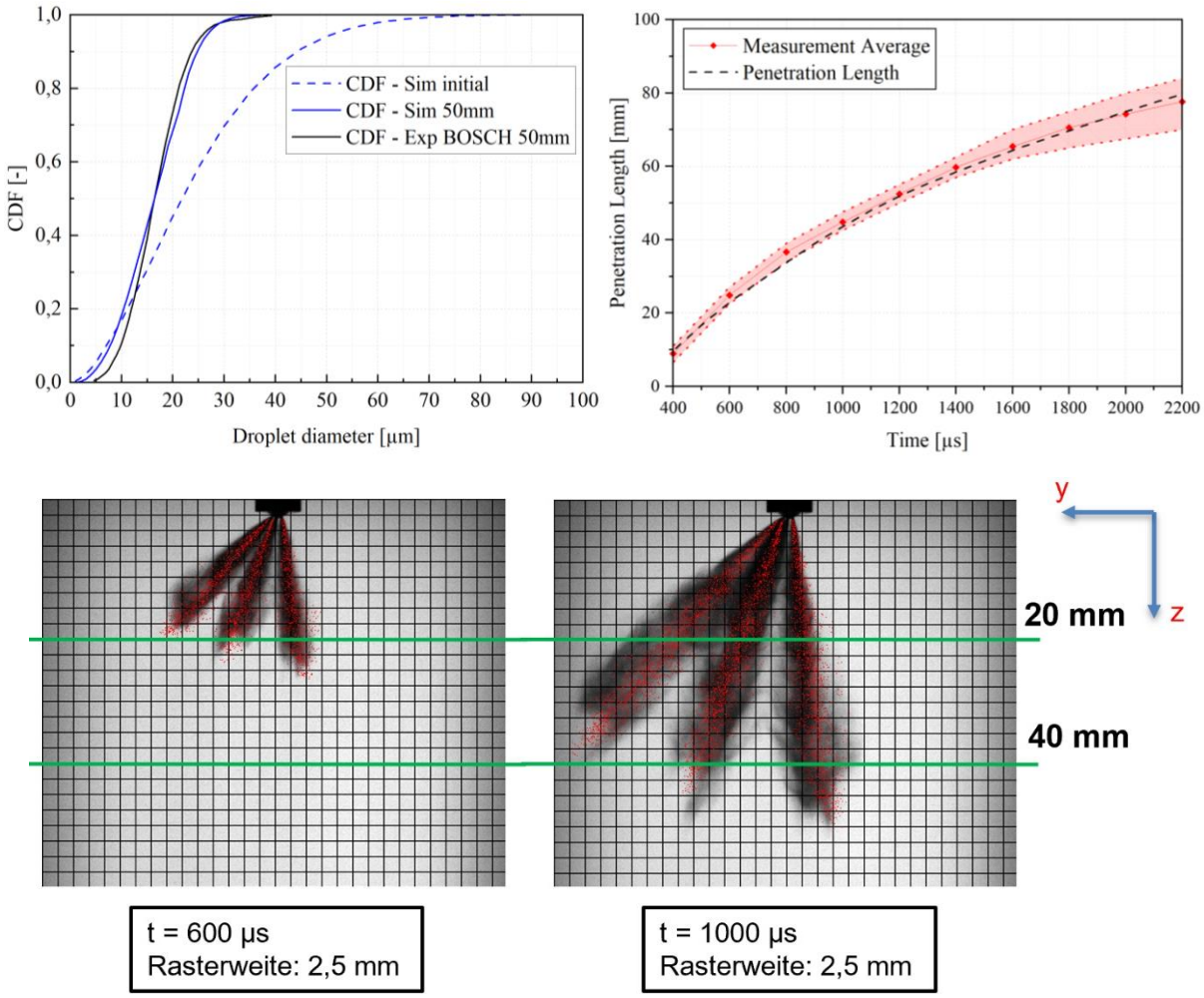

Figure 3-25: Simulated vs. measured spray results.

Table 3-8: Spray spectrum characterization.

50 mm distance	Measurement	Simulation
DV10	9.8 µm	7.8 µm
DV50	16.4 µm	16.5 µm
DV90	23.2 µm	24.8 µm
SMD	13.2 µm	13.1 µm

3.4.5 Detailed simulation of ignition at droplets

3.4.5.1 General equations

To formulate the governing set of compressible Navier-Stokes equations for a reactive system and equations of state for the gas phase and the liquid phase.

In these equations, the model for a homogeneous reactor (which was also considered in part of the studies) is included as a special, simplified case. Generally, this model results from setting all spatial derivatives (divergence and gradient operators) equal to zero. Additionally, for constant pressure systems, the volume (at fixed total mass) is allowed to change.

$$\frac{\partial \rho}{\partial t} + \mathrm{div}(\rho \vec{v}) = 0$$

$$\frac{\partial \rho_i}{\partial t} + \mathrm{div}(\rho_i \vec{v}) + \mathrm{div}\vec{j_i} = M_i \dot{\omega}_i$$

$$\frac{\partial (\rho \vec{v})}{\partial t} + \mathrm{div}(\rho \vec{v} \otimes \vec{v}) + \mathrm{div}\bar{\bar{p}} = 0$$

$$\frac{\partial \rho u}{\partial t} + \mathrm{div}\left(\rho u \vec{v} + \vec{j_q}\right) + \bar{\bar{p}} : \mathrm{grad}\vec{v} = 0$$

$$\text{gas: } p = \frac{\rho}{\bar{M}} RT \qquad \text{liquid: } \rho = \rho(T)$$

t denotes the time, ρ the density, $\vec{v}$ the velocity, ρ_i the density of species i, $\vec{j_i}$ the diffusion flux density of species i, M_i the molar mass of species i, $\dot{\omega}_i$ the molar scale rate of formation of species i, $\bar{\bar{p}}$ the pressure tensor, u the specific inner energy, $\vec{j_q}$ the conductive heat flux density, $\bar{M}$ the mean molar mass and R the universal gas constant.

The chemical source term $\dot{\omega}_i$ for species i can be computed if all the reactions in which species i is involved (either by chemical formation or consumption) are known. These reaction equations specify the stoichiometric coefficients of each species on the educt (initial substance) and product side, as well as the velocity coefficient k_r of the chemical reaction. The latter is a strongly temperature-dependent quantity, modeled by an Arrhenius expression of the form

$$k_r = A\, T^b \exp\left(-\frac{E_a}{R\, T}\right).$$

In the pre-exponential term AT^b, b is a temperature-exponent and E_a is the activation energy; R in this formula is the gas constant. The values of b and E_a are specific for each reaction.

Quantitatively, in a system of a number of R reactions, the chemical source term of species i can be expressed using the velocity coefficient k_r, stoichiometric coefficients ν^e_{ri} and ν^p_{ri} on the left and right side of the reaction equation of reaction r, by

$$\dot{\omega}_i = \sum_{r=1}^{R} k_r (\nu^p{}_{ri} - \nu^e{}_{ri}) \prod\nolimits_{s=1}^{S} c_s^{\nu^e_{rs}}$$

with c_s (s = 1,..,S, S: total number of species) the concentrations (number densities, expressed e.g. in mol/m^3) of the species.

The chemical reactions occurring in a given fuel/air mixture are, in this model, simple represented by a collection of a number of R of sets of stoichiometric coefficients, parameters A, b and E_a. The collection of data used in our studies was the one compiled in the detailed reaction mechanism of Kalghatgi et al.[34]. These authors present a fully detailed model in [35]; a more compact but nevertheless well-validated chemical mechanism is presented in [34]. The latter

was used in our studies. The kinetic scheme has been augmented with reaction data that describe the oxidation of a number of keto-hydroperoxides [36].

The transport processes are also modeled in detail. Fourier's law is used to determine the heat fluxes. Diffusion includes the basic Fick-Law, but also detailed transport effects like thermo-diffusion. For the determination of the diffusion coefficients, the approximation of Curtis and Hirschfelder[37] is used.

3.4.5.2 Treatment of the liquid phase

Convection inside the droplet is neglected. The liquid phase properties are calculated based on the data correlations taken from Reid et al. [38]. The approximation of Latini et al. [39] is used to calculate the heat conductivities. The (state-dependent) specific heat capacities $C_{p,i}$ of the liquid are computed according to the approximation of Rowlinson and Bondi [40]. The required properties to model the phase transition are also taken from Reid et al. [38]. The vapor pressure is calculated using the Wagner equation, and the enthalpy of vaporization is calculated by the correlation of Riedel and Watson [41].

3.4.5.3 Liquid/gas interface

A vaporization model accounts for the coupling of the liquid phase and the gas phase. A local phase equilibrium between liquid and gas is modeled by interface equations.

$$\phi_{\mathrm{vap}} = \frac{-\sum_{\mathrm{j_{vap}}} \mathrm{j_j^g} - \sum_{\mathrm{j_{vap}}} \mathrm{w_j} \sum_{\mathrm{i}} \mathrm{R_i} + \sum_{\mathrm{j_{vap}}} \mathrm{R_j}}{\sum_{\mathrm{j_{vap}}} \frac{\mathrm{p_j M_j}}{\mathrm{p\bar{M}}} - 1}$$

$$0 = \rho \cdot \mathrm{v_n} - \phi_{\mathrm{vap}} - \sum_{\mathrm{i}} \mathrm{R_i}$$

$$0 = \phi_{\mathrm{vap}}(\mathrm{w_i} - \epsilon_{\mathrm{i}}) + \mathrm{j_i} + w_{\mathrm{i}} \sum_{\mathrm{j}} \mathrm{R_j} - \mathrm{R_i}$$

$$\sum_{\mathrm{i}} \epsilon_{\mathrm{i}} \cdot \phi_{\mathrm{vap}} \cdot \Delta \mathrm{h_{vap,i}} + \mathrm{j_q^g} - \mathrm{j_q^l}$$

In these equations, ϕ_{vap} denotes the vaporization rate, w_{i} the mass fraction of species i, R_{i} the surface reaction rate of species i, j_{vap} the indices of the vaporizing species, p_{j} the partial pressure of species j, p the pressure, M_{j} the molar mass of species j, $\bar{M}$ the mean molar mass, ρ the density, v_{n} the normal velocity, $\epsilon_{\mathrm{i}} = \dot{\mathrm{m}}_{\mathrm{i}}/\dot{\mathrm{m}}$ the fraction of vaporizing mass, j_i the diffusion flux density of species i (gas phase), $\Delta h_{\mathrm{vap},i}$ the enthalpy of vaporization of species i and j_{q} the heat flux density.

Formulation for numerical treatment

In the spherically symmetric case (1D) the equation system is transformed into modified Lagrangian coordinates to overcome difficulties with the discretization of the convective terms [42]. This allows to implement a low Mach number approximation easily and to replace the momentum equation by $\frac{\partial \mathrm{p(r)}}{\partial \mathrm{r}} = 0$.

$$\left(\frac{\partial \mathrm{r}}{\partial \psi}\right)_{\mathrm{t}} = \frac{1}{\rho \mathrm{r}^2}$$

$$\frac{\partial \mathrm{w_i}}{\partial \mathrm{t}} + \mathrm{z}\frac{\partial \mathrm{w_i}}{\partial \psi} + \frac{\partial}{\partial \psi}(\mathrm{r}^2 \mathrm{j_i}) = \frac{\dot{\omega}_{\mathrm{i}} \mathrm{M_i}}{\rho}$$

$$\frac{\partial \mathrm{T}}{\partial \mathrm{t}} - \frac{1}{\rho \mathrm{c_p}}\frac{\partial \mathrm{p}}{\partial \mathrm{t}} + \mathrm{z}\frac{\partial \mathrm{T}}{\partial \psi} - \frac{1}{\mathrm{c_p}}\frac{\partial}{\partial \psi}\left(\rho \mathrm{r}^4 \lambda \frac{\partial \mathrm{T}}{\partial \psi}\right) - \frac{\mathrm{r}^2}{\mathrm{c_p}} \sum_{\mathrm{i}=1}^{\mathrm{n_S}} \mathrm{j_i c_{pi}} \frac{\partial \mathrm{T}}{\partial \psi} + \frac{1}{\rho \mathrm{c_p}} \sum_{\mathrm{i}=1}^{\mathrm{n_S}} \dot{\omega}_{\mathrm{i}} \mathrm{h_i M_i} = 0$$

Where ψ denotes the Lagrangian coordinate, c_{pi} denotes the specific heat capacity of species *i*, λ the heat conductivity, and h_i the specific enthalpy of species *i.*

The system of equations in the liquid phase is (analogous to the gas phase) also transformed into Lagrangian coordinates. Due to the time-varying mass of the droplet, however, one further transformation is necessary in order to fix the coordinate system to the drop surface (ψ_D^0 expressed in Lagrangian coordinates) [43].

$$\frac{d\psi_D^0}{dt} = -\left(\phi_{vap} + \phi_{stef}\right) \cdot r_D^2$$

where ϕ_{vap} denotes the vaporization mass flux and ϕ_{stef} the Stefan flux.

The resulting equation system in the modified coordinates t and η reads:

$$\left(\frac{\partial r}{\partial \eta}\right)_t = \frac{\psi_D^0}{\rho r^2}$$

$$\frac{\partial w_i}{\partial t} - \frac{1}{\psi_D^0}(\eta \vartheta^0)\frac{\partial w_i}{\partial \eta} + \frac{1}{\psi_D^0}\frac{\partial}{\partial \eta}(r^2 j_i) = 0$$

$$\frac{\partial T}{\partial t} - \frac{1}{\psi_D^0}(\eta \vartheta^0)\frac{\partial T}{\partial \eta} - \frac{1}{c_p \psi_D^0}\frac{\partial}{\partial \eta}\left(\rho r^4 \lambda \frac{1}{\psi_D^0}\frac{\partial T}{\partial \eta}\right) - \frac{r^2}{c_p}\sum_{i=1}^{n_S} j_i c_{pi}\frac{1}{\psi_D^0}\frac{\partial T}{\partial \eta} = 0$$

The resulting equations for the gas and liquid phase are discretized by central differences on non-equidistant grids and solved in a fully coupled way together with the interface equations.

3.4.5.4 Generic simulation software for reacting flows

The in-house Code INSFLA was used for the model simulations of droplet ignition and flame initiation scenarios. INSFLA solves transport equations for energy, species mass, momentum underlying the physics of these processes. It involves a detailed treatment of chemical source terms (gas-phase, surface reactions), molecular transport terms (heat conduction, diffusion, viscosity).

The equations form a system of Partial Differential Equations (PDE) involving time and pace as independent variables. INSFLA performs a numerical solution of this PDE with adaptive time-stepping, respecting tolerance criteria via an error control. The spatial discretization is also adaptive; this helps to accurately resolve spatial profiles of physical variables with steep gradients and sharp curvatures like they are typical in reacting gas phase flows.

The code also has the advantage of its large generality with respect to the systems that can be modeled. Especially, complex boundary conditions, like the ones found at the interface between an evaporating liquid or a solid (possibly with surface reactions) and the gas phase can be treated.

Applications include deflagration-based combustion processes in premixed, non-premixed and partially premixed systems, auto-ignition, Multi-phase phenomena (evaporation, condensation, deposition from gas to solid).

After discretization, one obtains a large system of ordinary differential and algebraic equations. The resulting differential-algebraic equation system is solved by the linearly implicit extrapolation method LIMEX [44]. This method was conceived for the solution of such large and stiff differential-algebraic systems. In addition, efficient numerical methods are implemented for the calculation of the resulting block tri-diagonal matrices and the solution of the linear equation systems [43]. Due to the simultaneous perturbation of the sparse Jacobian, the required number of function evaluations does not depend on the number of grid points. This particular feature helps to perform highly resolved, accurate physical studies at reasonable computational costs.

The program code is written in FORTRAN. Computations are performed on a regular single PC using Linux as an operating system. The simulations yielding the presented results use the full capacity of the mentioned hardware.

3.4.6 Modeling of hot-particle-induced ignition

Besides oil-fuel droplets, detached particles are assumed to be a potential root-cause of pre-ignitions. In order to determine the gas-phase ignition potential caused by a hot particle inside the combustion chamber, a detailed sub-model of a single particle had to be established.

Whereas oil droplets accelerate ignition processes by evaporating reactive species, particles induce an ignition by heat transfer. The particles inside a cylinder are heated up by regular combustion cycles. Moreover, the particle itself could increase the surface temperature by exothermal reactions. Since the composition and the reactivity of such detached particles are unknown, the hot particle was simplified as a hot surface. Only the heat transferred from the particle surface to the reactive gas-phase environment was considered. The general advantage of this modeling approach is that it is valid for reactive and non-reactive particles. Figure 3-26 shows the numerical grid used in this submodel.

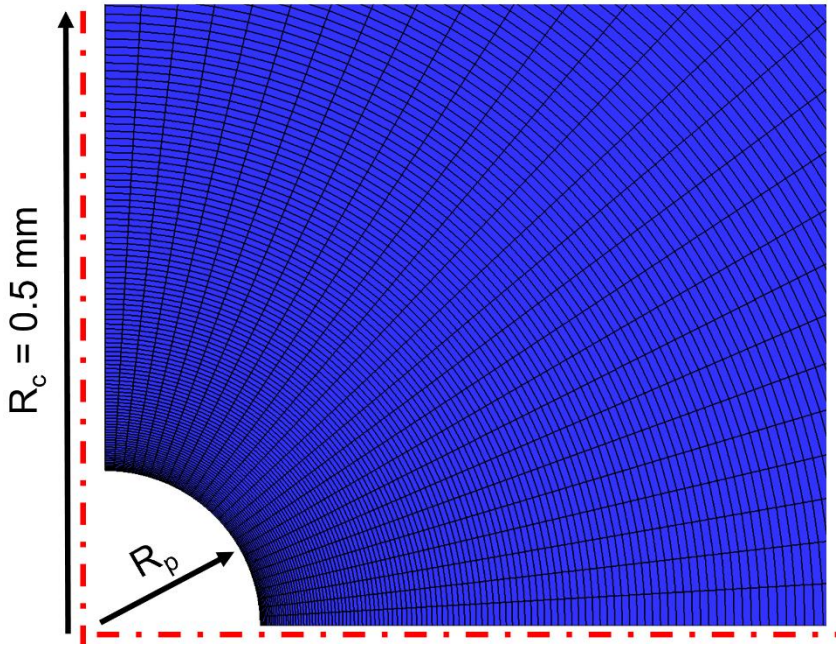

Figure 3-26: Hot particle ignition sub-model.

A two-dimensional structured radial grid was set up to model the heat transfer problem numerically. Double symmetry conditions were used to reduce the model size to a 90° sector. The overall simulation domain was limited to a radius of 3.125 mm discretized with 8,100 cells (d_R x d_φ x d_z = 300 x 27 x 1). The particle radius (R_p) is set to 125 µm, representing the typical size of the piston crevice gap. In order to capture the sharp increase of the gas temperature near the hot surface, the boundary layer had to be resolved. Therefore, the cell size at the wall was set to 1 µm. Towards the outer end of the simulation domain, the cell size increased to 20 µm using a stretching factor.

The gas-phase was modeled as a mixture of air (76.8 %-m/m N_2, 23.2 %-m/m O_2) and fuel. The fuel was represented as a TRF-surrogate. The three components (iso-octane, n-heptane, toluene) were mixed according to the RON and MON measurements to mimic the actual fuel reactivity. By applying the modified linear-by-volume method of Morgan et al. [45], a mixture composition could be found iteratively. Table 3-9 shows the result for the fuel used in this project.

Table 3-9: TRF representation of fuel.

Fuel measurement	Value [-]
RON	96.5
MON	86.0
Surrogate species	**Mass fraction [-]**
iso-Octane	0.1246
n-Heptane	0.1565
Toluene	0.7189

The chemical reaction kinetics were calculated in the gas phase using the semi-detailed TRF mechanism of Andrae et al. [46], including 137 species and 633 reactions. In order to determine the ignition delay time, a consistent ignition criterion was used. If an established propagating flame front reached a critical radius (R_c) of 0.5 mm, the flame was assumed to be self-sustaining. The time to reach that criterion was defined as ignition delay time. The critical radius was set according to Kalghatgi et al. [47], who published the critical radius for n-heptane/air mixtures.

4 Test environments

4.1 IVT Test setup

This FVV project was a cooperation between different institutes with different infrastructural environments on their testing facilities. Therefore, the institutes who did investigations on the testbed had to compare their measurement data from the testbed to avoid deviations between the different test systems. These comparisons were made during the commissioning phase between the IFKM in Karlsruhe and the IVT in Graz.

4.1.1 Test engine

For the experimental investigations on the testbed, a turbocharged gasoline engine with modifications to resist higher cylinder pressures has been used. The full engine provided by Ford® was a three-cylinder gasoline engine with a displacement of 999 cm³. The engine is boosted with a one-stage waste-gate turbocharger and a 200bar injection system which is centrally located. A more detailed engine description can be found in Table 4-1. Due to the earlier combustion during the compression stroke caused by low-speed-pre-ignitions, the cylinder pressure during such combustion anomalies can rise to the upper detection border. In order to withstand combustion cycles with such high damage potential, the engine was equipped with reinforced connecting rods and non-serial pistons. The pistons were redesigned for pre-ignition resistance, which leads to an increased piston land width. The most common damage case in consequence of pre-ignitions is a fault of the piston ring land. With these modifications, the engine can resist a calculated average cylinder pressure of 140 bar and a calculated maximum cylinder pressure of about 185 bar. All other engine parts were parts from the serial production engine.

Table 4-1: Test Engine data.

Ford Fox ECO-Boost	
Bore	71.9 mm
Stroke	82 mm
Cylinder Number	3
Total Displacement	999 cm³
Compression ratio	10.5 : 1
max Torque @1500-4000rpm	170 Nm
max Power @6000 rpm	92 kW
max engine speed	6800 rpm

Indifference to the test engine in Karlsruhe, the test engine in Graz had no optical access but was prepared for in-cylinder-pressure sensing on all three cylinders. The cylinder pressure indicator system will be described in chapter 4.1.2. Ford provided an engine control unit (ECU) with full access to set and control engine-specific parameters.

4.1.2 Testbed

An asynchrony electric motor and an eddy current break arranged in a tandem design worked together on the automated testbed. The asynchrony electric motor has been used to tow the engine. The tandem system, as well as the engine, were mounted on a decoupled baseplate. The test cell was also equipped with different fuel supply lines to change between different liquid fuels quickly. Furthermore, a supply for gaseous fuels was accomplished. The test cell equipment also included connecting units for conditioning systems. In combination with conditioning devices, we were able to control the engine coolant temperature, the temperature of the intake air, and the fuel temperature in a wide range.

Measuring equipment

The measuring equipment for these investigations included slow and fast data acquisition. The testbed system recorded the slow data. The fast data acquisition recorded the fast data crank angle-resolved and was used to detect combustion anomalies.

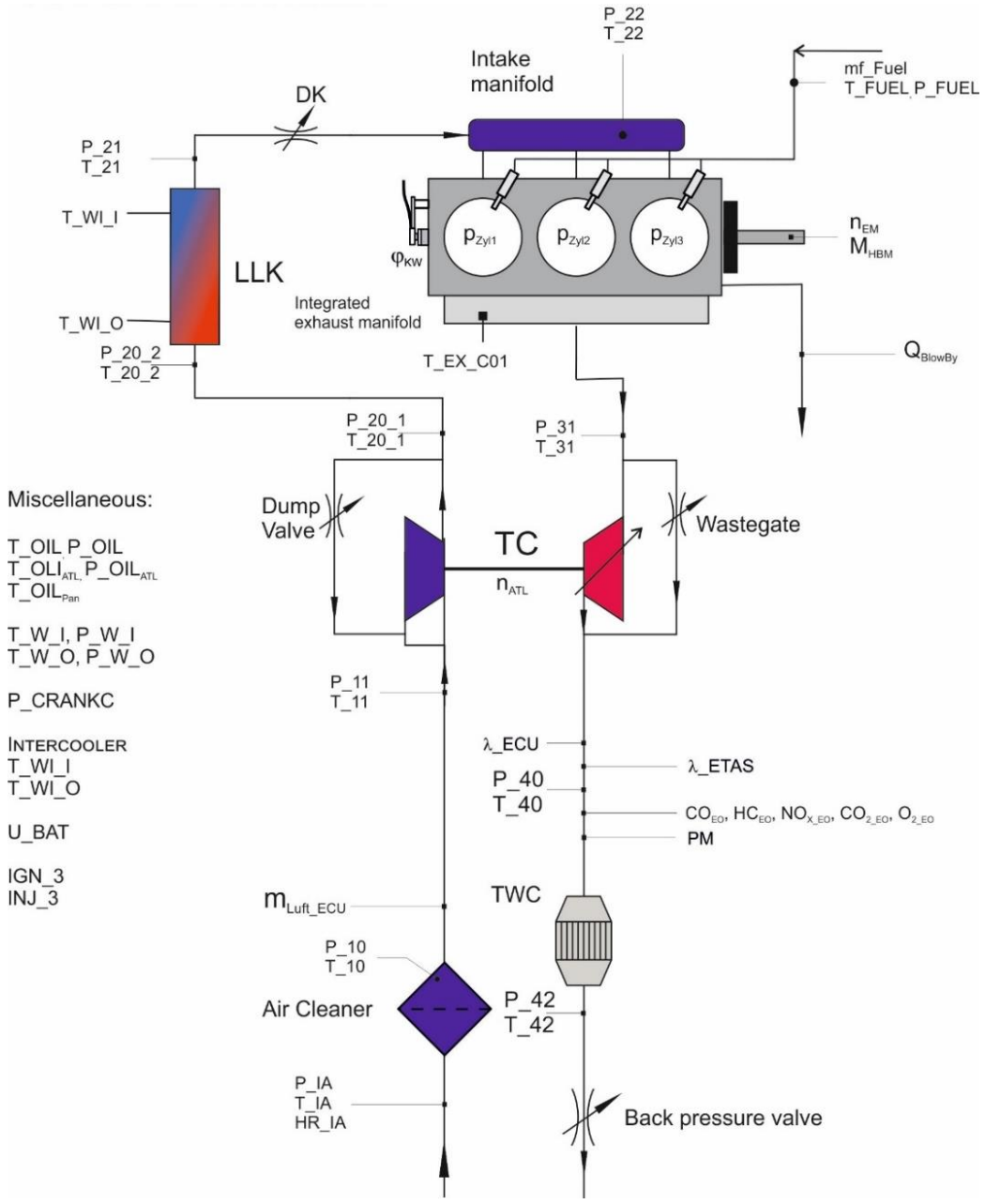

Figure 4-1: Testbed scheme.

A scheme of the sensors installed on the testbed is shown in Figure 4-1. The sensors for pressure and temperature were installed at important positions on the intake and exhaust system. To regulate the intake gas temperature, a gas-to-liquid heat exchanger indifference to the serial engine was used. The crankcase ventilation was also not connected to the intake system. Instead, the blow-by gas was fed to the exhaust gas extraction after the blow by measuring device. We were able to measure the engine emissions upstream of the three-way catalyst. The soot emissions were measured with an AVL Smokemeter.

On the one hand, the focus of the investigations in Graz were thermodynamic variations and the influence on LSPI occurrence. On the other hand, a considerable part investigated oil droplets on suspicion to trigger pre-ignitions.

To detect combustion anomalies, i.e., low-speed-pre-ignitions in Graz, we used the indication system Indicom from AVL, Table 4-2. The test engine was equipped with high- and low-pressure sensors. For the cylinder-pressure-indication three, water-cooled sensors (GC24DK) were deployed. In order to ensure longer service life, sensors with an overload of 300 bar were used. Low-pressure indication transducers were installed at the test engine's intake and exhaust ducts to align the recorded pressure signals with the CFD-simulations. For this purpose, piezoelectric pressure sensors with cooling adapters and a connection to determine the absolute pressure were used. More technical information can be found in Table 4-3.

Table 4-2: Indication measurement system.

Manufacturer	**AVL**
Indication system	IndiSet Advanced 631
Charge amplifier	MicroIFEM
Crank angle sensor	AVL 635C
Software	Indicom v2.0

Table 4-3: Pressure transducer

Position		Cylinder	Intake	Exhaust
Manufacturer		AVL	AVL	AVL
Sensor type		GC24DK	GU21C	GU21C
				
Measuring range	bar	0 … 250		0 … 250
Overload	bar	300		300
Sensitivity	pC/bar	19		35
Linearity	% FSO	≤ ± 0.2		≤ ± 0.3

4.1.3 Oil injection system

We set up a system to bring a specific amount of lubricants into the test engine's inlet duct for the investigations of different oil types and ionic liquids. With this injection system, we maintained a constant contribution of the liquid to be investigated in the test engine. The oil input should represent the oil transport in a real engine through the intake system caused by the turbocharger's oil leakage, crankcase ventilation system, and the valve stem sealings. The liquids were pumped with a peristaltic pump through a hose to a stainless steel hose close to cylinder three's intake duct. The schematic setup for the oil injection is shown in Figure 4-2.

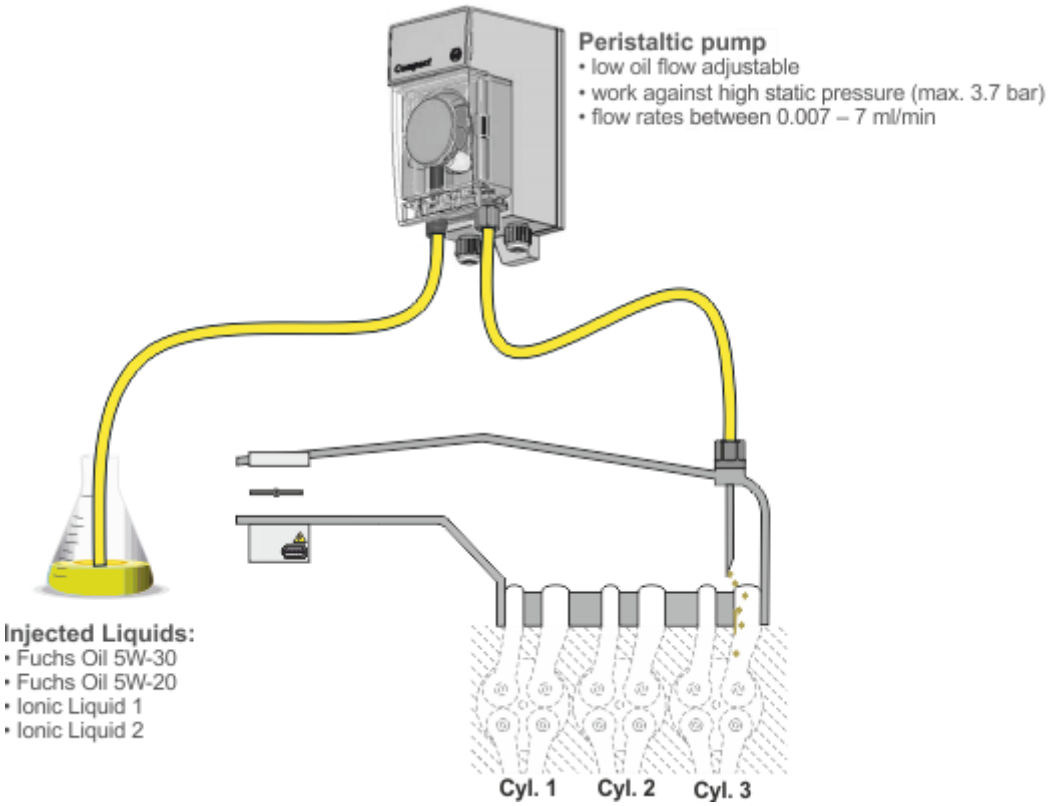

Figure 4-2: Injection system.

For each injection test, the peristaltic pump was adapted to a specific liquid mass flow depending on the liquid density and the operating point. The oil amount pumped through the injection lance was measured with a highly accurate scale for exactly one minute for the setup process. Due to this procedure, it was possible to set the oil mass flow by adjusting the peristaltic pump's rotation speed to the desired value. The used pump was able to inject a mass flow up to 7 ml/min against a boost pressure of 3.7 bar absolute pressure. Between tests with different liquids, the injection equipment has been cleaned and changed to avoid contamination of the new test liquid with the old one. In this way, the injection setup was a sufficient tool to investigate the LSPI tendency of different lubricants and compare the number of occurred pre-ignitions during a test sequence. The test methodology for the injection tests is explained in chapter 3.2.3.

4.1.4 Oil source detection

In order to detect relevant oil droplet sources which are under suspicion to influence the LSPI behavior, different measurement systems were used. With three different oil consumption measurement systems, we were able to split the overall oil consumption of the test engine and give information about the quantity of various engine parts' oil consumption

There are four mechanisms of how engine lubricant can get into the combustion chamber and act somehow as an LSPI trigger or accelerator. These oil routs into the combustion chamber are the:

- crankcase ventilation system
- turbocharger shaft
- inlet valve shaft sealing
- cylinder surface and reverse blow-by

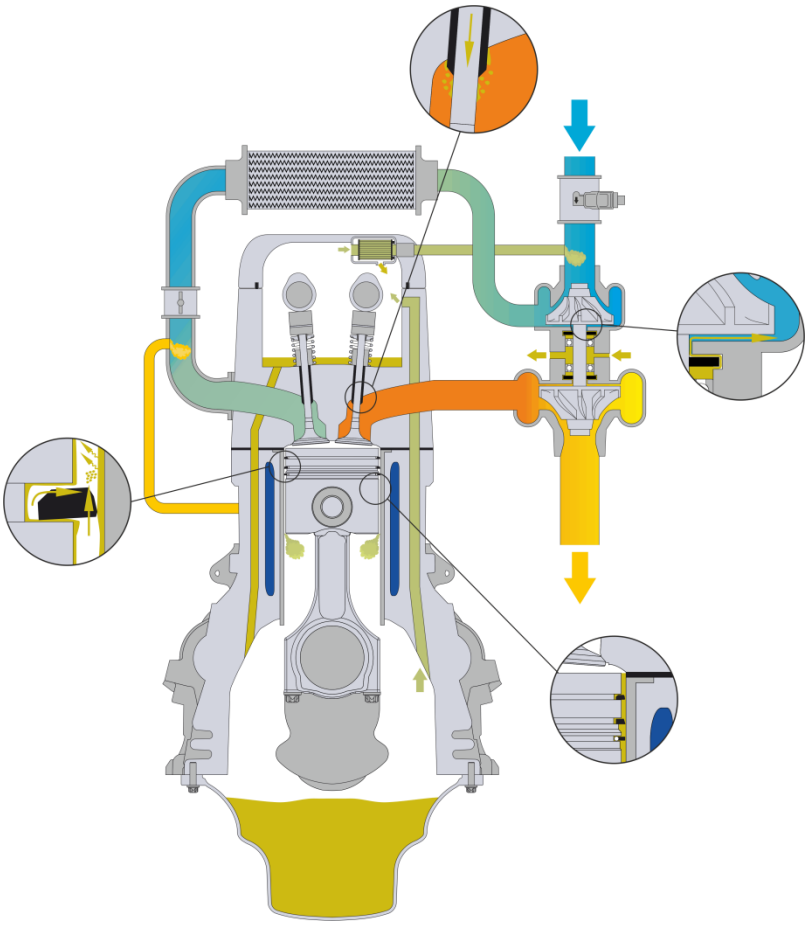

Figure 4-3: Oil sources of internal combustion engines.

The test engine is equipped with two crankcase ventilation systems. One for non boosted operating points and the other for boosted operating points. In our investigations, the crankcase ventilation system for boosted operation points was connected, as only this blow-by route course was active at the LSPI investigation points. Because it is impossible to measure the in-cylinder oil consumption and the oil loss through the valve shafts with our system, we calculated this oil amount as residual of the test engine's overall oil consumption. The calculation mythology is explained in chapter 3.2.4.

Crankcase ventilation oil consumption measurement

A special filtration device has been designed and used to determine the oil amount included in the blow-by-gas. Therefore, two paper filters were fixed in the filtration devices. In order to avoid gas flow past the filters, the filter papers were fixed around the circumference with special retaining rings. The oil amount in the blow-by gas was determined by weighing. For this purpose, both filter papers were weighed before and after the test run. A three-way valve in the experimental setup allowed us to by-pass the filtration unit during the conditioning phase to avoid wrong measurements. The filtration unit and the connection hose from the test engine to the filtration unit were heated up to 120°C. This measure is necessary to avoid condensation of water or fuel in the connecting hose and the filtration unit. This condensate would also be deposited on the filter papers and would misrepresent the measurements. Upstream and downstream of the filters unit pressure measuring points were attached to observe the filtration unit's pressure drop during the measurement. With this information, the measurement time was adjusted under the observation of the pressure ratio. After the measurement device, a flow meter for blow-by was installed to compare the blow-by mass flow with and without the filtration unit.

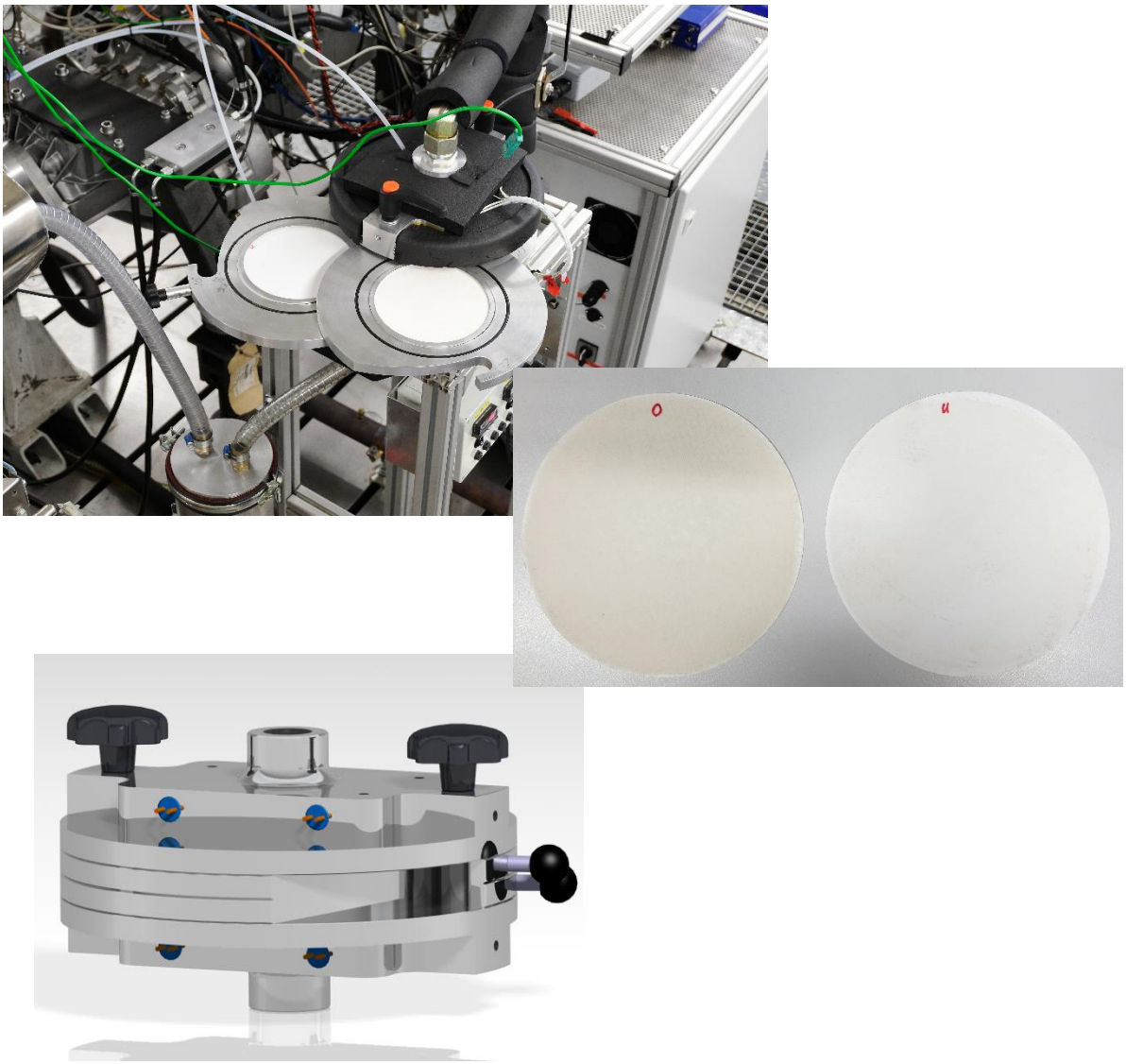

Figure 4-4: Blow-By oil measurement system.

Turbocharger oil consumption measurement

Another oil consumption measurement device has been used to measure the turbocharger oil consumption. Turbocharger lubrication is one of the reasons why oil is transported through the intake system into the combustion chamber. The amount of oil loss through the turbocharger shaft depends on many different boundary conditions. For example, the surface of the turbocharger shaft, the bearing system of the exhaust gas turbocharger, and the lubrication system of the turbocharger influence oil consumption. Also, pressure conditions in the intake system and an increased crankcase pressure influence the transport of the turbocharger lubricant from the lubrication area along the impeller shaft into the intake system. For instance, operating conditions with low pressure along the compressor wheel and increased crankcase pressure oil can be transported into the intake system.

To measure the turbocharge system's overall oil loss, we installed a standalone measuring system on the testbed. This measuring system was able to weigh the oil consumption online. Therefore, the turbocharger's oil supply and conditions are integrated into the measurement device and work without a connection to the engine. The standard oil lubrication hoses from the test engine have been disconnected. The turbocharger was connected to the measurement device and supplied with oil. The scheme of the turbocharger oil consumption measurement device is shown below, Figure 4-5.

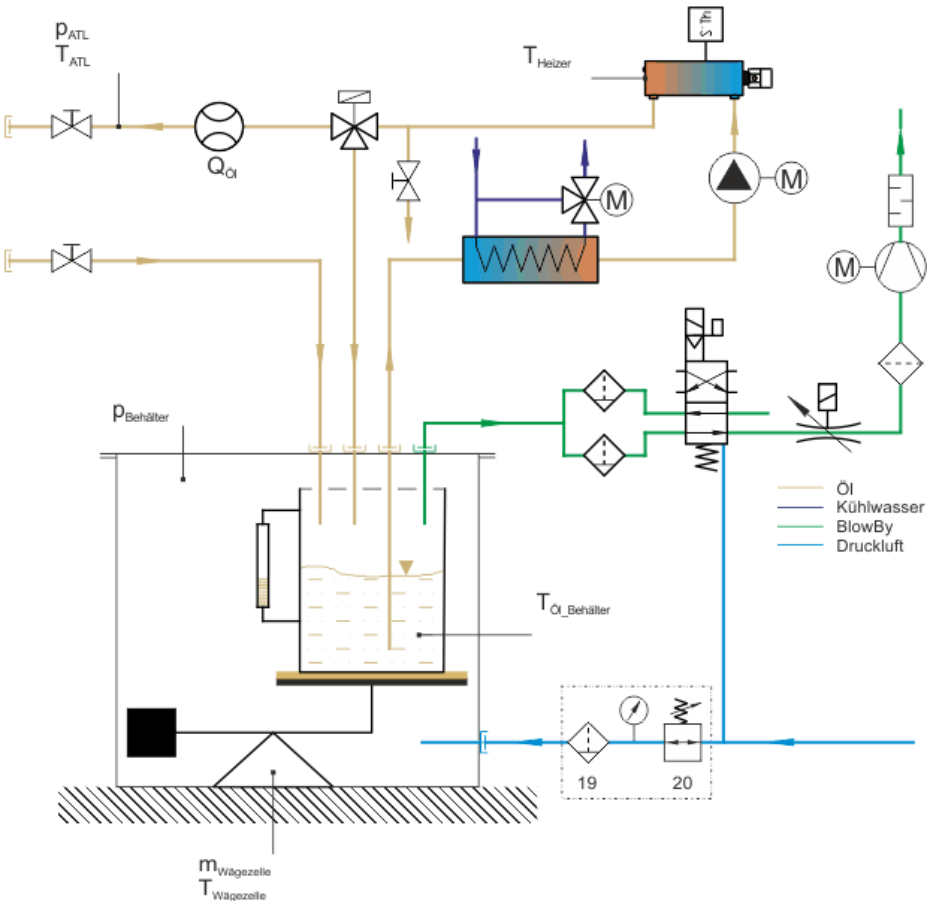

Figure 4-5: Turbocharge oil consumption measurement.

To compensate the pressure difference between the crankcase and the containment of the measuring device, a vacuum pump was installed to apply the containment pressure.

Overall oil consumption measurement

To divide the oil consumptions by their origins, we had to measure the test engine's overall oil consumption. Different methods to evaluate the overall oil consumption of internal combustion engines, shown in Figure 4-6, exist. They can be split into conventional measurement methods and analytical chemical measurement methods. Measurement methods such as gravimetric or volumetric methods require more operating time to obtain sufficient results. Correspondingly long test sequences are needed. For the chemical measurement methods, special measuring devices are necessary, but with these methods, an entire grid measurement can be executed without long measuring times per measuring point.

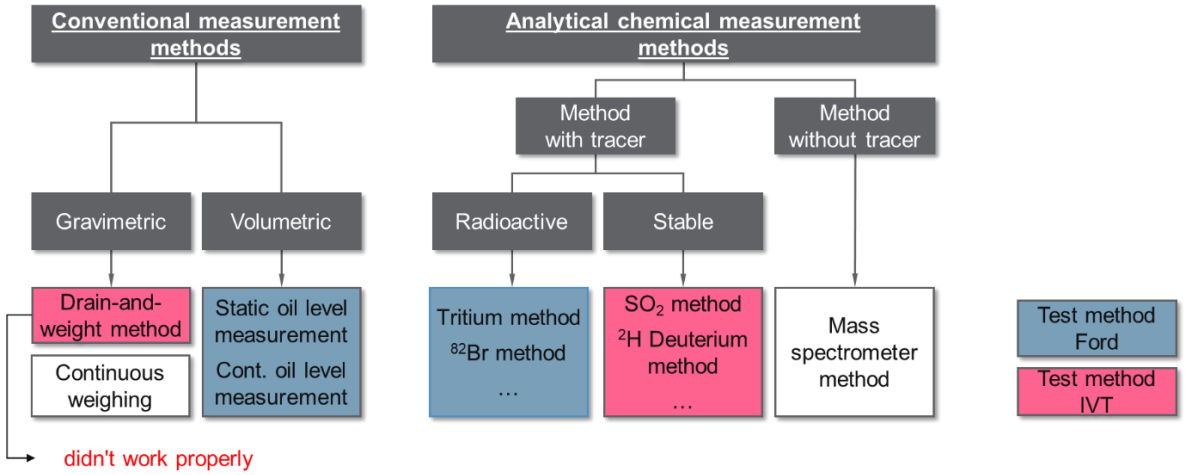

Figure 4-6: Overview overall-oil-consumption measurement methods [48].

We tried to determine the overall oil consumption with the "Drain- and weight method" in a first step. With this measurement technique, it was impossible to gain reproducible results for the overall oil consumption on the testbed. Although we have always strictly followed the test procedure, we only could achieve results with a large spread in oil consumption. For valid results, we would have to run the engine for several hours in an operating point and use the static oil level measurement method to gain a more considerable amount of oil consumption which could be detected more reliable. Because such time-consuming tests would have postponed further investigations, we decided to use a tracer method to evaluate the engine's overall oil consumption. We determined the test engine's oil consumption with the SO_2 method in a grid measurement. The measurement device lube sense from V&F detects the SO_2 concentration in the exhaust gas with which, in a post-processing algorithm, the oil consumption was calculated. We also tested a second oil consumption measurement method. The second measurement method also belongs to the group of tracer methods. For this method, the engine oil was mixed with deuterium as a tracer. With the analyzing device connected to the exhaust pipe, the reaction product of deuterium in the exhaust gas was measured, and the oil consumption of each measurement point was calculated. [48]

4.1.5 CNG setup

For the investigations with CNG (Compressed Natural Gas) as fuel, we had to change the engine setup compared to the direct gasoline injection. For the gaseous mixture preparation, we used a multi-point-injection-system integrated into the intake manifold. Therefore, the mixture preparation happens in each cylinder's intake port and not directly in the combustion chamber. The high-pressure natural gas of 300 bar must be reduced in a first regulation step to 5 bar to use this injection system. As shown in Figure 9, the regulation unit decreased the gas pressure independence of the boost pressure to a maximum injection pressure of approximately 4bar. The gas injection valves were connected through special hoses to the intake manifold. The intake manifold has been equipped with inner extension pipes to release the CNG gas nearby the intake valves. These measures should avoid bad mixture behavior in consequence of charge motion between the cylinders.

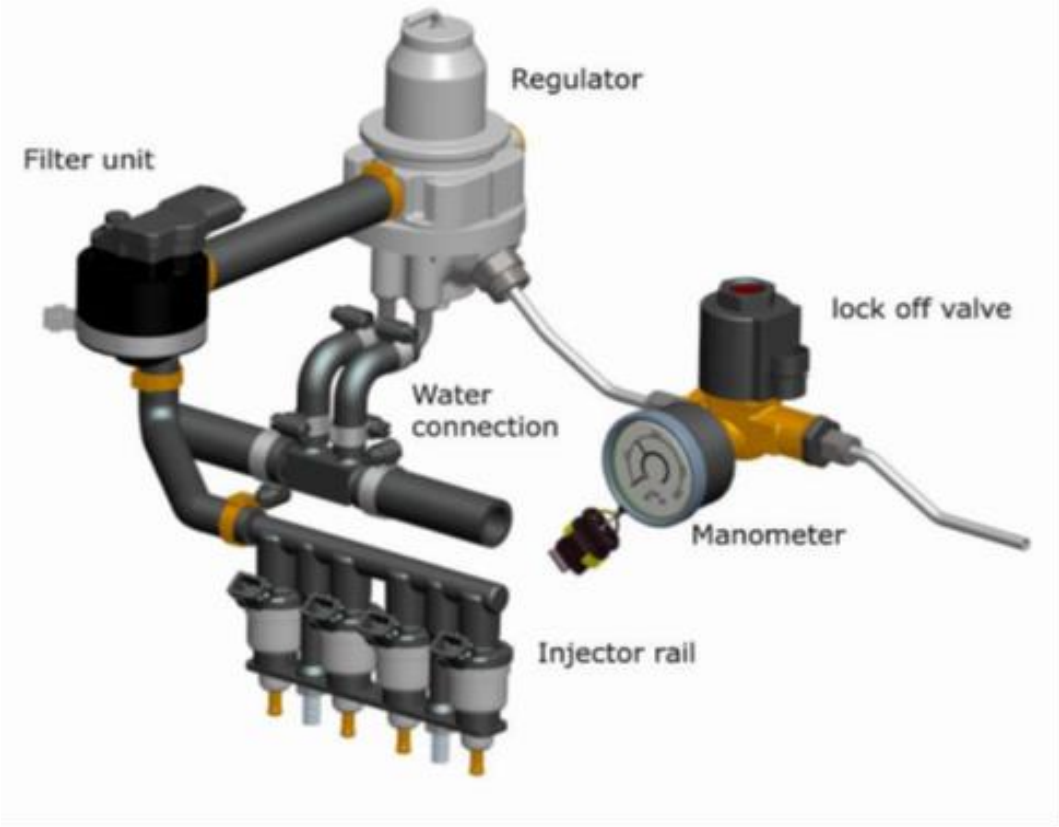

Figure 4-7: CNG MPI system.

4.1.6 Hardware variation

A variation of the honing pattern was investigated to determine the influence of hardware changes on low-speed pre-ignitions. For this purpose, an engine block was intentionally produced with a rougher surface through the honing process. The honing process was carried out and performed by "NAGEL Maschinen- u. Werkzeugfabrik Gmbh" on Ford's unfinished engine block. For this purpose, the honing surface came with a higher R_{vk} compared to the original honing from Ford. The idea behind this was to increase the oil storage capacity. In this experiment, the pistons and piston rings were not replaced to investigate only the effects of the honing surface on the pre-ignition behavior. Table 4-4 shows the honing parameters of the serial honing. For the hardware variation, the surface parameter R_{vk} has been increased to a value of 2 µm.

Table 4-4: Standard liner surface parameters.

Production surface values:								
Cv	**Ra**	**Rz**	**R3z**	**Rk**	**Rpk**	**Rvk**	**Mr1**	**Mr2**
[µm]	*[µm]*	*[µm]*	*[µm]*	*[µm]*	*[µm]*	*[µm]*	*[%]*	*[%]*
0,078	0,319	4,215	2,484	0,885	0,541	0,57	10,25	88,3

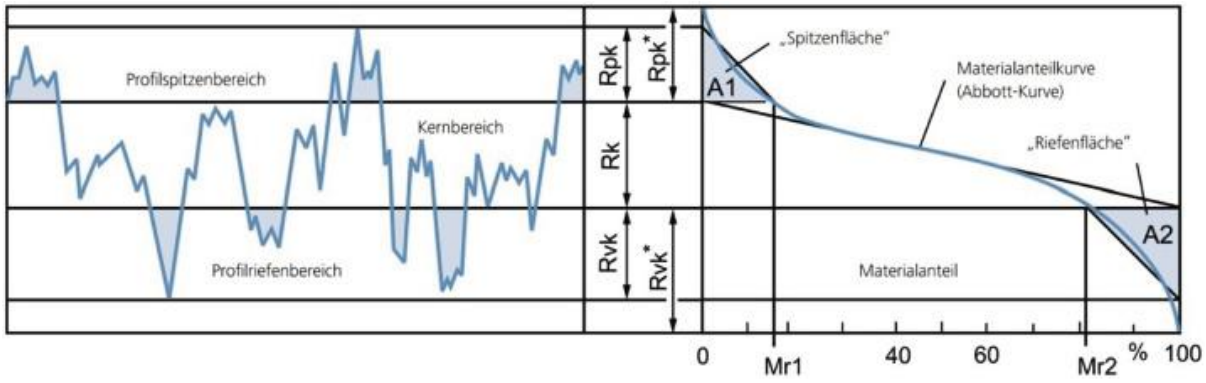

Figure 4-8: Definition Abbott-Firestone-Curve DIN EN ISO 13565-2 [49].

4.2 IFKM Test engines and operating media

The specifics of the test engines used and the engine operating media employed are presented below.

4.2.1 Test engines

Two Ford FOX 1.0l EcoBoost engines were used to implement the test methodology. These are downsized turbocharged gasoline engines with gasoline direct injection and variable valve train (intake and exhaust valve spread). Both engines have reinforced connecting rods and pistons with cast-in ring carriers and are therefore more resilient to pressure peaks and gradients for the pre-ignition tests. Table 4-5 shows the main engine specifications.

Table 4-5: Technical data of the test engines [50].

Manufacturer	Ford
Designation	Ford FOX 1.0L EcoBoost
Displacement	999cc
Valve train	DOHC
Valves / Cylinder	4 / 3
Bore	71.9 mm
Stroke	82 mm
Compression ratio	10.5:1
Fuel system	DI, central injector position
Ignition system	Individual COP with integrated driver

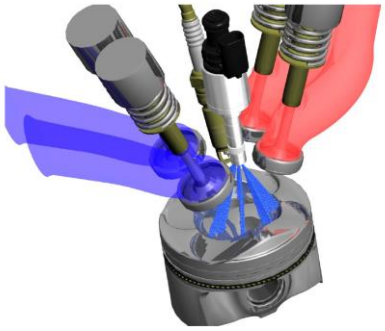

Both engines have cylinder heads with mounting holes for pressure sensors, as well as pressure sensor inserts in the exhaust manifold and airbox for low-pressure measurement. The crankcase ventilation path for full-load operation was routed directly to a catch basin for all tests (part-load path was closed). All auxiliaries were disassembled except for the cooling water pump, and the thermostats for external coolant conditioning were blocked open. The dual-mass flywheel is blocked by spot welds for the tests.

The use of a PROtroniC prototyping engine control unit enables fully variable access and intervention to all operational parameters. Access to the control unit and the recording of measured values is carried out by means of the ATI VISION software.

The test environment provides the dynamometer, which is connected to the engines empty gearbox shaft via a cardan shaft with a cardan disc, as well as the conditioning for cooling water and charge air, and records pressure and temperature at all relevant measuring points via a MORPHEE 3 test stand data acquisition system. An AVL KMA4000 is used as the fuel measuring system.

A Kistler KiBox is used for pre-ignition detection and combustion analysis. High-pressure analysis is carried out via three water-cooled piezoelectric pressure sensors of type Kistler 6041B in the cylinder head and low-pressure analysis is carried out on the exhaust side with a water-cooled piezoelectric pressure sensor of type Kistler 4049A10 in the exhaust manifold and on the intake side with a piezoelectric pressure sensor of type Kistler 4075A10 in the airbox.

4.2.2 Optical engine system

For the setup of the optical engine system, the second engine was additionally equipped with three optical access points. Two frontal Ø10.6 mm bores in the cylinder head are accessible through the integral front cover of the engine. Access sleeves with a "working diameter" of Ø8 mm can be inserted here, which can be used interchangeably for combustion chamber illumination and observation. Between the intake valves, a further Ø6.6 mm hole is provided under the airbox in the cylinder head, which allows an access sleeve with a "working diameter" of Ø4 mm. Endoscopic observation is not feasible here due to the small optical diameter for the specific investigation objectives. These boundary conditions led to the optical systems shown in Figure 4-9.

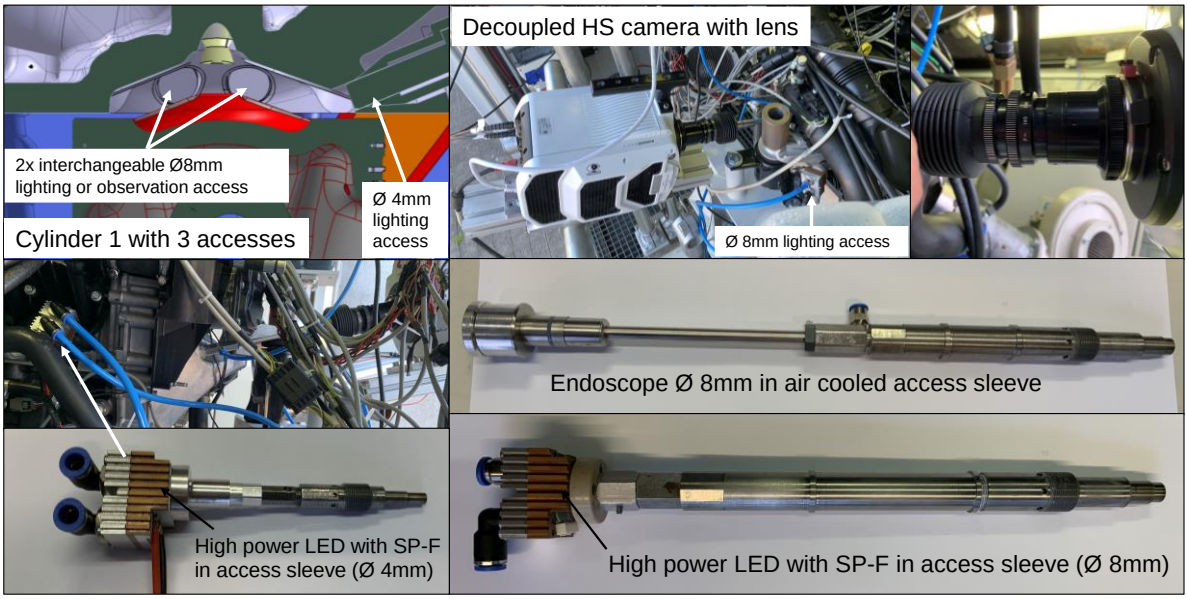

Figure 4-9: Composition of the optical engine system.

Two water-cooled high-power LED lighting systems were developed for the engine lighting, which allow the light spectrum to be adapted to the specific LIF requirements via a filter insert. The illumination color blue resulted from the spectral fluorescence requirements as well as the highest LED beam power available on the market. The observation access sleeve for holding the Ø8 mm Richard Wolf endoscope is additionally equipped with a compressed air-cooling system. Due to the high engine acceleration amplitudes, the camera system (HS camera + lens) had to be decoupled and was mounted fixed to the test bench. Since the movement amplitudes were relatively low during operation, no optical impairment occurred. A Phantom 1612 with 12bit COMS (Bayer-sensor) was used as the HS camera.
The resulting observation spaces of the cylinder one combustion chamber for the specific optical engine setups are shown in Figure 4-10. In engine operation under pre-ignition boundary conditions, the exhaust-side Ø8 mm access showed an increased tendency for window fouling compared to the intake-side Ø8 mm access. For this reason, the majority of all imaging was performed with optical setup 2. In the trade-off between illumination and observability, the focus on observability has proven to be more effective.

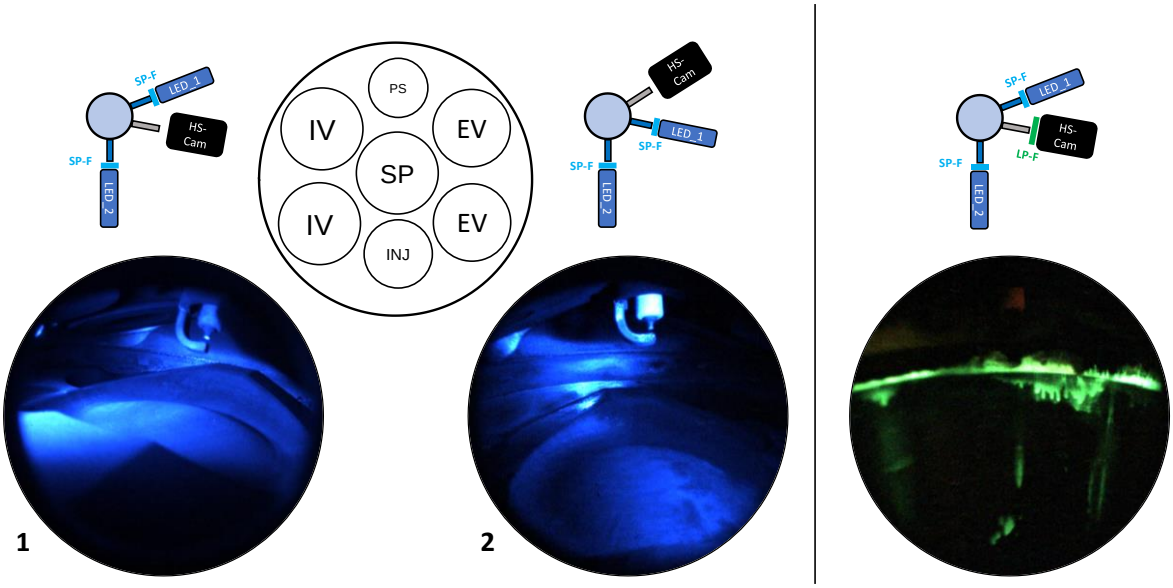

Figure 4-10: Optical setup 1 and 2 with corresponding combustion chamber view fields.

4.2.3 Engine operating media

Figure 4-11 shows the different boiling properties of the fuels used. Due to the increased proportion of high-boiling components in the High LSPI fuel, the resulting evaporation behavior in engine operation means that greater spray/ liner interaction is to be expected [18]. This results in a higher pre-ignition level, particularly necessary for the optical pre-ignition characterizations, which is why this fuel was chosen for the majority of the tests. It was provided by the company Coryton Advanced Fuels. In the chapter "Macroscopic PI characterization: Generation of pre-ignitions", a pre-ignition reference to the Super E5 fuel from Figure 4-11 is carried out.

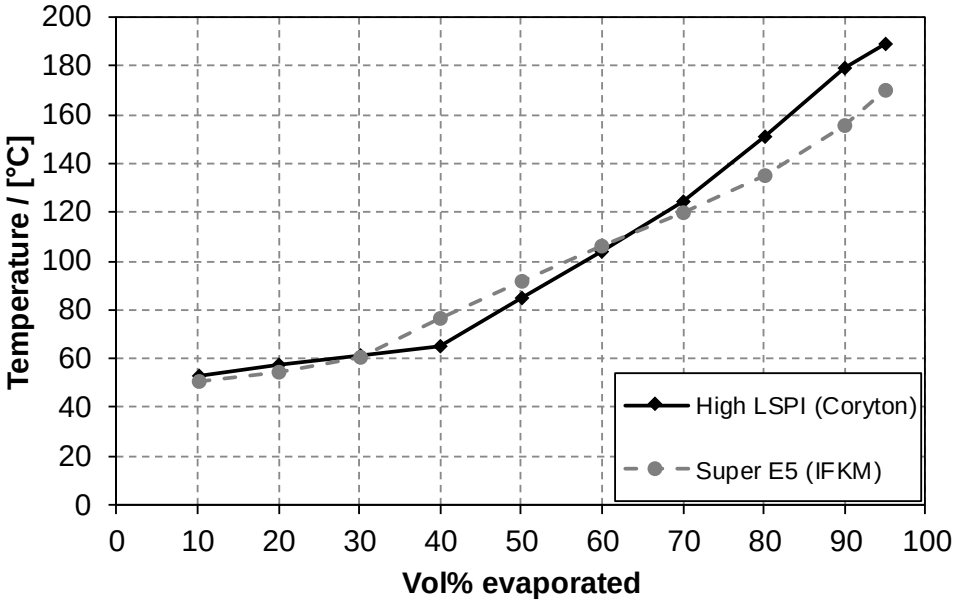

Figure 4-11: Distillation curves of the used fuels.

The influence of different engine oils on the pre-ignition rate turns out to be far more significant. In the present investigations, two different engine oils supplied by Fuchs Motorenöle were examined. The additive components detected in a fresh oil analysis are listed in Table 4-6 for comparison.

Table 4-6: Additive characteristics of the used engine oils.

		Fuchs TITAN Supersyn F Eco B SAE 5W 20	**Fuchs Titan Supersyn F Eco DT 5W 30**
Calcium	mg/kg	2015	2842
Magnesium	mg/kg	5	14
Boron	mg/kg	1	84
Zinc	mg/kg	871	1073
Phosphorus	mg/kg	741	907
Barium	mg/kg	0	0
Molybdenum	mg/kg	1	0
Sulfur	mg/kg	2256	2175

Hereafter the oils are referred to as Fuchs 5W20 and Fuchs 5W30.

5 Results and discussion

5.1 IVT results

The following results are a summary of the experimental investigations on the testbed. This summary is intended to show the most important correlations and underpin the mechanism that has been worked out.

5.1.1 Parameter variation

As explained, the parameter variation investigation's goal was to determine the independence of different thermodynamic boundary conditions on the occurrence of LSPI events. For this purpose, one thermodynamic parameter has been changed for each variation run.

A variation of the fuel type has been carried out in the beginning. Compared to the following investigations, the low level of pre-ignition is justified due to the used engine oil Fuchs 5W-20, Figure 5-1: Comparison of engine fuel type regarding LSPI events and evaporation curves. We later changed the engine oil to Fuchs 5W-30 because this oil showed a higher number of LSPI events during the investigation time of 30 000 cycles. After the general investigations to specify the engine oil and the fuel type used for further tests, we started the engine parameters studies.

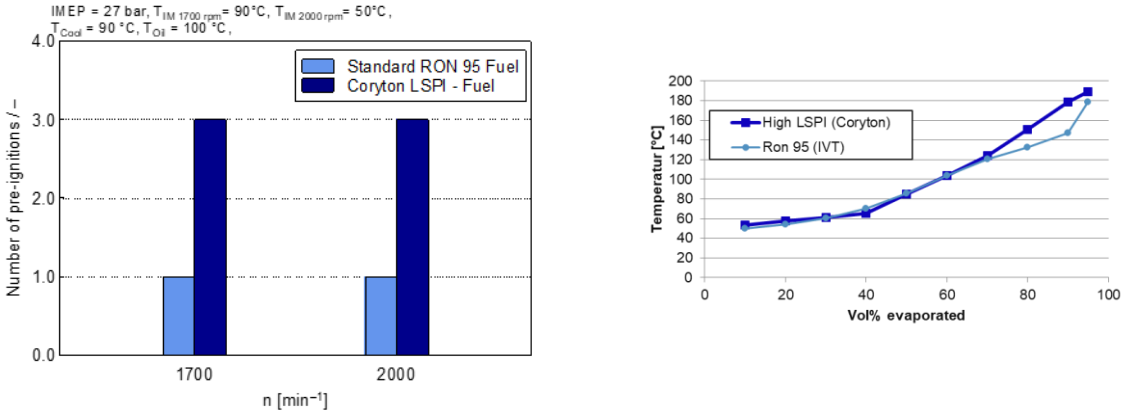

Figure 5-1: Comparison of engine fuel type regarding LSPI events and evaporation curves.

A variation of coolant temperature showed the already observed behavior regarding pre-ignitions demonstrated in [51]. With an increase in the coolant inlet temperature, the number of attended LSPI events decreased. This behavior could be shown for two different engine speeds, see Figure 5-2. These tests also show the difference between the oil types in the absolute number of pre-ignition during the test sequence.

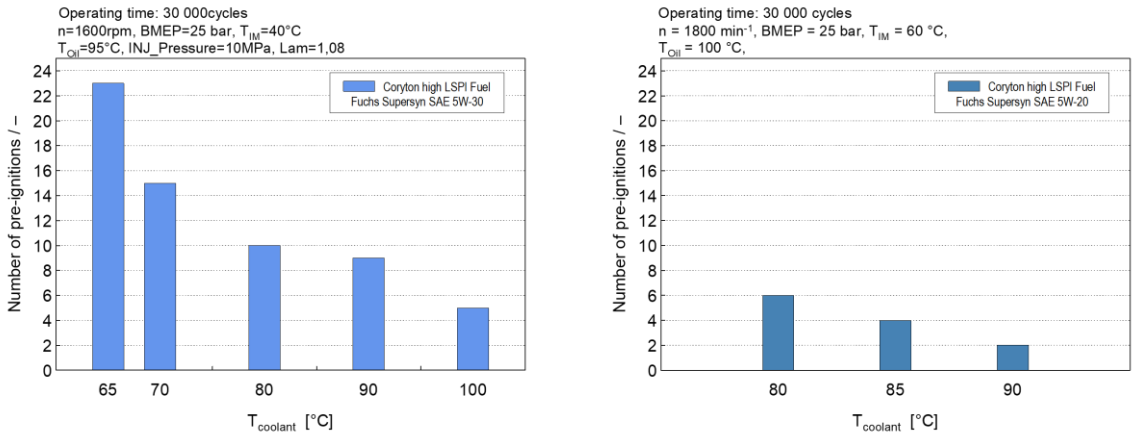

Figure 5-2: Variation in coolant temperature.

A dependence of pre-ignition events on the engine speed could also be observed, shown in Figure 5-3. Therefore, variations with different intake air temperatures have been investigated. The number of pre-ignitions rises with higher engine speed. Also, the higher level of pre-ignitions with Fuchs 5W-30 engine oil could be confirmed.

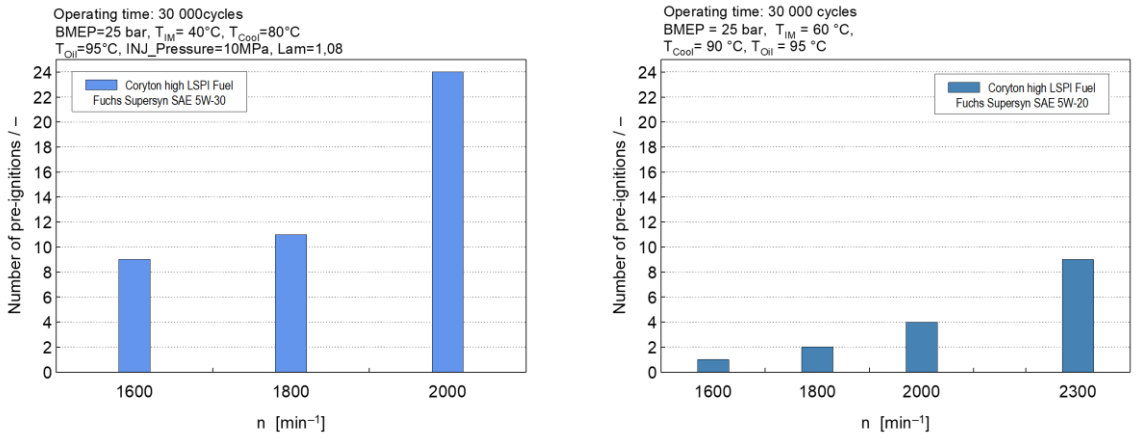

Figure 5-3: Variation of engine speed.

Also, a variation of the injection pressure and the fuel supply temperature were carried out, shown in Figure 5-4. The variation of injection pressure didn't show a clear trend. The highest number of pre-ignitions occurred with the injection pressure of 100 MPa. During this variation sequence, the start of injection was set to 250 °CA BDTC. The variation of the fuel temperature from the minimum possible temperature of 19°C to the maximum possible temperature of 42°C showed decreased pre-ignition with increased temperature. This behavior agrees with the assumption that better vaporation conditions lower the fuel liner interaction, leading to a reduced formation of deposits.

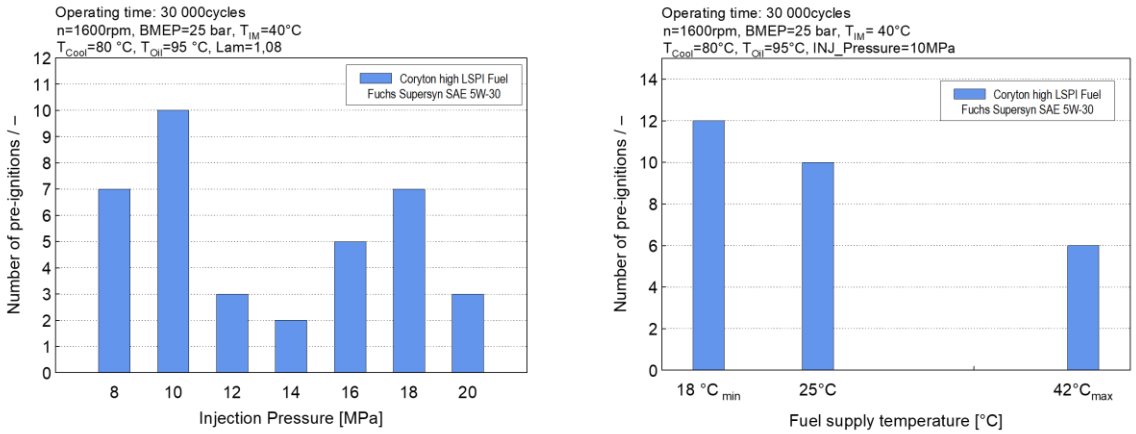

Figure 5-4: Variation injection pressure and fuel supply temperature.

On the testbed in Graz as well as in Karlsruhe, we saw an increase of LSPI events with a higher engine out Lambda values. The engine out lambda shown in Figure 5-5 does not correspond with the combustion chamber lambda. These observations only show the pre-ignition behavior trend, not the number of pre-ignitions matching the combustion lambda. The CFD simulation showed a combustion lambda much lower than the engine out lambda for the investigated operation point. A variation of the start of injection (SOI) showed the highest number of LSPI at an SOI of 250°CA BTDC. Except for SOI 250°CA, the number of pre-ignitions decreases between 220° CA and 300°CA BTDC. Also, on the second test engine in Karlsruhe, the highest number of LSPI events was detected with an SOI of 250°CA BTDC. That leads to the assumption that the mixture formation or liner wall interaction significantly promotes LSPI events with these settings. In another test, we also could show that LSPI's occurrence increases with the engine load. We decided to use 25 bar BMEP for further investigations as a compromise between the number of LSPI that occur and the lowest possible load on the engine. The outliers in some experiments are probably also due to the stochastic occurrence of pre-ignitions. Nevertheless, a trend can be discerned.

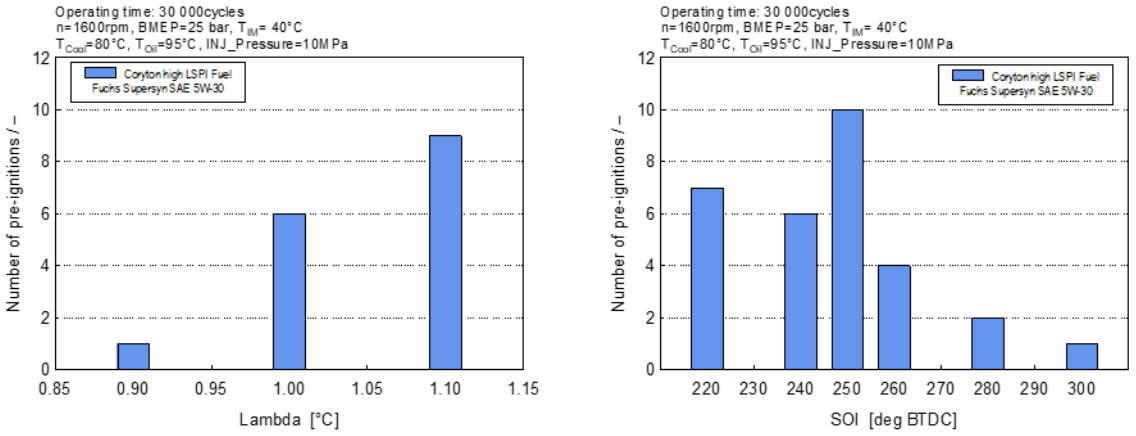

Figure 5-5: Variation Lambda and start of injection.

The suspected mechanism of how pre-ignitions occur in this engine can be explained by an interaction between the injection spray, the spray interaction with the liner wall, and the piston crevice. Nearly all parameter variations that can be assumed to have a worse mixture formation showed an increase in pre-ignitions. A colder cylinder liner wall promotes the condensation of the fuel on the liner wall. This condensation leads to a higher fuel content on the liner wall, which increases the dissolution of fuel in the engine oil. Analytics of the engine oil also showed a high value in oil dilution. Also, a lower fuel entry temperature leads to an imperfect mixture formation. The increasing LSPI events with an increased engine speed can be explained by

the increased charge movement and the promotion of residual building mechanism in the piston crevice. The circumstantial examination of all these variations leads in a first step to the iso-operating point for the optical investigations shown in Table 5-1. Furthermore, there was the first suspicion that pre-ignitions do not occur under these circumstances immediately only after a specific conversion time.

Table 5-1: Iso operating point.

ISO OPERATING POINT	
Engine speed	1600 rpm
Engine torque	200 Nm (25 bar BMEP)
Start of injection	250 °CA BTDC
Ignition	- 4 °CA BTDC
Injection pressure	10 MPa
Exhaust lambda	1.08
Coolant temperature	65 °C
Intake temperature	40 °C
Oil	Fuchs Titan Supersyn F EcoDT 5W-30
Fuel	LSPI Fuel

5.1.2 Injection tests

The injection tests were used to investigate the LSPI behavior of different lubricants. We had to determine how much injected oil leads to pre-ignitions in general. Therefore the oil amount was increased from 0.15 g/kWh to 0.9 g/kWh in three test sequences. For these investigations, an operating point was chosen, which showed no LSPI events with deactivated oil dosing system. Before the test runs, a conditioning sequence without oil dosing has been carried out for 30 minutes. During this conditioning, no LSPI events occurred, which assumes that the injected oil influences the LSPI occurrence. An injected oil amount of 0.15 g/kWh showed no pre-ignitions. With an injected oil amount of 0.45 g/kWh, pre-ignitions occurred shown in Figure 5-6. This test showed a critical oil amount between 0.15 g/kWh and 0.45 g/kWh, leading to pre-ignitions for this operating point. With a higher oil amount also injected, the number of LSPI events increased, shown in Figure 5-6 for 0.9 g/kWh. For further investigation, we chose an oil amount of 0,45 g/kwh to compare the different lubricants.

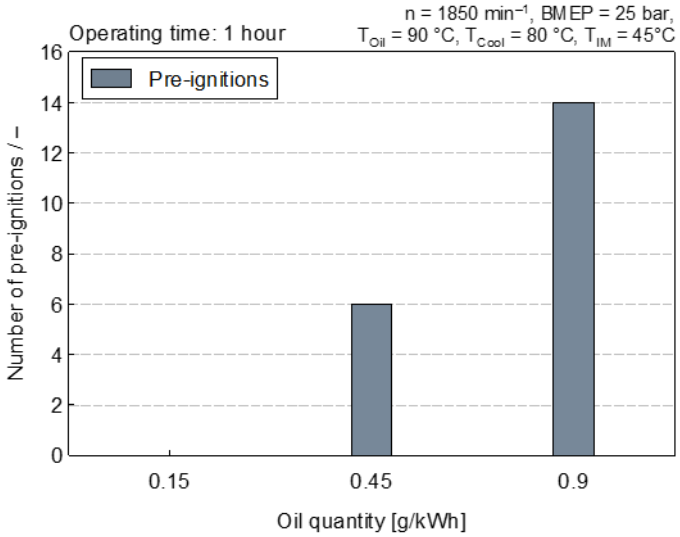

Figure 5-6: Variation of injected oil amount.

During these investigations, different oils have been injected into the intake runner of cylinder three. The used base oil and the reference oil Fuchs 5W-30 have been compared to provided ionic liquids from Iolitec. To verify the methodology, we also injected coolant and regular water. During this investigation, no advantage of Ionic liquids compared to standard oil could be observed, shown in Figure 5-7. Also, the provided base oil showed no benefit regarding LSPI behavior during the injection tests. The route course of pre-ignitions during the injection tests leads to the assumption that LSPI events always occur after an accumulation time as a single event or an LSPI series, shown in Figure 5-8. This behavior, in turn, supports the thesis that accumulated residuals of oil, fuel and soot are working as triggers of pre-ignitions. Due to the long time until the first pre-ignition occurs after the activation of the dosing system, ignition of the oil drop is rather unlikely. Also, the route course of pre-ignitions of other liquids like base oil or ionic liquids showed similar results. In summary, it can be confirmed that ionic liquids showed no advantages to avoid pre-ignitions at this operation point, which is also due to their similar chemical composition to engine oil.

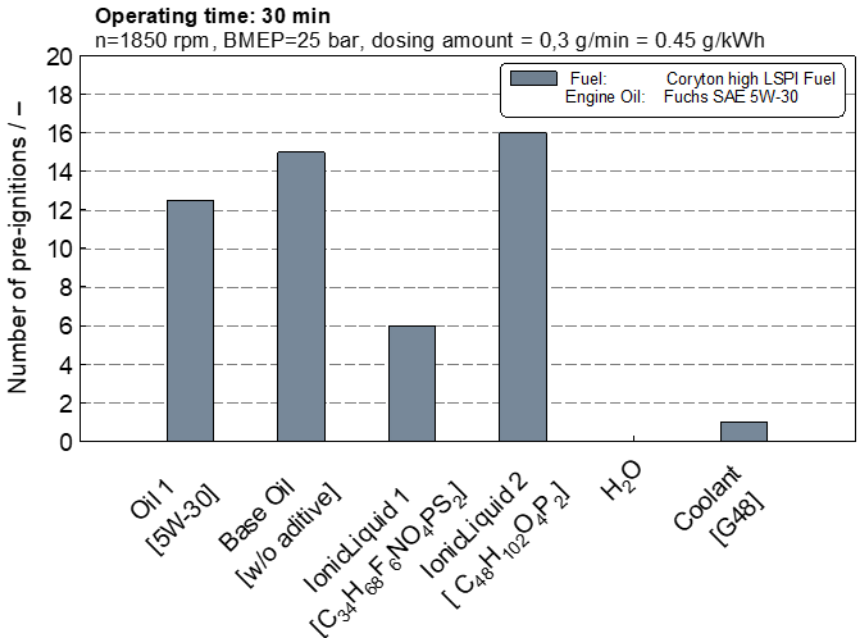

Figure 5-7:Injection tests with different lubricants.

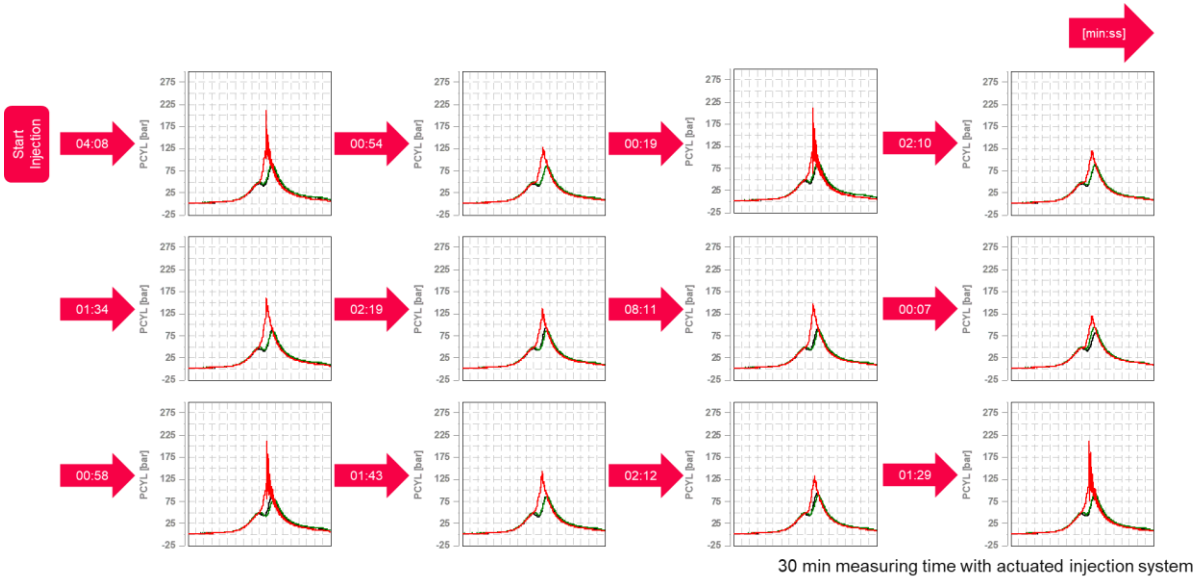

Figure 5-8: Route course LSPI events during dosing of Fuchs 5W-30.

5.1.3 Oil consumption measurements

The oil consumption tests were divided into three independent test methodologies. As explained in chapter 3.2.4, the oil contained in the blow-by gas was measured through filtration and weighing. For these measurements, the results are shown in Figure 5-9. The oil quantity contained in the blow-by gas depends on the blow by mass flow. The transported oil quantity at 1600rpm and 25 bar BMEP was measured with 1.58 g/h results in an oil consumption of 0.04 g/kWh. Compared to the oil dosing tests, the blow-by gas's oil content can only lead to pre-ignitions over an extended accumulation in the intake system.

The turbocharger oil consumption shown in Figure 5-10 for different operation points depends on many boundary conditions like pressure conditions between the crankcase and the turbocharger lubrication system or the turbocharger rotation speed. Nevertheless, a trend of higher oil consumption of this turbocharger at lower load points could be seen. This behavior can be explained through the low-pressure conditions in the intake system at these operation points.

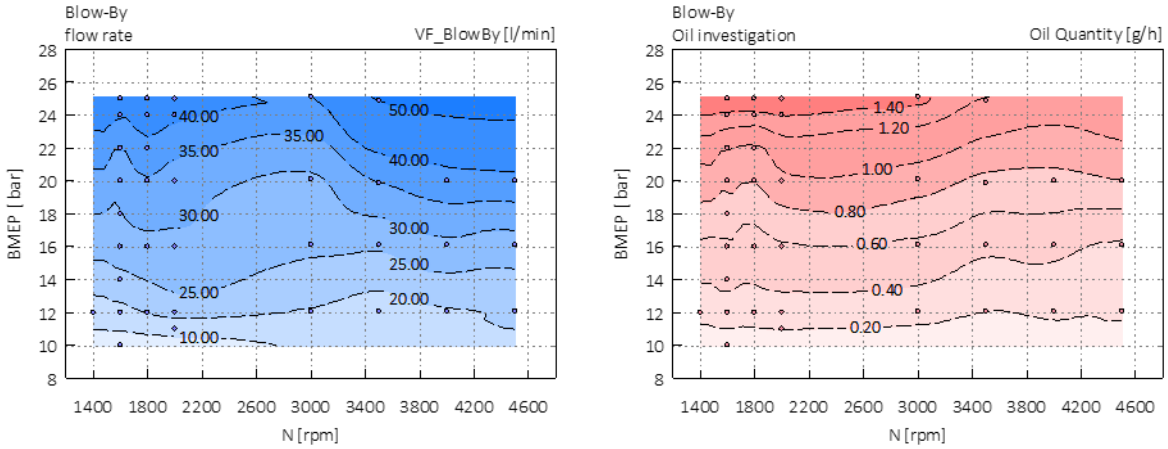

Figure 5-9: Blow-by mass flow and oil quantity of the blow-by gas.

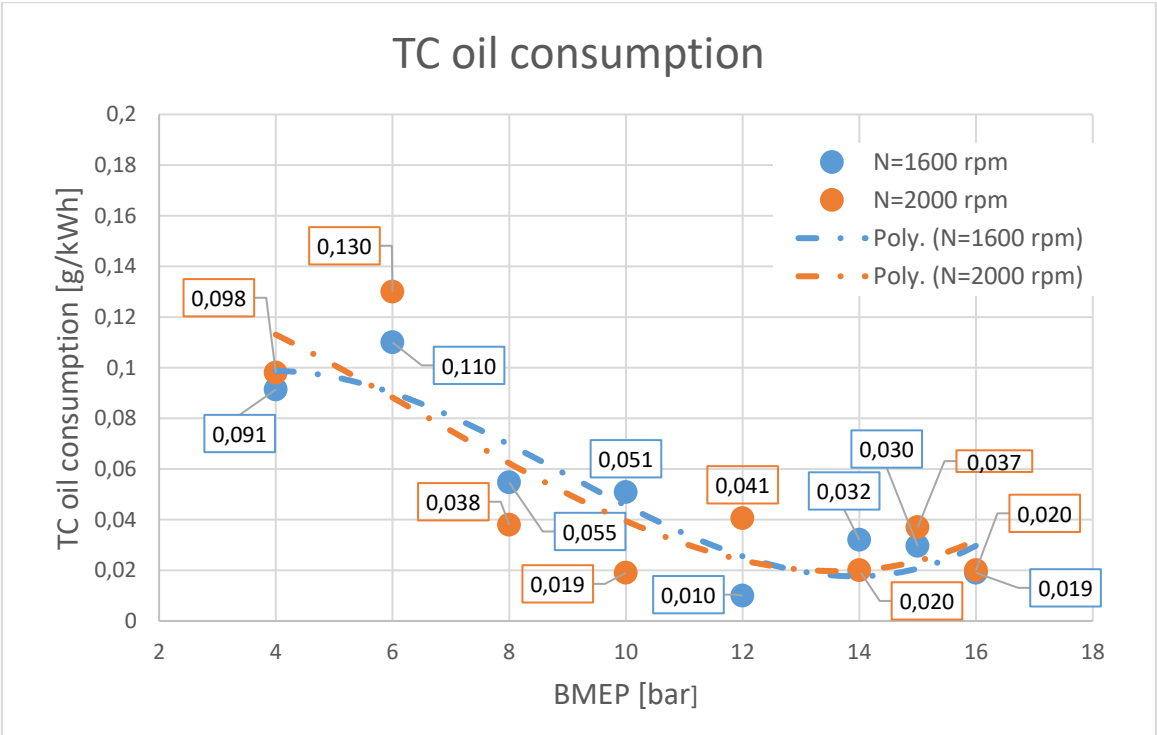

Figure 5-10: Turbocharger oil consumption in g/kWh for 1600 rpm and 2000 rpm.

The low-pressure conditions are promoting the oil transport through the sealings into the intake system. The slightly increasing oil consumption at higher loads is caused by the increased rotation speed of the turbocharger.

The overall oil consumption of the engine measured with the deuterium tracer method is shown in Figure 5-11.

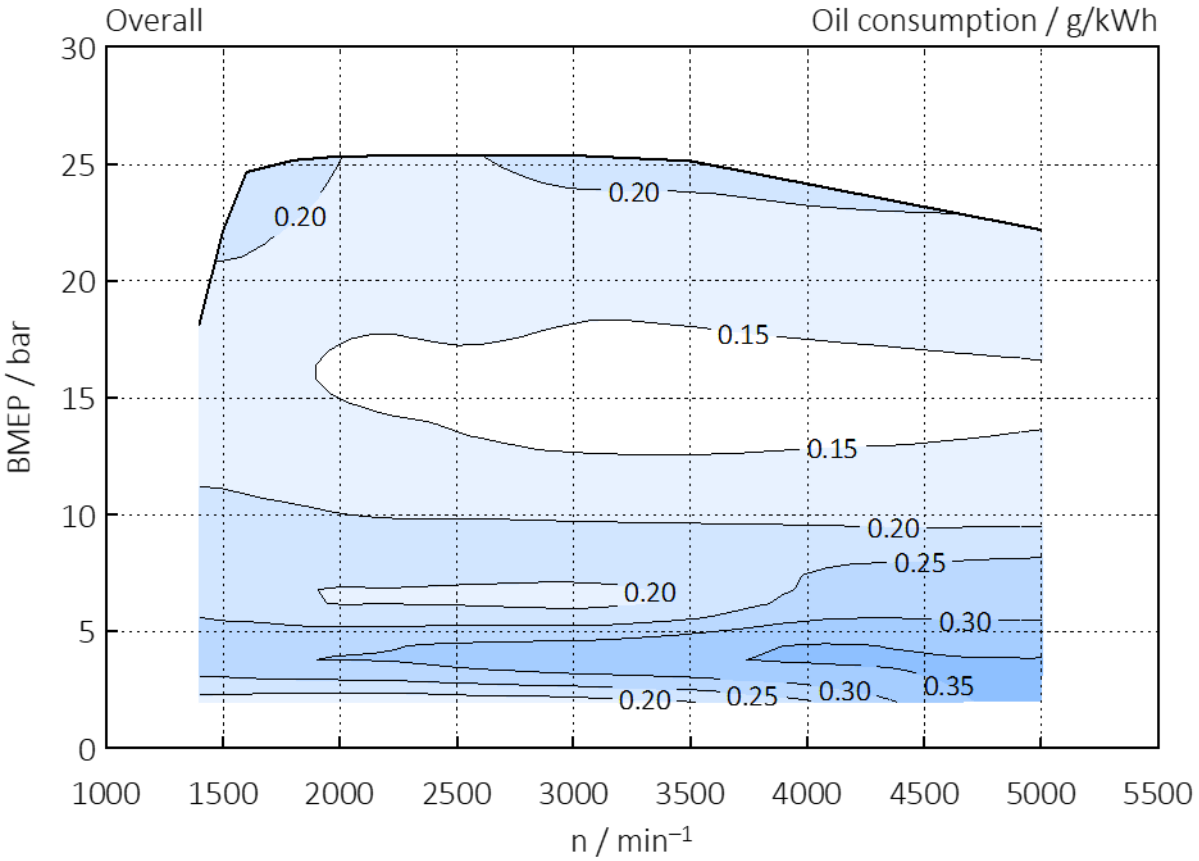

Figure 5-11: Overall oil consumption [g/kWh].

With these oil consumption measurements, the overall oil consumption was divided into their origins. The calculations in Figure 5-12 shows that the majority of the oil consumption is caused in the cylinder. The blow-by oil content rises at higher engine loads caused by the increased blow-by mass flow. Also, the turbocharger oil consumption share increases with the engine load caused by the turbocharger rotation speed.

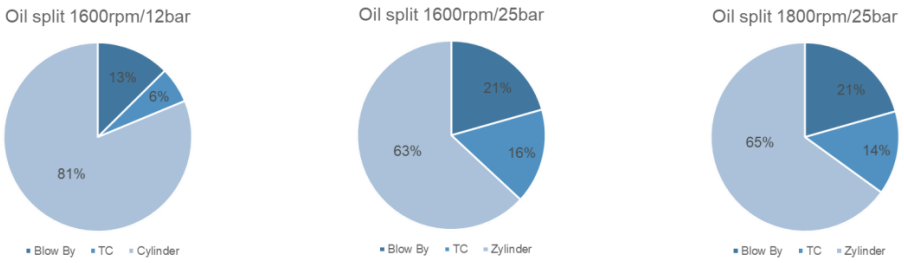

Figure 5-12: Oil split.

5.1.4 CNG investigations

The idea behind the CNG investigations was to exclude the interaction between the injection spray and the liner. The experiments with CNG as fuel confirmed the assumptions about the necessary attendance of residuals in the combustion chamber to gain pre-ignitions

The investigations with CNG as fuel were not performed at the operation point of the parameter variations. We had to increase the engine speed for the CNG investigations compared to the ISO operating point from 1600 rpm to 2200 rpm to reach the target torque of 200 Nm.

In the base investigation point, during five test repetitions, no pre-ignition occurred. To demonstrate the influence of oil in the combustion chamber, we also set up the injection method for the CNG investigations. We were able to measure pre-ignition only with an oil quantity of 2 g/min. All other investigations showed no combustion anomalies. The same operating point investigated with gasoline as fuel showed pre-ignitions without oil dosing into the intake manifold, Figure 5-13. The soot measurements during these investigations, in Figure 5-14, confirmed the assumption regarding the attendance of residuals for LSPI events.

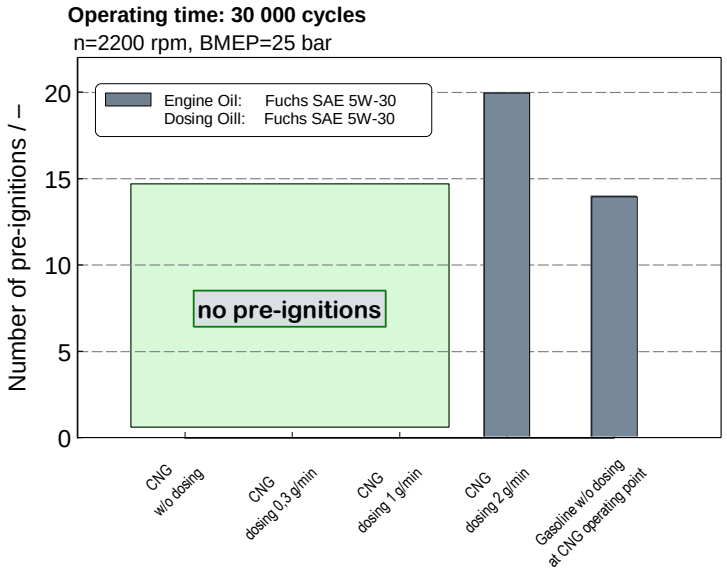

Figure 5-13: CNG investigations.

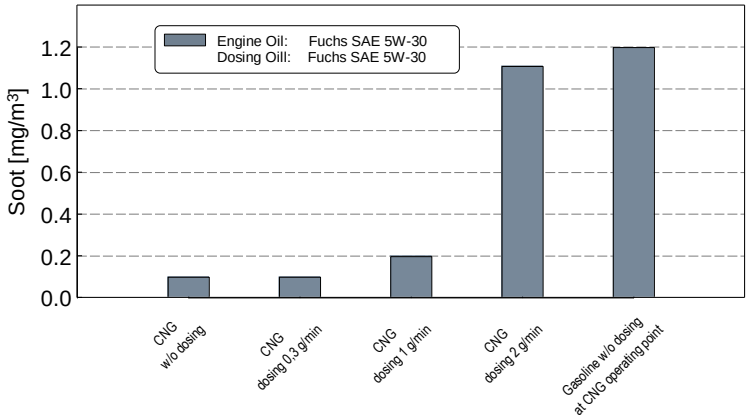

Figure 5-14: Soot value at different CNG and gasoline operating points.

5.1.5 Hardware Variation

The variation of the cylinder liner honing showed higher oil consumption in some parts of the grid than the standard cylinder honing. Also, the comparison of LSPI events at the ISO operating point showed a higher number of pre-ignitions. This could be caused by the increased oil entry into the combustion chamber due to the increased roughness of cylinder honing.

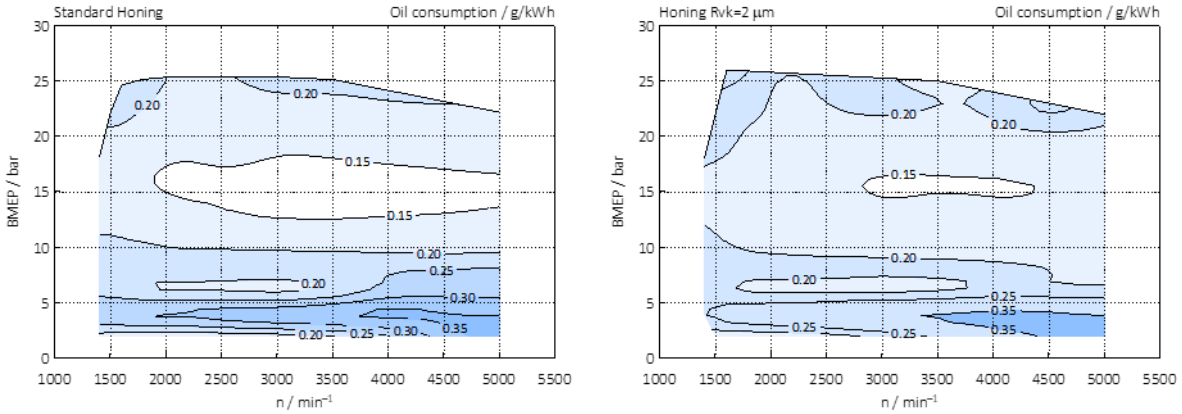

Figure 5-15: Oil consumption standard honing (left), honing Rvk=2 µm (right).

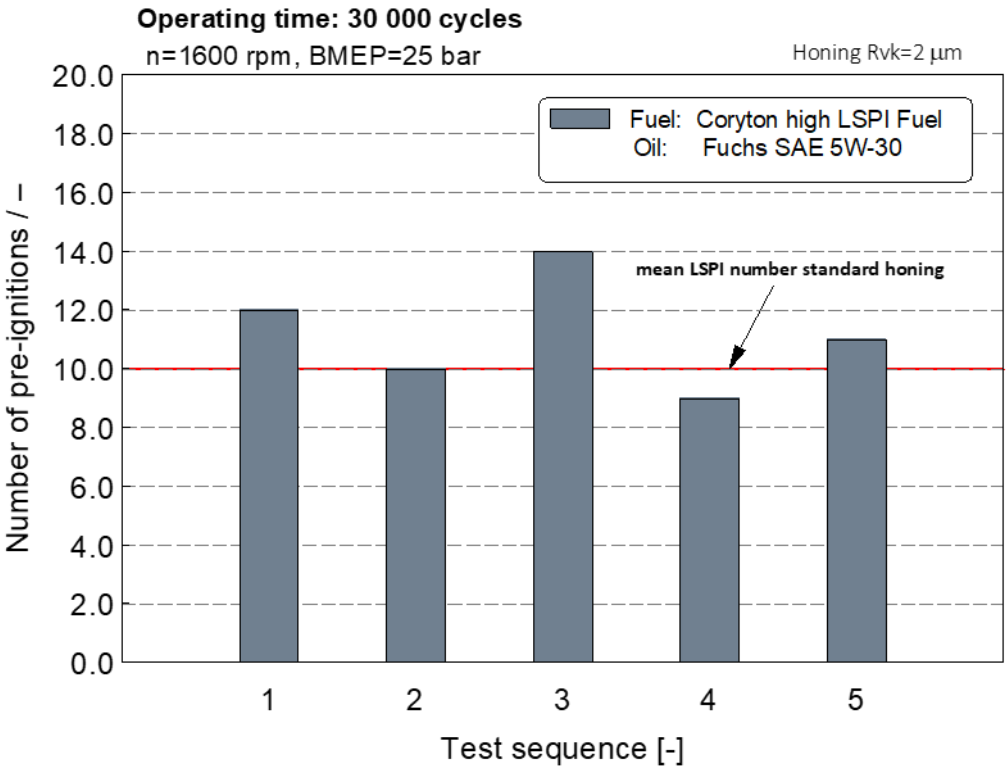

Figure 5-16: LSPI tests with changed honing.

5.2 IFKM results

In this chapter, all relevant results for the mechanism synthesis along the described methodology are presented and discussed in the context of pre-ignition influencing processes. In the end, a synthesized pre-ignition mechanism is presented.

5.2.1 Ex-situ LIF investigations

In order to enable detection of fuel and oil movements in the combustion chamber, a LIF setup (lighting source, tracer and filters) for the optical engine system was determined by means of ex-situ LIF investigations. By using the examination system shown in Figure 5-17, defined compositions of fluorescent dye and liquid can be spectrally examined under different temperature boundary conditions.

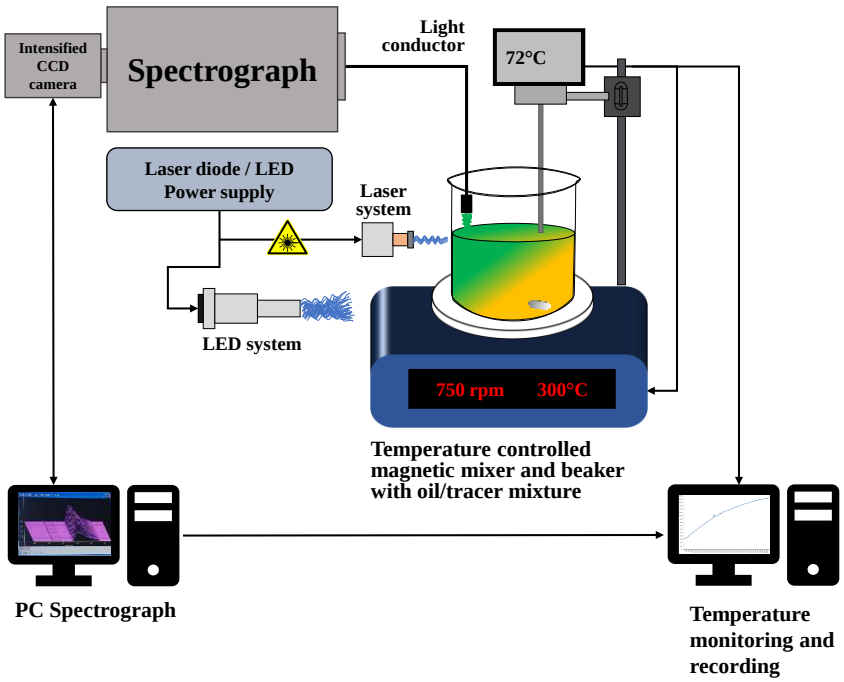

Figure 5-17: Fluorescence investigation system.

The light from an excitation source is introduced at the side of the beaker just below the liquid surface at a short distance. The light spectrum of the engine lighting system is used for this purpose. By means of a magnetic stirrer with integrated temperature control, the liquid/ tracer mixture can be tempered and stirred in a defined manner. A fiber optic bundle (190-1100 nm) is used as a light guide for recording and introducing the fluorescent light to the spectrograph. The light guide is held at right angles to the excitation light source in the beaker at a small distance above the liquid. An Acton SP2556 from Princeton Instruments (focal length of 500 mm) with a 200 µm entrance slit is used in combination with Princeton Instruments PI-MAX image intensified CCD camera to record the spectrum. For sample preparation, fresh oil and fuel were each weighed to 200 ml and enriched with tracer quantities in Duran beakers. The tracer amounts were prepared using a high-precision scale (Sartorius ENTRIS224-1S). For mixing, the fuel/ tracer mixtures were each stirred for 5 min using a magnetic stirrer at 1500 rpm. The oil/ tracer mixtures were additionally dissolved at 60°C for 20 min in an ultrasonic bath.

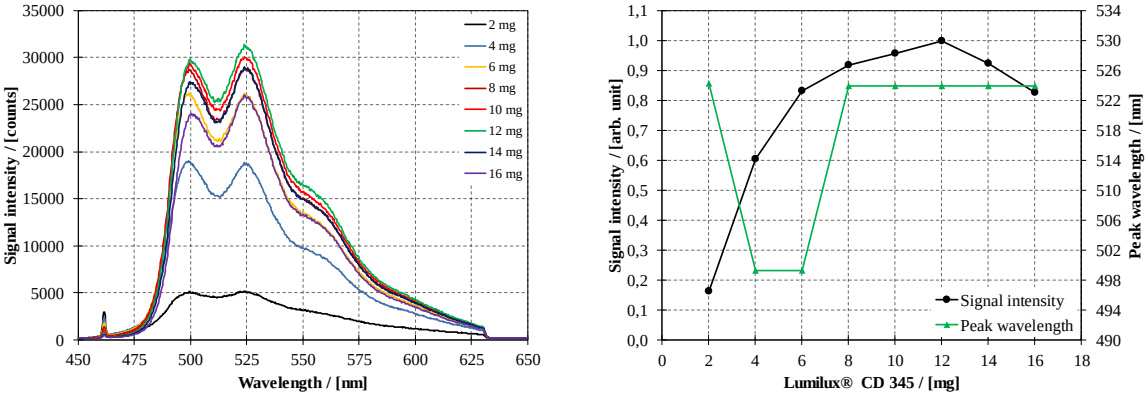

Figure 5-18: Emission spectra of Lumilux® CD 345 in Fuchs 5W20 (30°C) with different tracer concentrations (left); Normalized signal intensity and peak wavelength as a function of the Lumilux® CD 345 concentration in Fuchs 5W20 (right).

Figure 5-18 shows the emission spectra of Honeywell Lumilux® CD 345 in Fuchs 5W20 (30° C) at different tracer concentrations as well as the associated standardized signal intensity and peak wavelength as a function of the concentration when excited by means of a laser diode. In the area around 462 nm, the temperature-shifted excitation spectrum of the laser diode can be seen again. The spectrum is characterized by a double peak (499 and 524 nm) and is strongly dependent on the concentration. A signal intensity difference between the peaks that increases relative to the concentration can only be observed weakly. The second peak becomes more dominant as the concentration increases. The concentrations 4 and 6 mg show a slightly dominant first peak, which is why there is a peak wavelength shift here. The concentration-dependent fluorescence intensity shows a maximum in the range of around 12 mg Lumilux® CD 345. After that, quenching effects will probably occur more intensely.

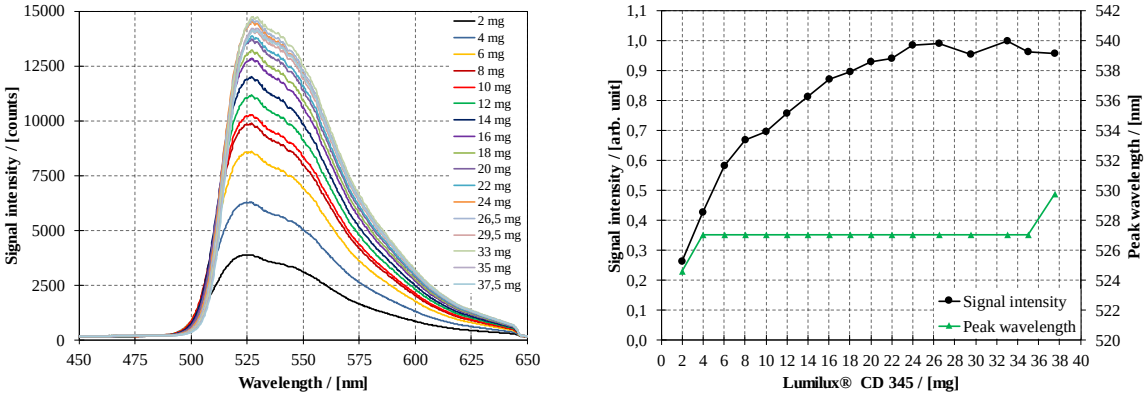

Figure 5-19: Emission spectra of Lumilux® CD 345 in Coryton "High LSPI" (17°C) with different tracer concentrations (left); Normalized signal intensity and peak wavelength as a function of the Lumilux® CD 345 concentration in Coryton "High LSPI" (right)).

Figure 5-19 shows the emission spectra of Lumilux® CD 345 in Coryton "High LSPI" fuel (17° C) at different tracer concentrations as well as the associated standardized signal intensity and peak wavelength as a function of the concentration when excited by LED LE D P3MQ with a 500nm SPF. In contrast to the oil, the spectrum is characterized by a single peak at 527 nm but is also strongly dependent on the concentration. The concentration-dependent fluorescence intensity shows a maximum in the range between 26 and 33 mg Lumilux® CD 345. After that, the quenching effects increase again. In a direct comparison to engine oil, there is significantly better solubility and a greater tracer concentration potential.

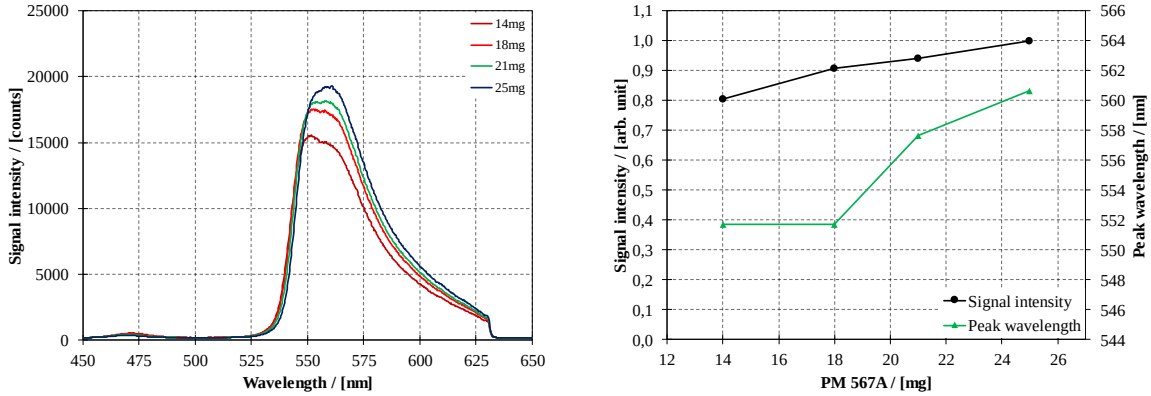

Figure 5-20: Emission spectra of PM567A in Fuchs 5W30 (30°C) with different tracer concentrations (left); Normalized signal intensity and peak wavelength as a function of the PM567A concentration in Fuchs 5W30 (right).

Figure 5-21 shows the emission spectra of PM567A in Fuchs 5W30 (30° C) at different tracer concentrations and the associated standardized signal intensity and peak wavelength as a function of the concentration, when excited by means of the LED LE B P3W 01 with 500 nm SPF. The excitation spectrum of the LED can be observed weakly in the range around 468 nm. The spectrum shows an increasing redshift with increasing concentration. Up to 25 mg PM567A, a flat increase in intensity is visible, which indicates that the maximum concentration potential will soon be reached.

In the ex-situ investigations, two possible tracers (Lumilux® CD 345 and PM567A) and their specific ideal concentrations in fuel and oil were defined when excited by light in the spectral range of the engine lighting system (450-480 nm). The final filter selection was defined in a downstream fluorescence detection analysis in a “combustion chamber replica” under engine LIF setup conditions (Figure 5-21). The lighting system is spectrally cut off using a short-pass filter (spectrum of the LED) in order to enable fluorescence detection to be clearly spectrally separated via a long-pass filter. This also showed the advantage of an LED system compared to a laser beam expanded lighting system with regard to homogeneous combustion chamber illumination.

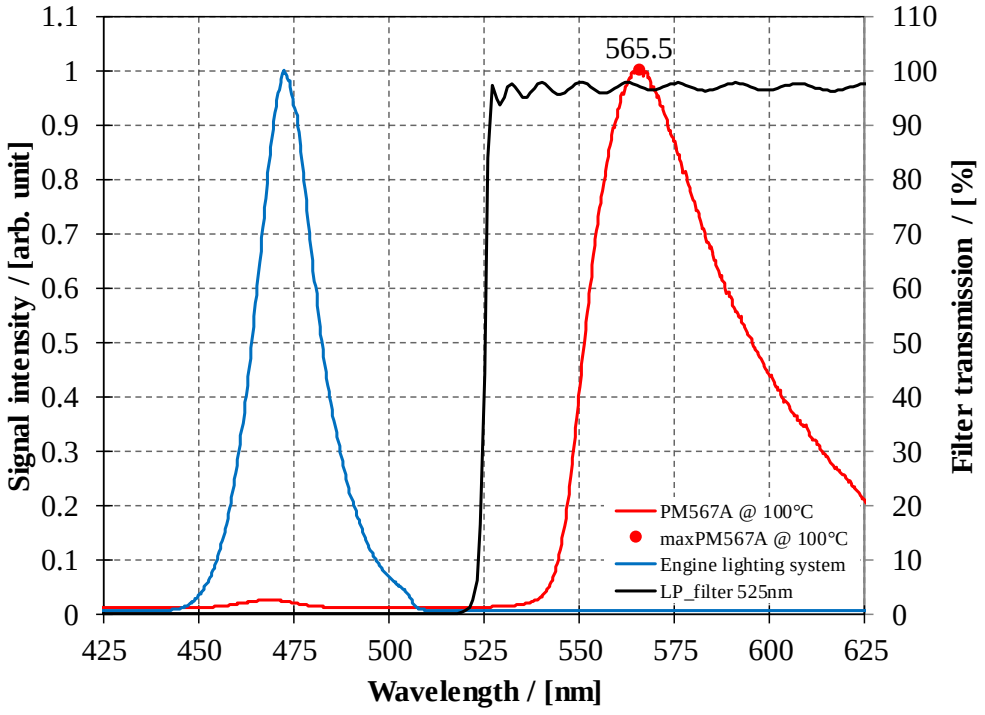

Figure 5-21: Exemplary spectral oil LIF engine setup.

For further characterization of LIF properties beyond the information required for the investigations described here, please refer to the planned paper "Investigations to characterize the interactions of light radiation, engine oil/ fuel and fluorescence tracers for the use of qualitative light-induced fluorescence in engine systems".

5.2.2 Macroscopic PI characterization: Generation of pre-ignitions

The general focus of all macroscopic pre-ignition characterizations shown here is not to build a comprehensive statistics-driven pre-ignition evaluation but rather to specifically confirm the current state of knowledge for the engine system at hand and to provide an investigation basis for the further optical pre-ignition characterizations through an iterative pre-ignition maximization path. This approach is justified in part by the limited possibility of mechanism synthesis based on "macroscopic statistics-driven pre-ignition results" as well as the general statistics challenge of valid pressure-based pre-ignition detection. The optical examinations showed many "mild" pre-ignition whose detection by means of a pressure signal and the corresponding detection criteria was not clearly ascertainable.

In order to generate a sufficiently high pre-ignition level as a basis for the optical pre-ignition characterization, a short series of tests based on 7x15k cycles was carried out on the pre-ignition influence of different engine operating media. The results are shown in Figure 5-22.

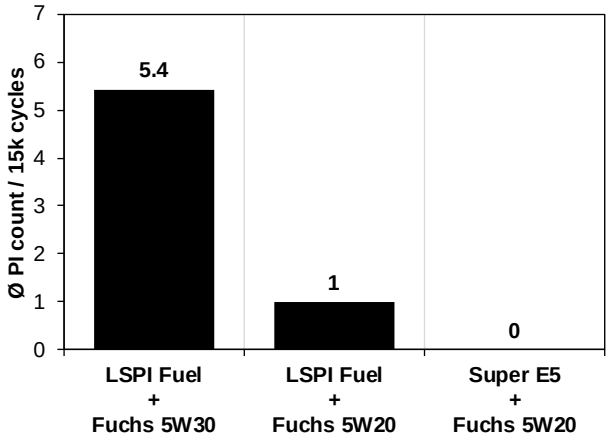

Speed	= 1600 rpm
T	= 200 Nm
IGN	= -4 °BTDC
λ	= 1.08
RP	= 13.8 MPa
SOI	= 280 °BTDC
T_{Air_in}	= 40 °C
T_{CW_out}	= 80 °C

Figure 5-22: Pre-ignition characteristics of different engine operating media combinations.

During engine operation with Fuchs 5W20 oil and IFKM Super E5 fuel, no pre-ignition occurred at the load point shown. The change of fuel led to a low level of pre-ignition, which experience has shown can be explained by the increasing proportion of high-boiling components in the fuel and the associated increased spray/ liner interaction [18]. Still, this level is insufficient for optical investigations.

Only the change to Fuchs 5W30 engine oil led to a significant increase in the level of pre-ignition. Here, a disproportionate oil influence on the pre-ignition probability is already visible, which speaks in favor of a strong involvement of the engine oil in the mechanism for pre-ignition. A direct comparison of the oils, in particular considering the additive components and assuming a strong calcium contribution to the pre-ignition formation, hints towards the nonlinear behavior already observed in [52]., which is also not uncommon in chemical kinetics in general. For further in-depth characterization, the combination of High LSPI fuel and Fuchs 5W30 oil was used.

5.2.3 Macroscopic PI characterization: PI critical engine operating conditions

The low pre-ignition level of the Fuchs 5W20 oil could also be confirmed in the test cycle for iterative determination of pre-ignition-critical engine parameter setups (Figure 5-23).

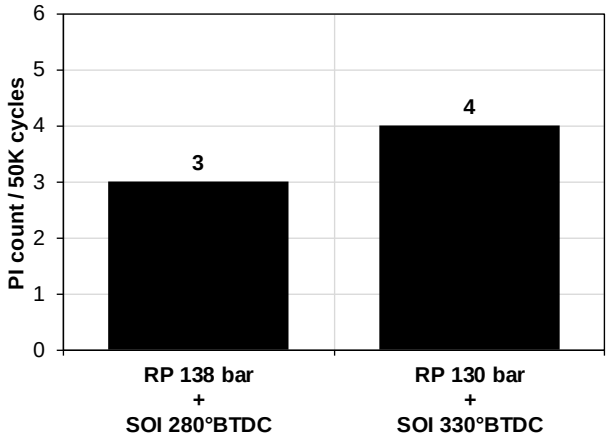

Speed	= 1600 rpm
T	= 200 Nm
IGN	= -4 °BTDC
λ	= 1.08
T_{Air_in}	= 40 °C
T_{CW_out}	= 80 °C
Oil	= 5W20
Fuel	= LSPI Fuel

Figure 5-23: Pre-ignition level: Fuchs 5W20 + Coryton LSPI Fuel.

Figure 5-24 shows a significant influence of the air-fuel ratio on the pre-ignition number. The lambda values are measured downstream of the turbocharger, but their delta also corresponds to in-cylinder lambda changes at a constant valve overlap.

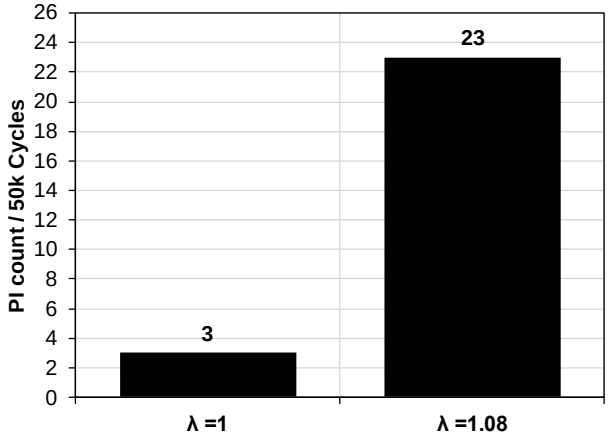

Speed	= 1600 rpm
T	= 200 Nm
IGN	= -4 °BTDC
RP	= 15 MPa
SOI	= 260 °BTDC
T_{Air_in}	= 40 °C
T_{CW_out}	= 65 °C
Oil	= 5W30
Fuel	= LSPI Fuel

Figure 5-24: Influence of air-fuel ratio on pre-ignition number.

A pure temperature reduction effect does not seem to be decisive here [53] [54]. [54] presents a hypothesis, which assumes that particle oxidation as a pre-ignition triggering preparing process is reduced by the increased residual gas content (lower lambda value) in the cycle before the pre-ignition between the expansion to exhaust stroke. This is based on a deposit flake-driven pre-ignition mechanism.

Figure 5-25 shows the already widely observed [55] [56] pre-ignition influence of the cooling water temperature. As the cooling water temperature decreases, the probability of pre-ignition increases. Here, the increasing spray/ liner interaction (lower fuel temperatures) and the associated detachment of oil-containing droplets are regarded as the main mechanism of action.

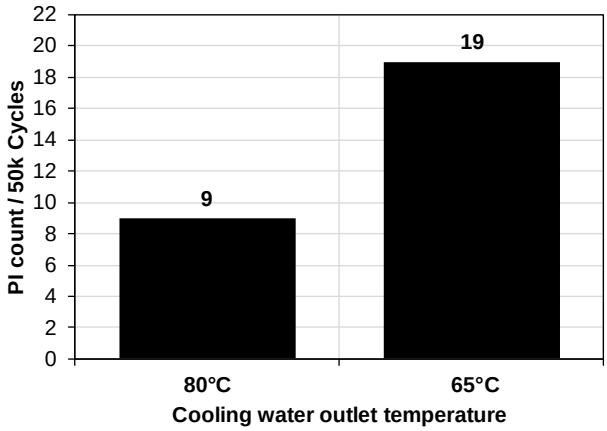

Speed	= 1600 rpm
T	= 200 Nm
IGN	= -4 °BTDC
λ	= 1.08
RP	= 13.8 MPa
SOI	= 280 °BTDC
T_{Air_in}	= 40 °C
Oil	= 5W30
Fuel	= LSPI Fuel

Figure 5-25: Influence of cooling water temperature on pre-ignition number.

For further iterative pre-ignition maximization, the following parameter variations were always carried out on the basis of the "bad engine setups" found. Figure 5-26 shows the influence of the start of injection. There is a tendency to show a clear increase in pre-ignition with late injection timings. This was also observed in [56]. Again, a strongly increasing spray/ liner interaction is seen as a dominant pre-ignition driver.

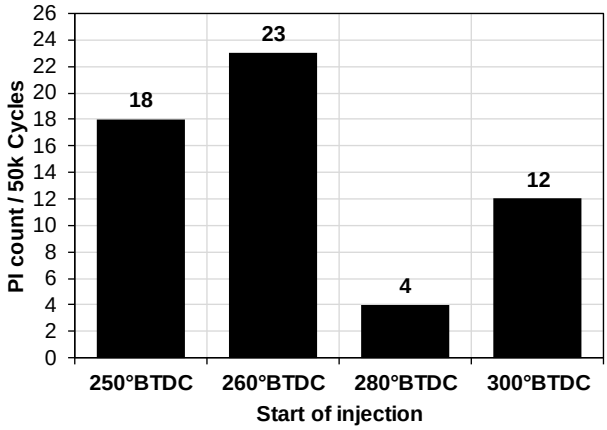

Speed	= 1600 rpm
T	= 200 Nm
IGN	= -4 °BTDC
λ	= 1.08
RP	= 15 MPa
T_{CW_out}	= 65 °C
T_{Air_in}	= 40 °C
Oil	= 5W30
Fuel	= LSPI Fuel

Figure 5-26: Influence of the start of injection on pre-ignition number.

Figure 5-27 shows a variation of the injection pressure. For the injection pressures of 80 and 100 bar, only 20k cycles were run due to the high incidence of pre-ignition. Here, the CFD simulations showed a great fuel spray penetration into the combustion chamber and thus also the possibility for high spray/ liner interaction.

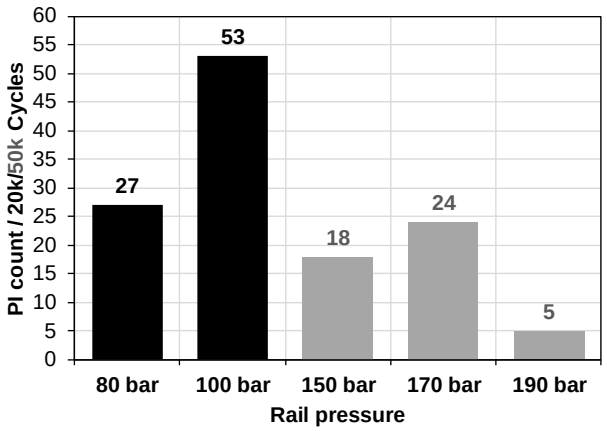

Speed	= 1600 rpm
T	= 200 Nm
IGN	= -4 °BTDC
λ	= 1.08
SOI	= 250 °BTDC
T_{CW_out}	= 65 °C
T_{Air_in}	= 40 °C
Oil	= 5W30
Fuel	= LSPI Fuel

Figure 5-27: Influence of injection pressure on the pre-ignition number.

In the iteration process of the macroscopic pre-ignition characterization, an increase in the spray/ liner interaction emerges as the dominant driver for pre-ignition. An engine parameter setup with an extremely high pre-ignition level was found: 100 bar point from Figure 5-27. We refer to this load point as "ISO load point". Thereby a basis for the subsequent optical characterizations has been provided. The results are very congruent to the thermodynamic LSPI characterizations from IVT.

5.2.3.1 Distinctive pre-ignition behavior

In the total overview of all generated pre-ignitions, the individual cylinder distribution is shown in Figure 5-28. The pre-ignition occurrence appears to be relatively evenly distributed. The interpretation of marginal cylinder differences is not permissible due to the statistically relatively small data basis. Another phenomenon is shown in Figure 5-28 on the right: If we look at the occurrence of pre-ignition in all 3x150k cycles, we notice a clear reduction in the frequency of pre-ignition in the second 50k cycle, which also remains at a comparatively low level in the third cycle. A continuously increasing oil dilution can be observed over the driving time. However, this cannot be linearly correlated due to the constant behavior of the 100k and 150k cycles. Also, the averaging over different engine parameter setups of the different test cycles makes an interpretation difficult. Quickly occurring oil changes could form an explanatory model here. This illustrates the relevance of oil changes for comparability.

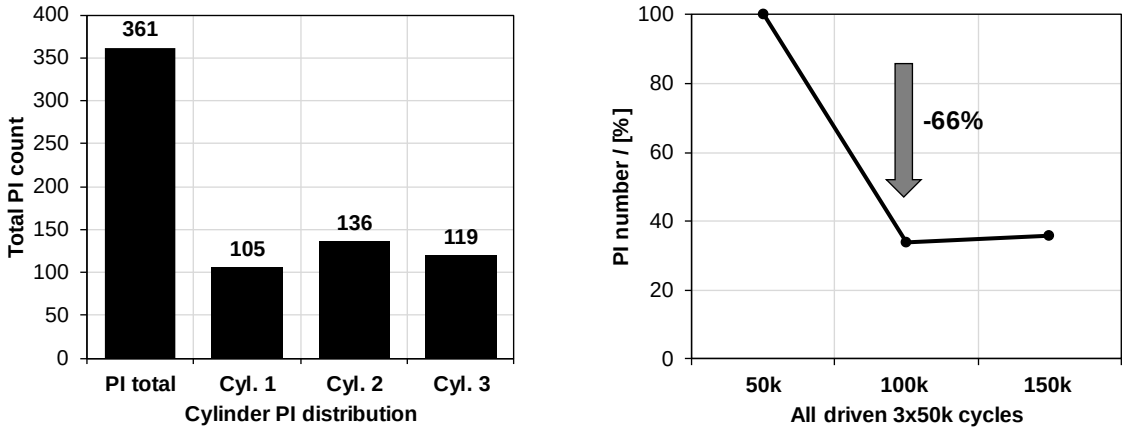

Figure 5-28: Cylinder pre-ignition distribution of all measured pre-ignitions (left) and pre-ignition level behavior depending on completed test cycles (right).

A consideration of pre-ignition occurrence over time within a 20/50k series of measurements is shown in Figure 5-29. These are the three test cycles with the largest number of detected pre-ignitions. The pre-ignition count per 2.5k engine cycles based on the total number of pre-ignitions of a test cycle is plotted. A phenomenon similar to Figure 5-28 on the right can also be observed with constant engine parameter setup within one 50k cycle. The number of pre-ignitions per 2.5k cycle unit decreases as the cycle time progresses (increasing oil dilution) and seems to settle at a certain level. In addition, there is a kind of "wave-like" behavior. This speaks for a multi-cycle pre-ignition mechanism, which has to "build up" until a pre-ignition event (individual pre-ignition or series) occurs. After that, the process seems to repeat itself until the next pre-ignition event occurs. A pre-ignition event is apparently able to set the basic process somehow back to its "initial state".

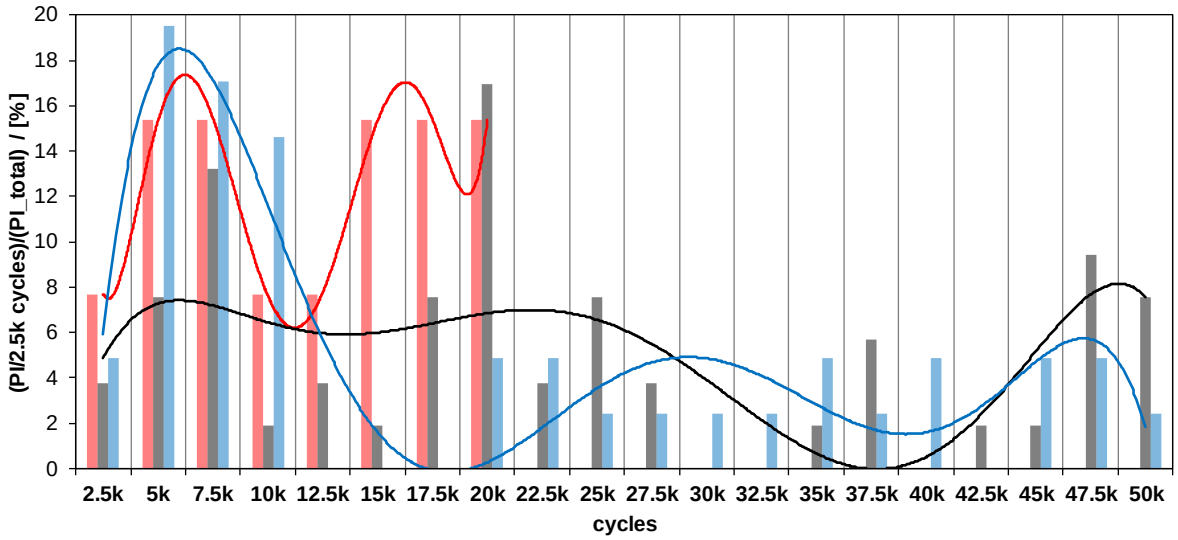

Figure 5-29: Characteristic pre-ignition occurrences within a 20k/50k test cycle.

5.2.4 Optical pre-ignition characterization

The results of the optical pre-ignition characterization are presented below. These are recordings of the "ISO load point" as well as engine parameter setups which showed a lower pre-ignition level in the macroscopic pre-ignition characterization ("cleaner" load points). The general pre-ignition behavior was very congruent. The crank angle resolution of the optical recordings was 2° CA at 1600 rpm due to the selected exposure time. This corresponds to a good compromise between maximum resolution and necessary exposure time.

5.2.4.1 Distinctive pre-ignition behavior

All recorded pre-ignition events showed general, unmistakable behaviors, which are presented in this chapter. The terms “solid particulate matter” and “particle” are used congruently.

Detached / floating particles

During engine operation at preignition-critical load points, freely moving solid particulate matter (particles) of various sizes can be observed in the combustion chamber. The solid property can be attributed to the injection jet impulse transfer without form changing. Figure 5-30 shows a floating particle in the intake stroke of the cycle before pre-ignition and in the cycle after pre-ignition. A comparable occurrence of solid particulate matter could also be observed in [57]. In this event, pre-ignition is initiated by a glowing particle entering the piston crevice. In general, the presence of solid particulate matter can be observed to a small extent in normal cycles. This circumstance suggests that deposits formed at these load points can be detached independent of pre-ignition events and can then remain in the combustion chamber for a certain time.

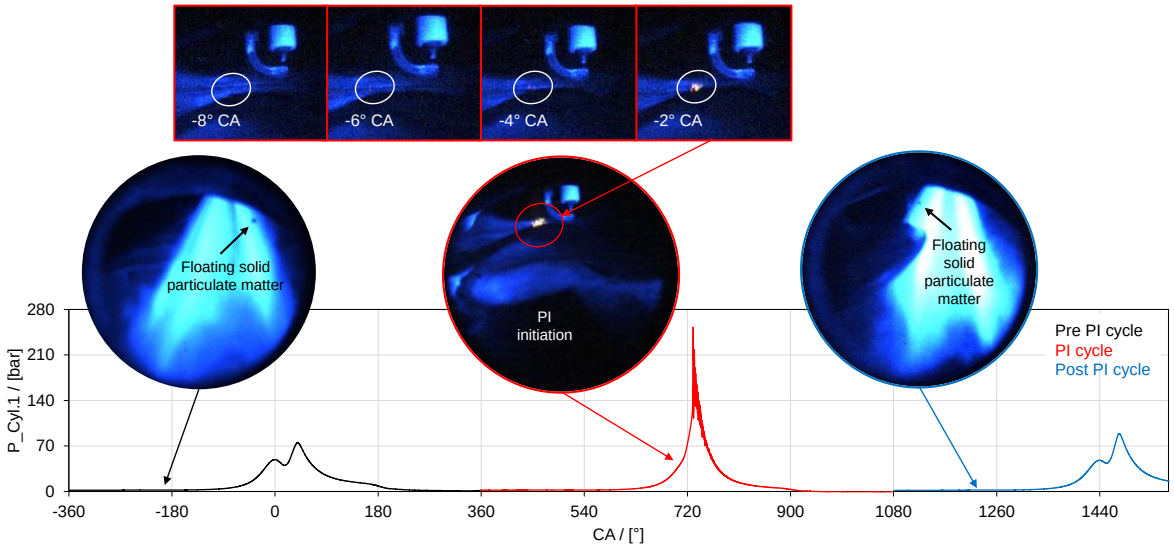

Figure 5-30: Floating solid particulate matter bevor and after pre-ignition event cycles.

Particle / deposit detachment by pre-ignition and follow up (super) knock

Another phenomenon is the combustion chamber "cleaning effect", which can already be observed in knocking combustion and can lead to deposit detachment due to large pressure oscillations and high temperatures [58]. Figure 5-31 shows a comparable behavior due to pre-ignition with subsequent "super knock". The pre-ignition is initiated by a glowing particle near the inlet valves. In the preceding cycle, clear bore top (crevice) deposits and piston deposits are visible. In the exhaust stroke of the following (pre-ignition) cycle, a large amount of dissolved solid particulate matter is visible. The presence of solid particulate matter in the subsequent intake stroke shows that these detached elements can remain in the combustion chamber despite the charge exchange. The subsequent compression stroke shows a bore top (crevice) and piston head free of deposits. This initial pre-ignition-induced deposit detachment mechanism has a large influence on the in-cylinder conditions immediately following pre-ignition events [56].

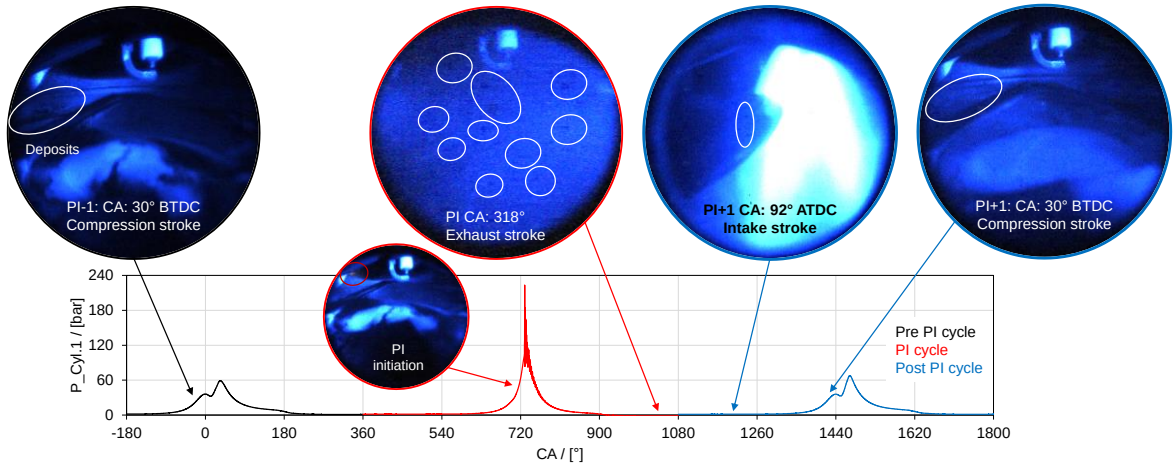

Figure 5-31: Particle / deposit detachment by pre-ignition and follow up (super) knock.

Burning solid particulate matter in a cycle-by-cycle decreasing manner

The effects of such a pre-ignition-initiated detachment mechanism are shown in Figure 5-32. In the cycle after the pre-ignition, a large amount of burning solid particulate matter can be seen after combustion has been initiated by the spark plug. The particle amount decreases with every following cycle until there is no more difference to the cycles prior to pre-ignition.

The solid particle character shows itself in a very special way when such substances bounce off the spark plug ground electrode in the exhaust stroke without changing their shape in a great way. In this time window near the end of the exhaust stroke, some particles go into a glowing state due to the decreasing oxygen availability and the presumably burnt outgassing. There also seems to be a difference in the chemical kinetics of individual solid particulate matter (glowing vs. non-glowing). This leads to the assumption that different material compositions may be involved, which is also confirmed by the increased occurrence of glowing particles near the end of the exhaust stroke under comparable pre-ignition pressure conditions in the oil injection investigations. Compared to [18], pre-ignition series are less frequent, which is probably due to the increased scavenging effect.

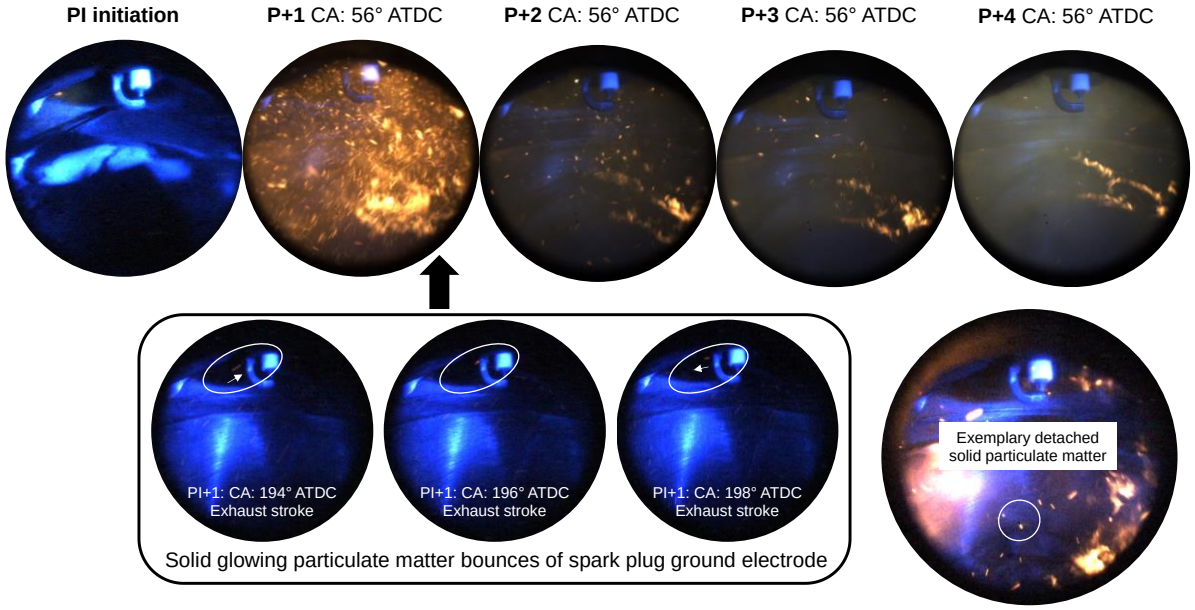

Figure 5-32: Detached solid particulate matter burns/ glows in a cycle-by-cycle decreasing manner.

Pool fire characteristics of different injection strategies

Figure 5-33 shows the typical combustion pattern with a pronounced pool fire point and individual luminescence points during engine operation with pre-ignition-critical parameter setups. Compared to a point with a lower pre-ignition probability, the "ISO load point" shows a more pronounced pool fire, which indicates an increased spray/ liner/ piston interaction. The image of the spray/ liner interaction as a fundamental driver for pre-ignition is condensing. The exact spray and liquid film distributions in the “ISO load point” are clearly shown in the accompanying CFD simulations and also in the later LIF investigations.

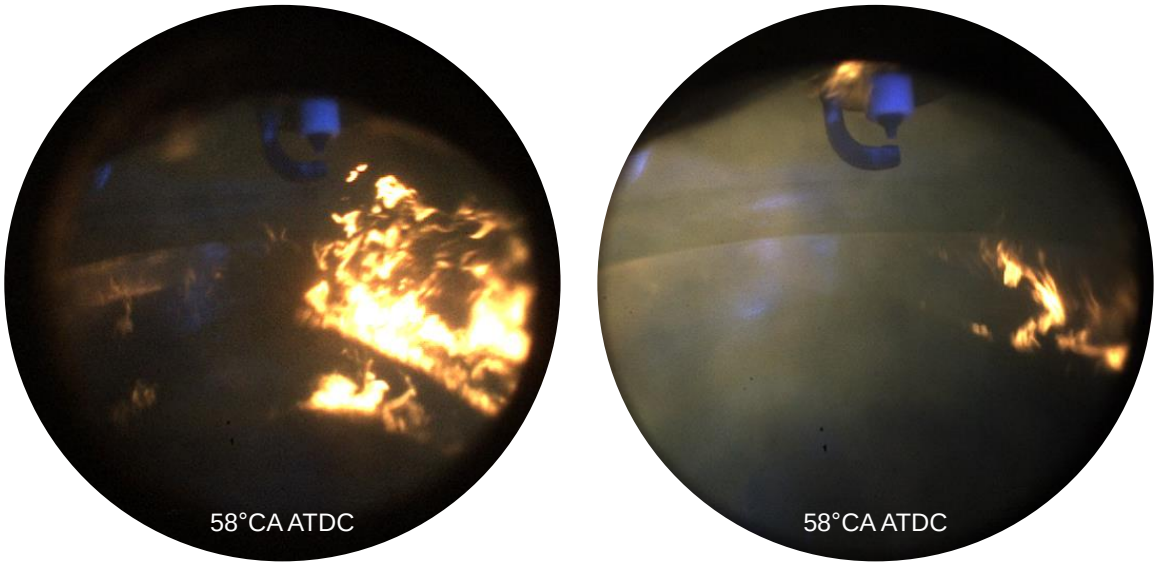

Figure 5-33: Luminous flames on piston top / crevice area at max pre-ignition level load point (left) and “cleaner” load point (right).

Deposit formation at piston crevice / bore top

In the direct comparison of the load points in Figure 5-33, a qualitative deposit build-up difference and thus a spray/ liner interaction correlation can also be visually recognized. Figure 5-34 shows the comparison of the typically resulting deposits in the area of the piston crevice at the bore top after engine operation in pre-ignition load points with different engine parameter set-ups. The "ISO load point" shows an increased build-up of deposits, which speaks for a clear correlation between deposits and pre-ignition frequency.

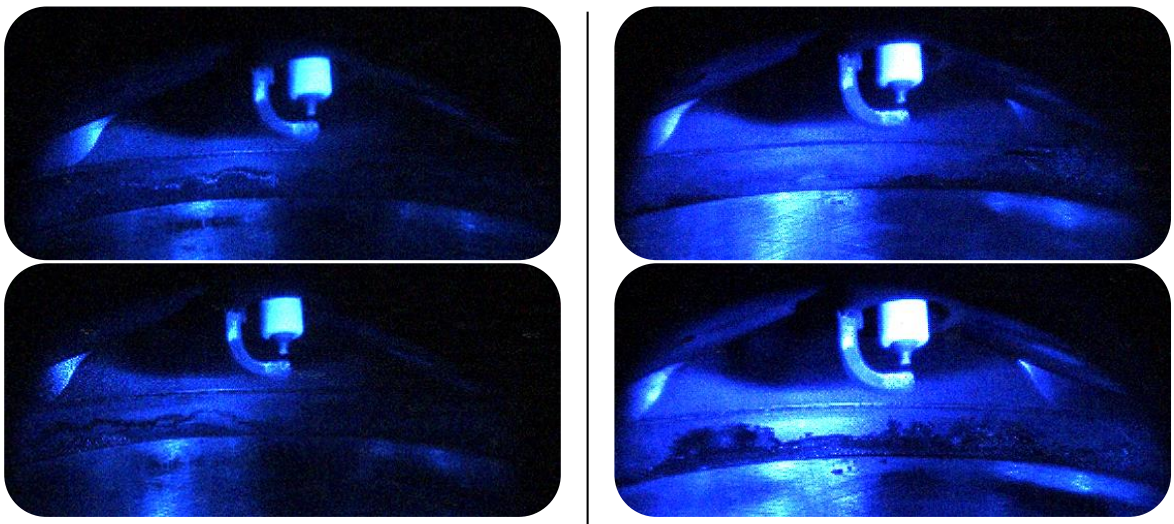

Typical “ISO load point” bore top pictures
→ More and thicker deposits

“Cleaner” load points with reduced PI frequency
→ Reduced deposit build up

Figure 5-34: Formed deposits after pre-ignition load point operations at crevice / bore top.

When looking at the temporal course of the deposit pattern, a very dynamic process is generally noticeable. Figure 5-35 shows the deposition pattern after individual optical pre-ignition runs under "cleaner" engine parameter setups (~10k engine cycles). It is noticeable that deposits build up relatively quickly but also disappear again. The degradation of deposits, mainly driven by pre-ignition events, results in a very dynamic cycle process which is (probably) also reflected in the behavior of Figure 5-29.

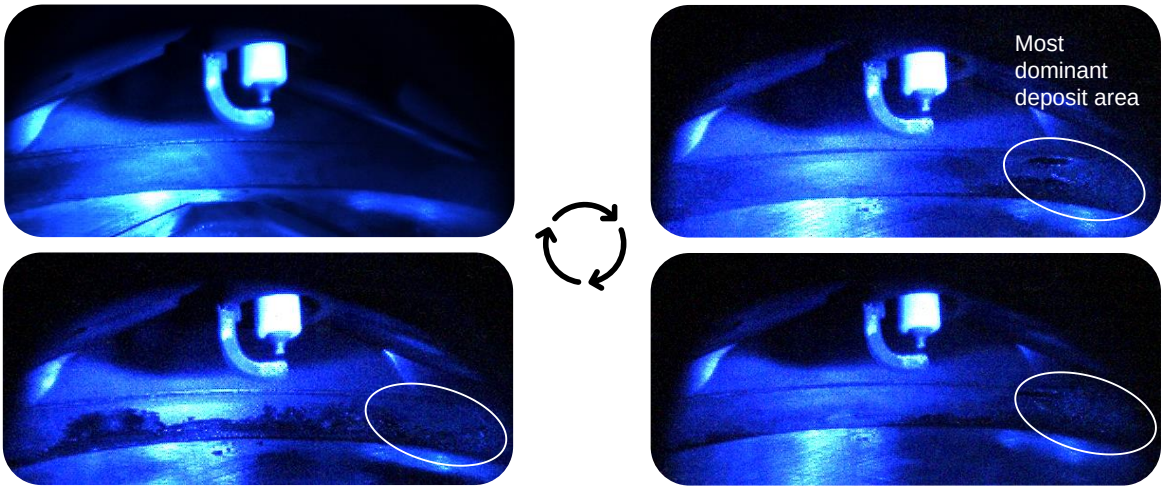

Figure 5-35: Dynamic deposit build-up at pre-ignition load points.

There is increasing evidence of a strong deposit involvement in the pre-ignition mechanism. The most dominant deposit area corresponds to the pool fire areas from Figure 5-33 and thus allows the conclusion that the boundary conditions present here in the form of a locally increased fuel/ oil content under strongly sub-stoichiometric combustion conditions lead to increased deposits.

5.2.4.2 Spatial distribution of the pre-ignition initiation locations

For further characterization of pre-ignition, different specific pre-ignition initiation areas are shown in the figures below. Here, a division was made between initial pre-ignition and follow-up pre-ignition.

Initial pre-ignitions

Figure 5-36 shows the typical pre-ignition initiation areas of initial pre-ignitions. There was only one initial event (red circle) with more than one nucleus of initiation in all of the recorded pre-ignitions. Otherwise, there were single-core initiation areas around the piston crevice circumference. Flame propagation occurs from or at the specific piston crevice location. A glowing object entering or exiting the piston crevice can often be observed. Pre-ignition initiation in the combustion chamber volume occurred predominantly in the area around the spark plug and in the vicinity of the piston crown. A glowing solid particulate matter history can always be detected at which the flame propagation starts. The pronounced tumble flow field influences the movement path of the solid particulate matter. The initiation point framed in green represents a special characteristic of extremely long pre-ignition events. Typically, initiation takes place at/around this piston deposition point, which continuously initiates pre-ignition under light-emitting near top dead center over several cycles.

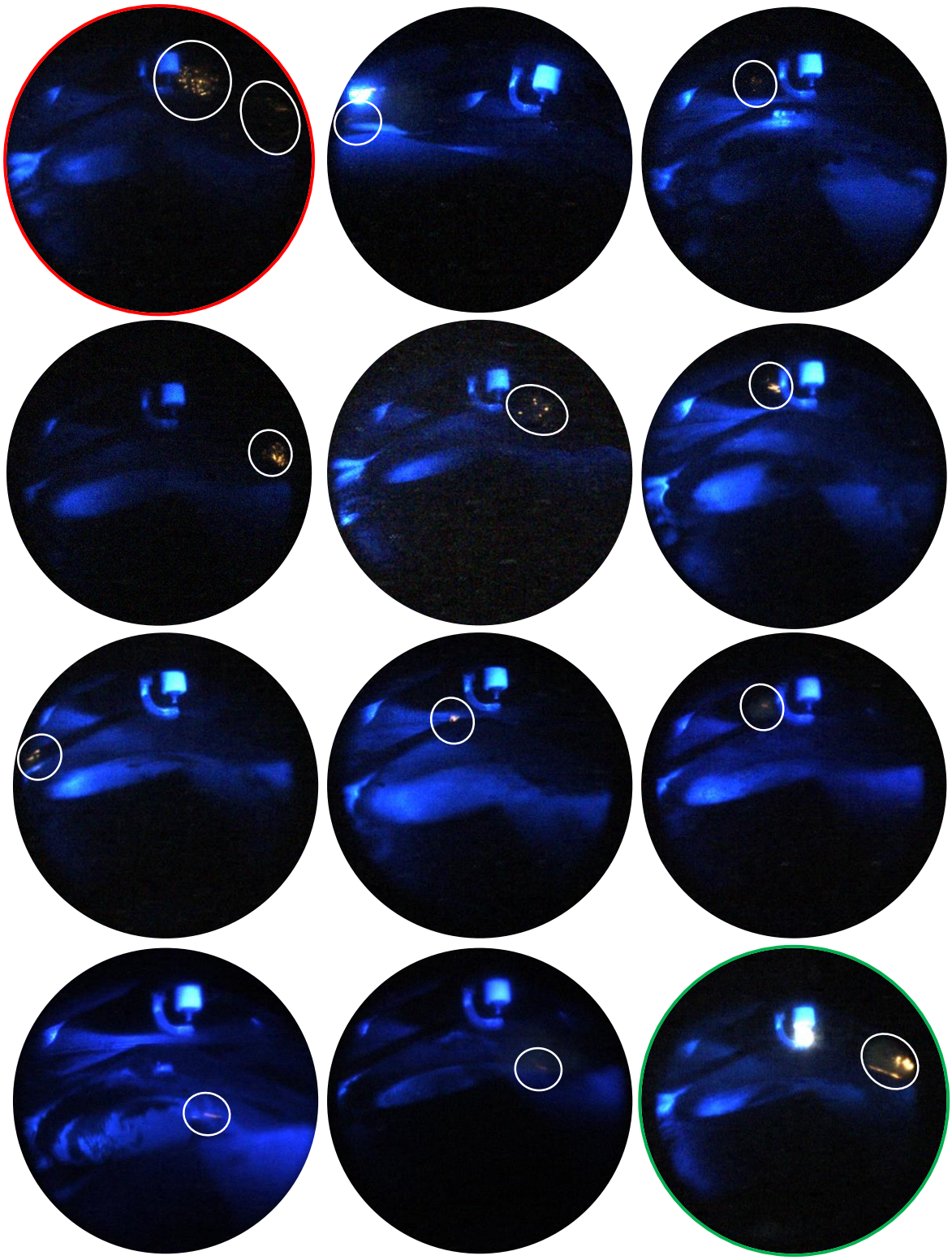

Figure 5-36: Characteristic initial pre-ignition initiation locations.

Follow-up pre-ignitions

The typical initiation pattern of follow-up pre-ignition events is shown in Figure 5-37. There is no discernible change in the typical initiation area (top row). However, the increased occurrence of multi-nucleus pre-ignition initiations can be observed (bottom row). As shown above, this must be due to the deposit detachment potential of initial pre-ignitions. This sometimes leads to extreme pressure peaks in the following knocking combustion. Overall, all fully detectable pre-ignitions show a glowing solid particulate matter history.

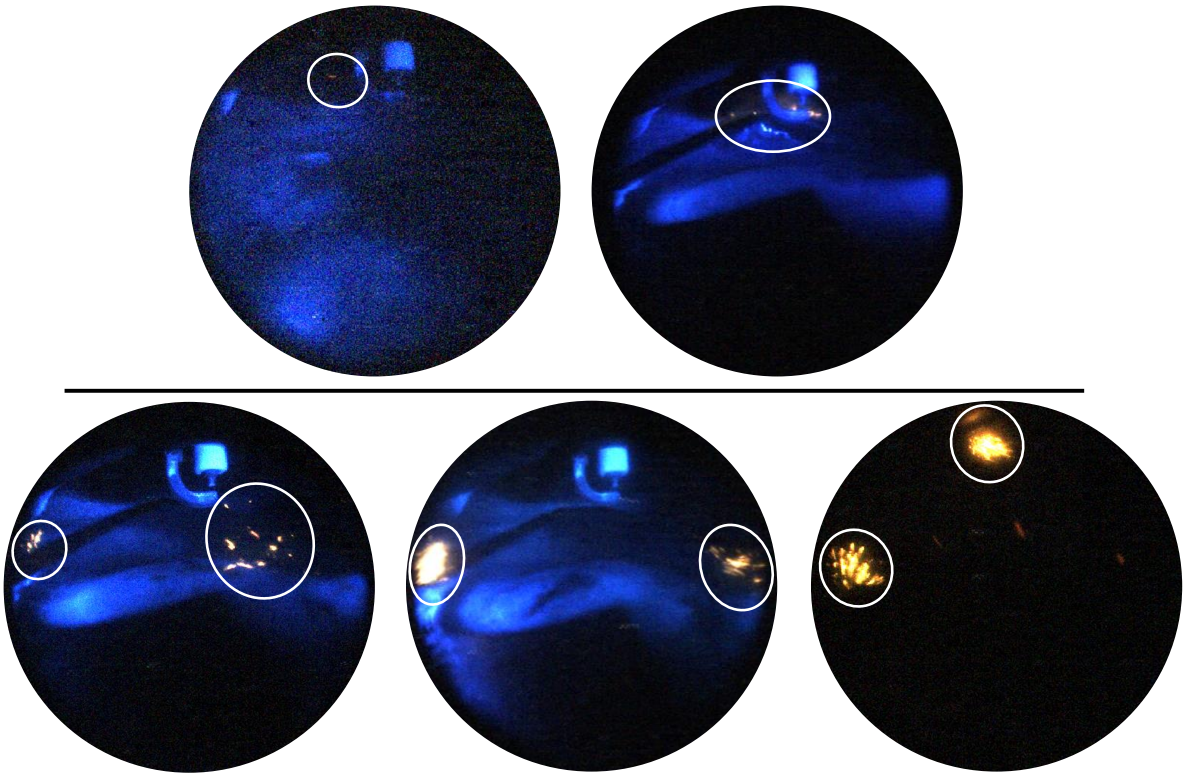

Figure 5-37: Initiation characteristics of follow-up pre-ignitions.

General initiation characteristics

In summary, we can observe three specific pre-ignition initiation characteristics (Figure 5-38). An initiation in the combustion chamber volume, the initiation at/in the piston crevice area, as well as the "special case" of an initiation source existing over several cycles on the piston crown area near the crevice. All the indications shown speak for a solid particulate matter/deposit-driven pre-ignition mechanism. There was no detection of a direct oil droplet ignition or a glow ignition through hot components.

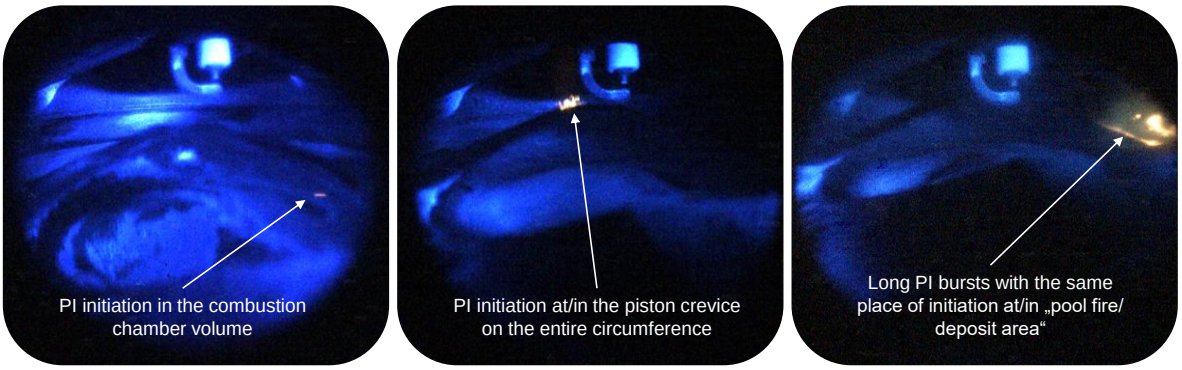

Figure 5-38: Different pre-ignition initiation characteristics.

Subsequently, the detailed optical analyses of typical pre-ignitions events are presented.

5.2.4.3 Single pre-ignition

Figure 5-39 shows the typical course of a singular pre-ignition event. In the cycle before the pre-ignition initiation, the typical combustion pattern with a strong pool-fire presence is shown. The pre-ignition is initiated by a glowing solid particulate matter emerging from the piston crevice near top dead center, which initiates flame propagation near the piston head. In the expansion stroke of the pre-ignition cycle, the process of particle detachment from specific spray/ liner interaction areas can be detected. In this case, this is optically only possible due to a relatively mild pre-ignition. There is also a luminance-dominated combustion behavior at the

piston edge, which indicates an increased accumulation of oil and fuel. Some of these initially burning particles survive the subsequent charge exchange and can still be recognized in the subsequent cycle. The bouncing of a glowing particle on the spark plug base electrode without form changing in the exhaust stroke illustrates the solid substance of these detached particles. The majority of pre-ignition events consisted of individual pre-ignitions.

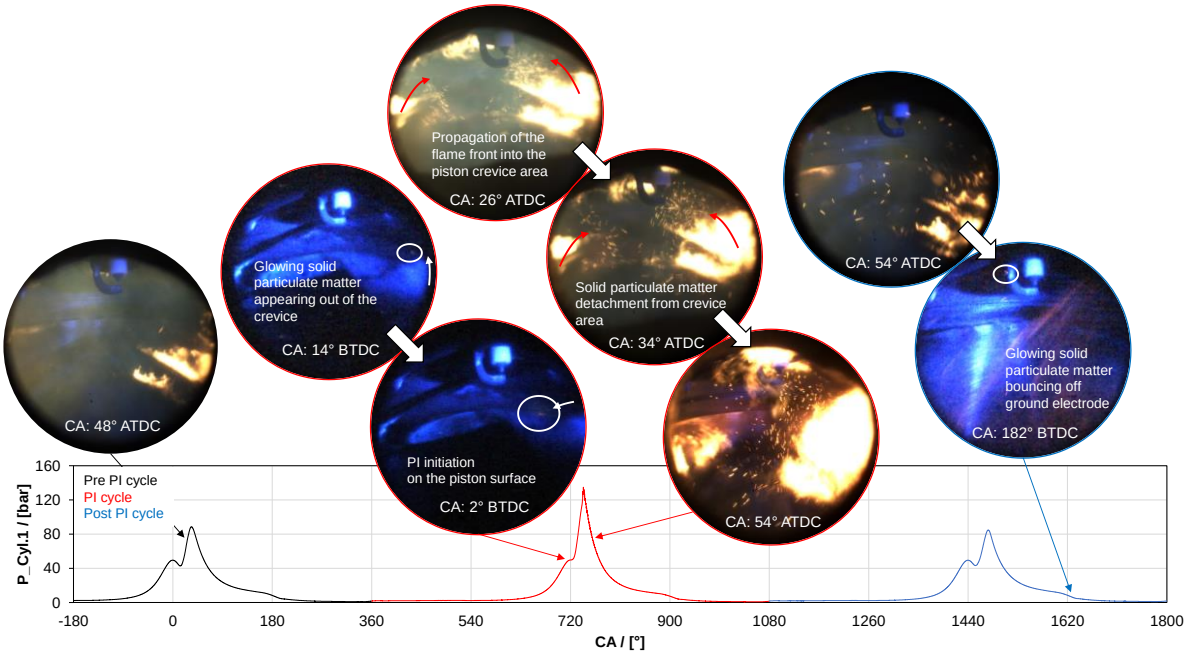

Figure 5-39: Typical course of a single pre-ignition.

5.2.4.4 Short pre-ignition series

In addition to single pre-ignition events, there were also "classic" pre-ignition series. Probably due to the strong scavenging effect, this mainly resulted in series of two pre-ignitions. A representative example is shown in Figure 5-40.

The initial pre-ignition is initiated by a glowing particle following the tumble flow. The start of glow likely occurs during compression. After a rebound at the inlet valve, the air-fuel mixture is ignited near the spark plug. In the following cycle, a large number of burning and glowing particles can be seen during combustion and expansion. These must have survived the charge exchange and do not yet seem to have the potential to trigger a further pre-ignition in the compression stroke. Only in the next but one cycle is the repeated initiation of a pre-ignition visible through a particle that begins to glow in the compression stroke. The pure number of particles is no guarantee for the generation of pre-ignition, but it explains the increased occurrence of more than one ignition nucleus during subsequent pre-ignitions. This pattern speaks for the influence of an oxidative process of these particles, which in turn is influenced by the combustion air-fuel ratio of the specific cycle.

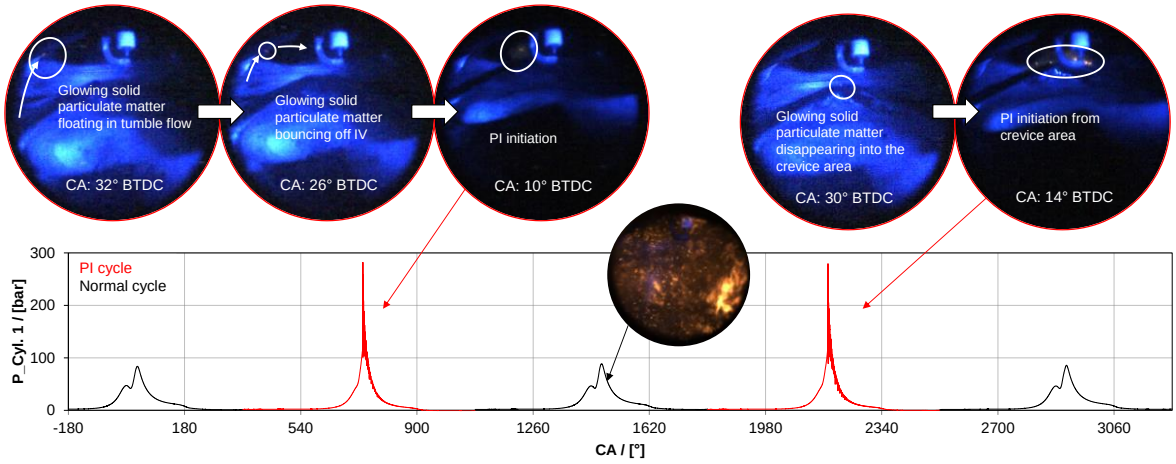

Figure 5-40: Typical course of a short pre-ignition series.

5.2.4.5 (Very) long pre-ignition series

The rare form of an extremely long pre-ignition series shown in Figure 5-41 illustrates the general challenge of pressure-based pre-ignition detection and thus the statistics-driven macroscopic pre-ignition interpretation. Pre-ignition events can occur which are not detectable by means of a pressure signal. In the event shown, these correspond to the first 13 cycles. There is a constant pre-ignition initiation source on a deposition point of the piston in the pool fire area (most dominant deposit point), which is only stopped by the occurrence of the pre-ignition event **1** with two initiation sources. The resulting greater pressure amplitudes suggest a sudden release of these critical deposition components. The picture resulting from **2** shows a congruent characteristic to Figure 5-40.

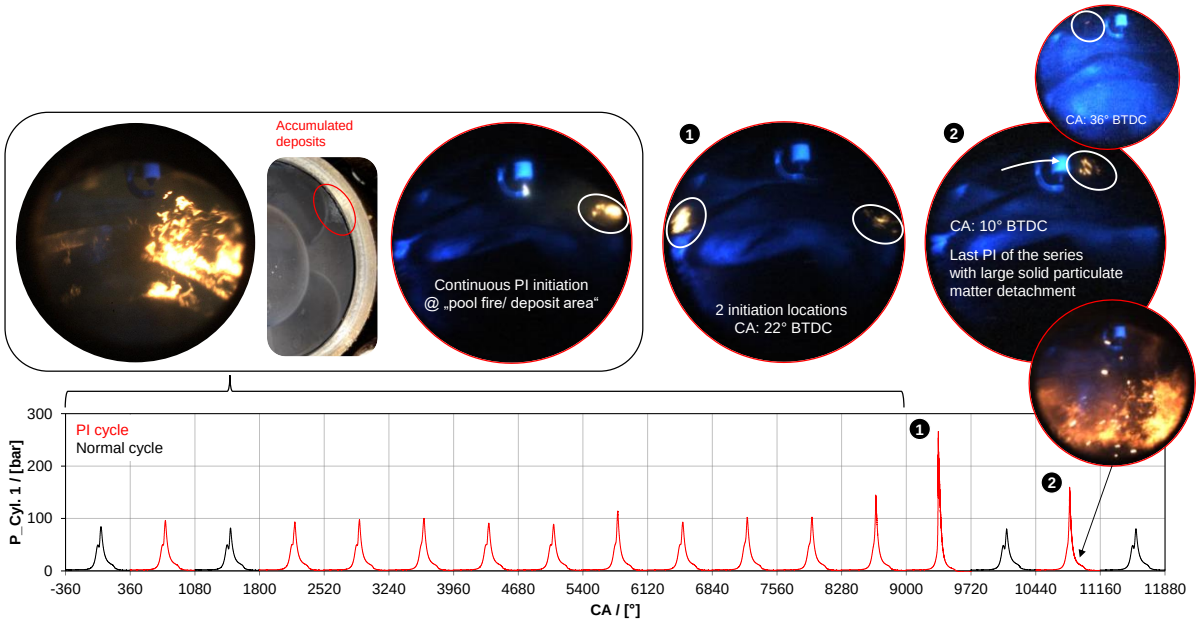

Figure 5-41: Typical course of a very long pre-ignition series.

5.2.4.6 Initiating mechanism

Figure 5-42 shows the overview of the evidence-based pre-ignition formation observations synthesized from all optical pre-ignition characterizations. **1** shows the start of glowing of a small moving particle near top dead center. The later pre-ignition initiating glowing particle at 14° CA BTDC is, however, much larger. This leads to the conclusion that particles must have a minimum size in order to have the potential to trigger a pre-ignition. Since the image details

in 1 are an observation period of a subsequent pre-ignition, a large number of particles are present in the combustion chamber at this point in time. The fact that only two of these particles are detected glowing in the observation volume causes the assumption made above of different specific particle properties. A purely morphological effect seems to be unlikely here, which is why it is presumably a different material composition. There seem to be different reactivities of individual particles.

The image details from 2 confirm the assumption of solid substances that cause pre-ignition. This is confirmed by the ability of the particles to bounce off the inlet valve without changing their shape. The shown particle detachment from specific deposition areas (pool fire area) shows the interrelationship between the formation of deposits and the appearance of particles in the combustion chamber.

3 shows a glowing particle in the intake stroke of a single pre-ignition cycle with no pre-ignition history. The fact that there is a glowing particle here despite the cool combustion chamber conditions deepens the assumption that the particles have to be reactive. The activation conditions for this reactive process must have been set in the combustion process of the previous cycle. The strong observed air-fuel ratio influence on the pre-ignition frequency is presumably evident here. This must have the opposite effect. On the one hand, sub-stoichiometric combustion increases the formation of deposits, and on the other hand, available oxygen during combustion offers the possibility of setting oxidative activation conditions for particles.

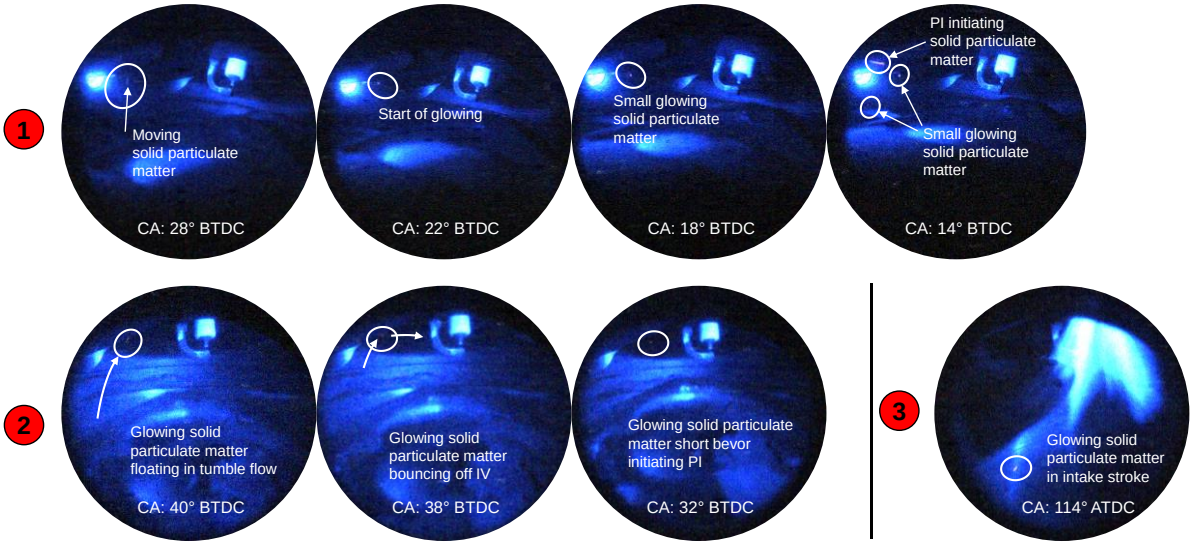

Figure 5-42: Solid particulate matter pre-ignition initiation characteristics.

The evaluations of the previous preignition characterizations show the picture of a multi-cyclic preignition mechanism, which is defined by (reactive) deposit formation and the release of (reactive) particles. These assumptions are validated in the simulative investigations.

5.2.5 Key experiments

To further establish the mechanism, the results of the key experiments carried out are presented below.

5.2.5.1 LIF detection of engine fluids

LIF fuel detection

In order to detect the in-cylinder fuel behavior in pre-ignition operation, the engine was operated with a tracer/ fuel mixture with a concentration of 22.3 mg Lumilux CD345 per 200 ml High LSPI fuel. In the ex-situ LIF investigations, this concentration resulted in approximately the greatest fluorescence intensity. Figure 5-43 shows high-speed recordings with the LIF engine setup in the "ISO load point". During the injection, the green fluorescence signal of the fuel

spray is clearly visible. In the expansion stroke, there is also a clear build-up of fuel/ tracer on the bore to / piston crevice area. This confirms the assumption of the large spray/ liner interaction in engine operation with a pre-ignition critical parameter setup.

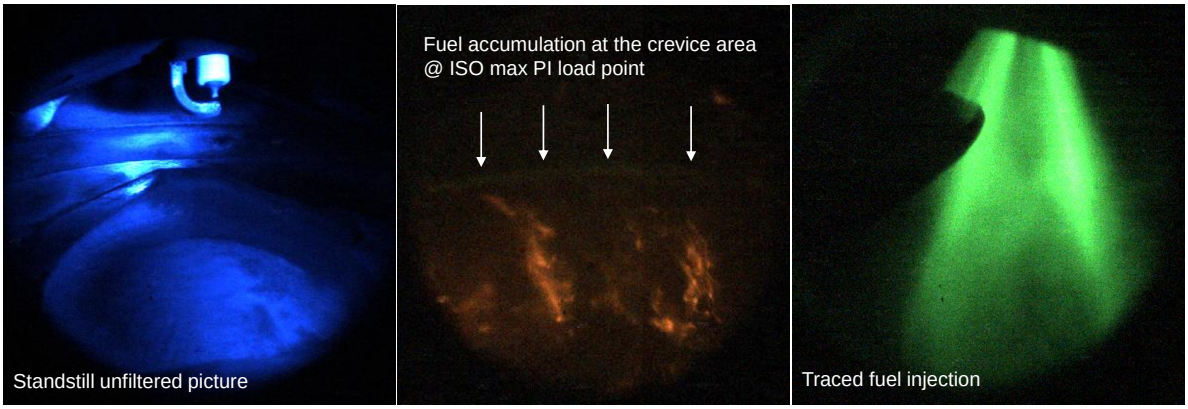

Figure 5-43: Traced fuel high-speed detection.

In the CFD simulations, specific locations of fuel film applications on the liner could be analyzed in the "ISO load point". These could not be localized under high-speed boundary conditions during engine operation due to the short exposure time and the resulting relatively weak fluorescence signal, as well as the increasing access window fouling. For this reason, the fuel fluorescence image was taken under longer exposure time after an "emergency stop" of the engine from the "ISO load point". The result and the CFD and deposition correlations are shown in Figure 5-44. The fluorescence image after the engine emergency stop shows a clearly inhomogeneous fuel accumulation image in the area of the bore top / piston crevice. The specific attachment points correlate well with the liner wetting points occurring in the spray and liquid film simulation in the "ISO load point". A correlation can also be found in the deposition image (**1**, **2**, **3**). In the simulation, point **2** shows the largest amount of fuel applied to the liner, which corresponds to the "dominant" crevice deposit point. The specific deposit point found on the piston at the position of the constant pre-ignition initiation (pool fire area) from the extremely long pre-ignition series (**4**) correlates with the CFD fuel piston wetting point.

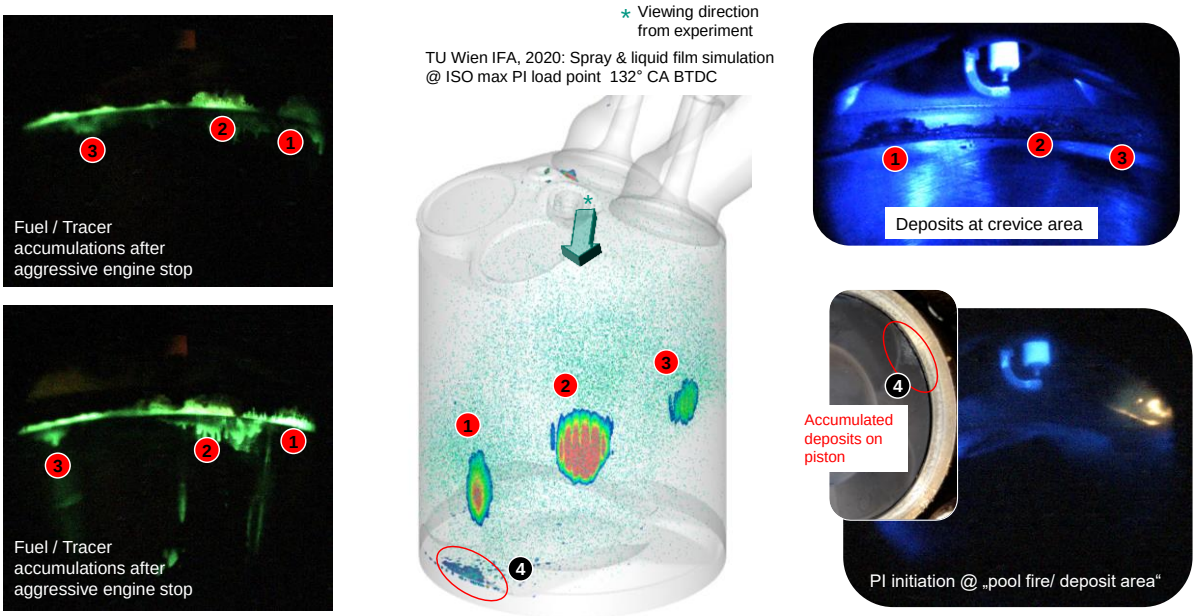

Figure 5-44: Experiment / CFD correlation of fuel liner interaction and deposit build-up.

These correlations clearly illustrate the connection between specific fuel interaction points and the corresponding build-up of deposits and thus clearly confirm the described mechanisms from the pre-ignition characterizations. Another weakly observable phenomenon is the detachment of oil/ fuel droplets at the piston crevice area. Since there is a mixture of oil and fuel there, an exact assignment is no longer possible. Figure 5-45 gives an overview of the phenomenon with different engine states.

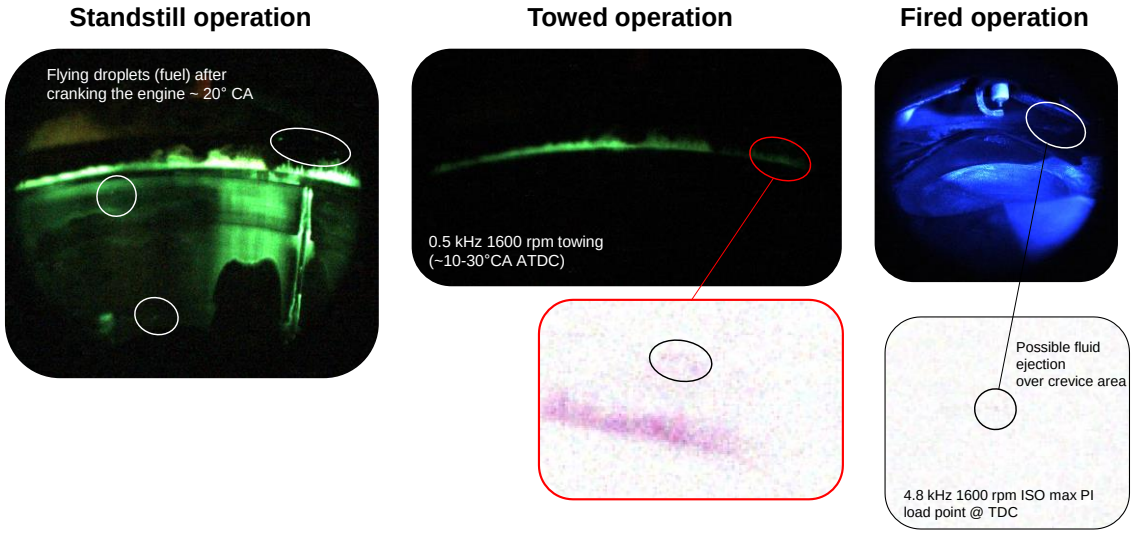

Figure 5-45: Detached fluids at different engine operating states.

When the engine is at a standstill, floating oil/ fuel drops can be observed after operation in pre-ignition areas due to the manual rotation of the engine. In towed engine operation, the detachment of oil/fuel droplets in the area of the piston crevice is weakly detectable. There is also evidence of oil/ fuel droplet detachment at the pre-ignition operating point. This process represents a physical enabling mechanism for the formation of deposits from oil components. This process was also shown in [59].

LIF oil detection

The detection of oil droplets during engine operation proved to be very challenging. This is due, among other things, to the general optical limitations of LIF operation on the real engine system and the operating conditions under full load. In direct comparison to fuel fluorescence, oil shows significantly worse optical properties (light penetration) as well as a poorer tracer concentration potential. For these reasons, no oil fluorescence could be detected with either tracer (Lumilux CD345 and PM567A) in normal "ISO load point" cycles. However, the hypothesis described in [56],[57] of the ejection of oil-containing droplets in the case of a super-knocking event with detonation waves could be included in Figure 5-46 and thus confirmed. In particular, this can lead to further particle generation and thus contribute to the development of subsequent pre-ignitions and further deposit build-up. In this specific case, 256 mg of Lumilux CD345 was used for 4.2 liters of Fuchs 5W30.

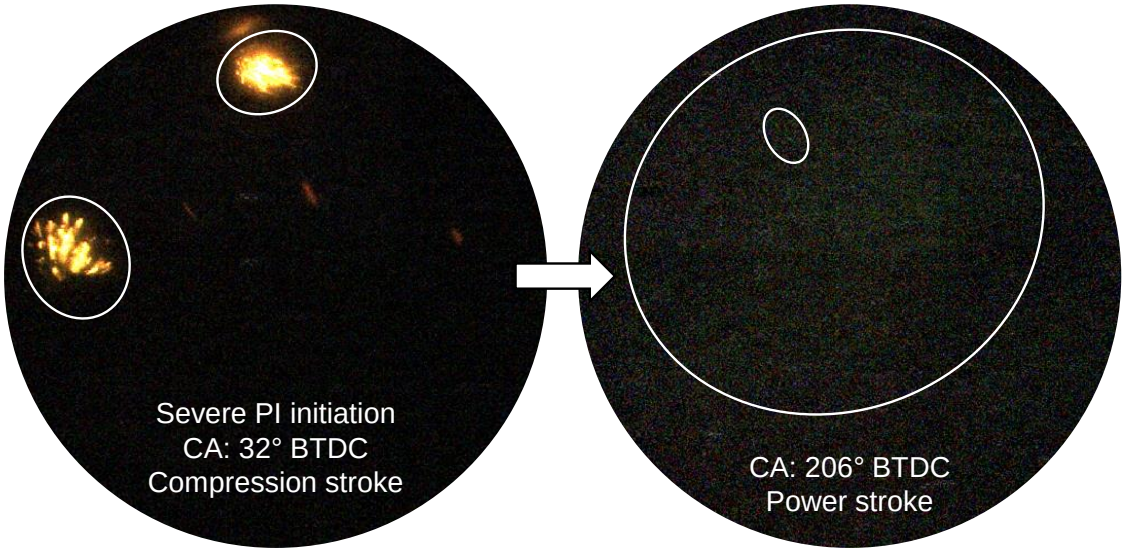

Figure 5-46: Detached oil droplets by pre-ignition with super knock.

Oil fluorescence detection was also used in the oil injection experiments (25mg PM567A / 200 ml Fuchs 5W30).

5.2.5.2 Oil injection investigations

Different oil properties showed a significant influence in the statistical "macroscopic" pre-ignition characterization. In order to better understand the role of the engine oil in the pre-ignition mechanism, the effects of an additional oil introduction into the combustion chamber at different load points were investigated. A strong influence on the preignition process was found, which is to be expected. The pre-ignition frequency increases strongly depending on the amount of oil injected. The load area in which pre-ignition occurs also expands strongly downwards. There is a frequent occurrence of relatively mild pre-ignitions. The introduction of oil via the inlet valve 2 of the first cylinder results in the characteristic shown in Figure 5-47. Among other things, there is a specific deposit formation at the exhaust valve 2 opposite the oil inlet. This could be correlated by means of LIF oil droplet tracking with an oil droplet movement path in the cylinder at the "ISO load point" as well as a deposit surface ignition pre-ignition initiation at the exhaust valve. The pronounced scavenging effect explains the special movement path. For a clearer presentation, the oil drop representations are inverted grayscale images derived from the original RGB images. The deposits created in this way serve as reference deposits in the further course of deposit characterization. All optical results refer to an injected oil mass flow of 0.35 g/min Fuchs 5W30.

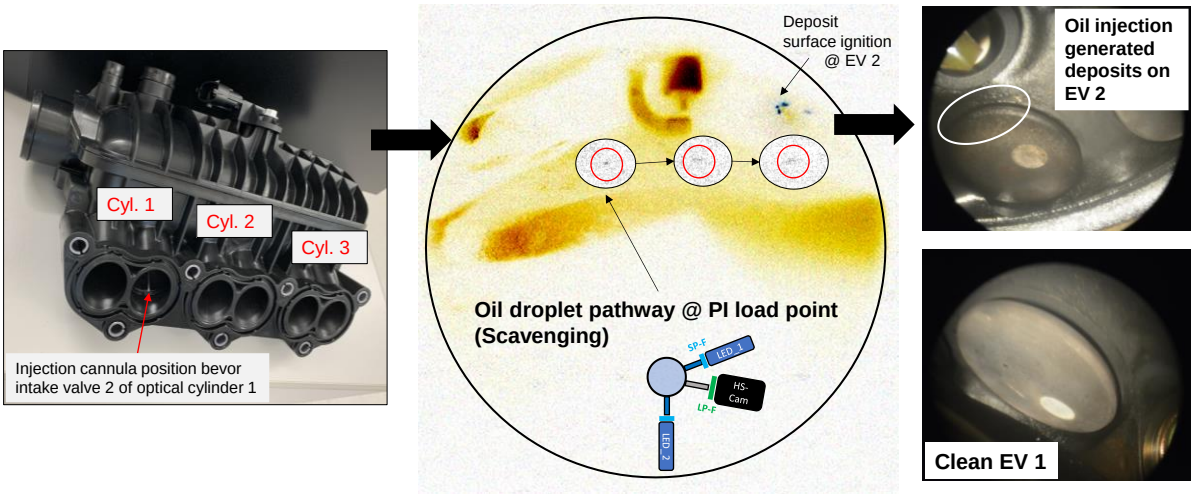

Figure 5-47: Oil path in combustion chamber at pre-ignition load point with correlated deposit area.

A direct optical pre-ignition comparison shows a clear difference in the initiation characteristics. Figure 5-48 summarizes the key elements.

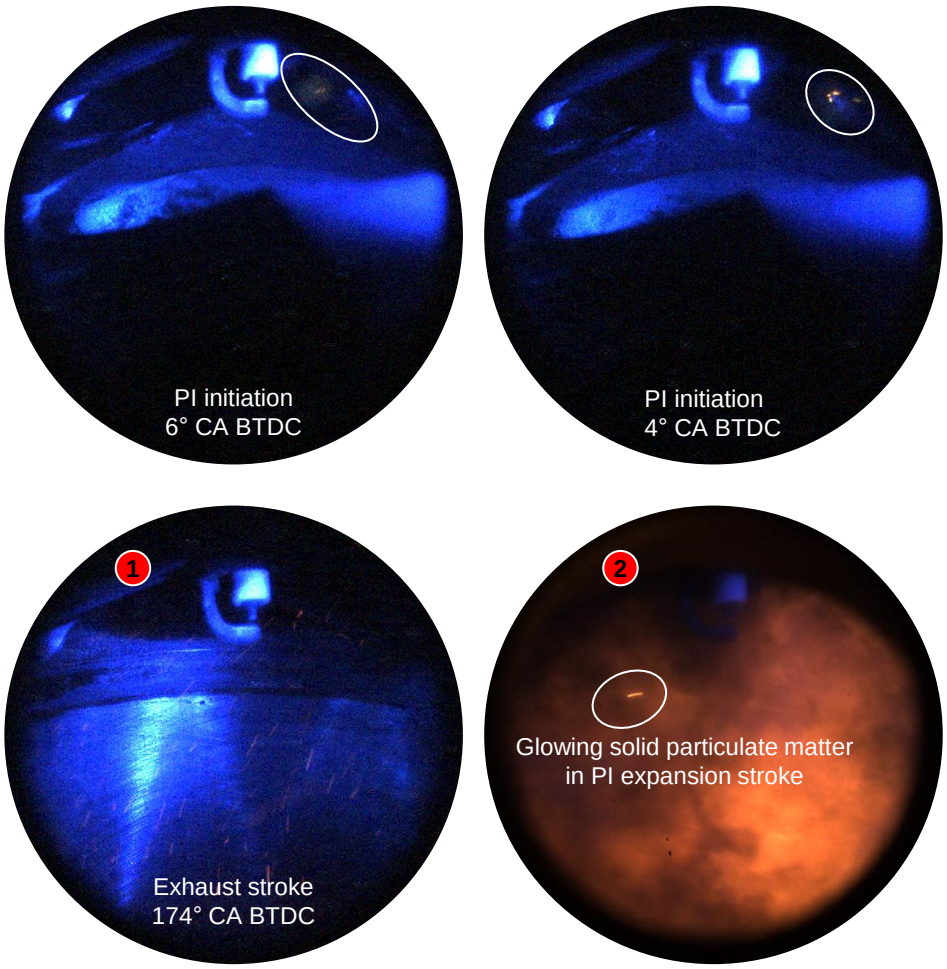

Figure 5-48: Oil injection pre-ignition characteristic.

The majority of all pre-ignitions generated are due to deposit surface ignition at the exhaust valve 2. Oil droplet ignition could not be observed. The fact that each pre-ignition generation requires a temporal oil injection lead time gives indications of necessary conversion processes in the form of deposit formation. In addition to the surface ignitions, there were also isolated cases of the well-known pre-ignition initiations by glowing particles. **2** shows a large glowing

particle in the expansion phase of a pre-ignition. Here, the oxygen content in the residual gas must have an effect on the particle oxidation process. The strong influence of the air-fuel ratio on the pre-ignition rate also supports this assumption. **1** shows the increased presence of glowing particles in the exhaust stroke after pre-ignition compared to the optical characterizations without oil injection. This suggests a larger proportion of reactive particles/deposits, which in turn, along with the additional deposits, is an explanation for the greatly increased pre-ignition occurrence. These statements are supported by a macroscopic pre-ignition characterization with oil injection. The results are shown in Figure 5-49.

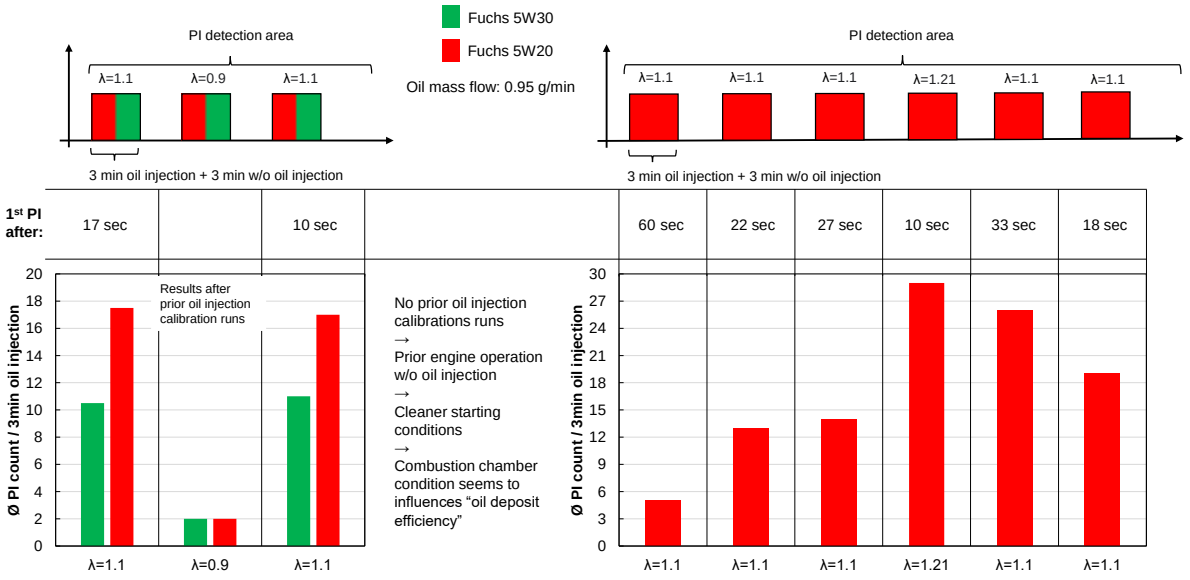

Figure 5-49: Air-fuel ratio oil injection test runs.

For the tests, the engine load was lowered to 170 Nm with a close to standard engine parameter setup while adjusting the pre-ignition detection thresholds (analog to the macroscopic pre-ignition characterizations). The engine oil was also changed to Fuchs 5W20. Under these conditions, no pre-ignition occurs during normal operation without oil injection. Unwanted cross-influences are thus avoided. The injected oil mass flow was increased to 0.95 g/min for all tests.

The oil comparison test series (Figure 5-49 left) consisted of a stationary engine operating point with three three-minute oil injection phases. In between are three-minute phases without oil injection. Two injection phases were run with λ=1.1, the intermediate phase with λ=0.9. The number of preignitions refers in each case to the mean value from three test series for the respective three-minute oil injection phase. No further pre-ignitions were detected in the intermediate phases or after the end of the last oil injector phase. The air-fuel ratio correlation known from the macroscopic pre-ignition characterizations is evident. For both oils, the pre-ignition level drops extremely for an air-fuel ratio of 0.9. The expected difference in the pre-ignition level of the oils is also confirmed. Looking at the times until the first pre-flaming occurs in the lean areas, it is noticeable that a certain start-up time is always required. This supports the assumption that a conversion/deposition process must occur before pre-ignition can be initiated. The time to initiate pre-ignition in the third block is always shorter than in the first block. When assuming a deposit-dominated pre-ignition mechanism, the oil deposition efficiency seems to be increased by certain preconditioning (changed surface morphology and roughness) of the combustion chamber.

The air-fuel ratio correlation is also shown in the lean range in another test series (Figure 5-49 right). The test procedure is analogous to the first. There are six three-minute oil injection phases and corresponding phases without oil injection. Of these, five phases are run with λ=1.1 and one phase with λ=1.21. The combustion chamber starting conditions differ between the test series, as oil injection calibration runs were carried out in advance for the oil comparison

test series. Accordingly, the assumed influence of combustion chamber preconditioning is confirmed by an extreme extension of the time interval until the first pre-ignition occurs (60 sec vs. 17 sec). The initial pre-ignition level is also lower but increases with the next two λ=1.1 oil injection phases. Increasing the air-fuel ratio to λ=1.21 results in a drastic increase in the number of pre-ignitions. The downstream oil injection phases with λ=1.1 lead to a reduction in the number of pre-ignitions and show a very comparable pre-ignition level to the oil-comparing test series.

In summary, a deposit-dominated pre-ignition mechanism can be identified even with additional oil injection. Pre-ignition was initiated by deposit surface ignition or glowing particles. A general pre-ignition increase can be explained by the specific placement of deposits and the associated better oxygen availability, as well as a generally observed more reactive "deposit pattern" (more glowing particles at the end of the exhaust strokes). The strong dependency of the pre-ignition level on the air-fuel ratio here determines the dependency of the pre-ignition level on an oxidative influence on the deposition/ particle history. Glowing particles appear in the expansion phase of combustion, which is clearly influenced by the residual oxygen in their oxidation behavior. This oxidative deposit / particle preconditioning appears to be a pre-ignition influencing mechanism.

The more reactive “deposition pattern” can be shown in the following deposit characterizations.

5.2.5.3 Combustion chamber deposit characterization

For the deposit characterizations, piston deposits were collected from four specific locations after an "ISO load point" pre-ignition run through an engine disassembly. As a reference deposit, oil deposits around exhaust valve 2 were collected through an optical access after an oil injection run ("ISO load point"). Figure 5-50 shows the specific deposit extraction points and the SEM secondary electron contrast images of the deposit samples. These give an overview of the deposit surface topology.

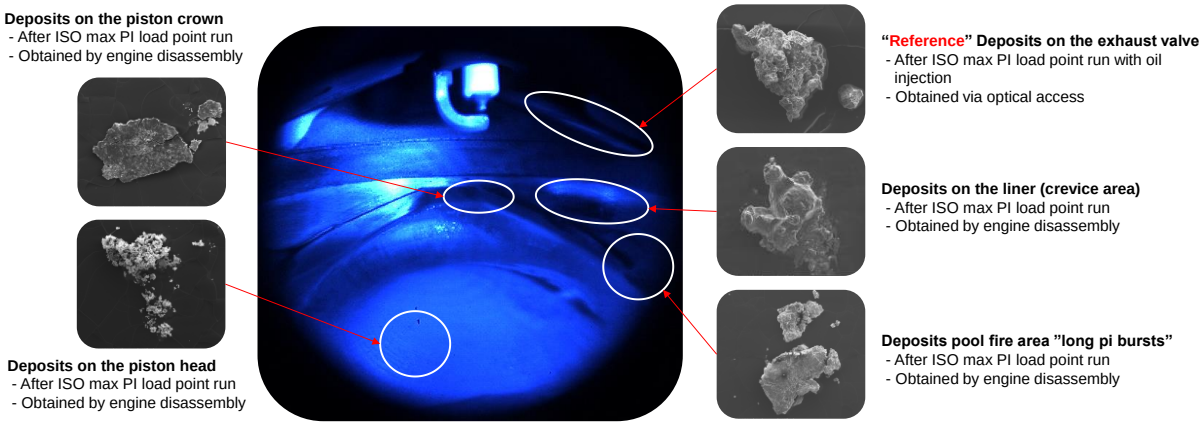

Figure 5-50: Combustion chamber deposit extraction areas.

SEM-BSE and SEM EDX spectroscopy analysis

Figure 5-51 shows the SEM BSE and EDX spectroscopy analysis of the oil reference deposit. The EDX spectrum shows many oil (additive) element-specific peaks. The red spectrum corresponds to a contrast point analysis, and the black spectrum corresponds to a grid averaging over the entire deposit sample. In addition to the main component carbon, many oil additive-specific elements can be seen. Among them is the element calcium, which has a strong influence on pre-ignition [52]. The Z-contrast image shows many high-contrast areas, which on the one hand indicates the general qualitative oil additive component distribution and, on the other hand, gives information about the element frequency. This allows a qualitative reference comparison with the analyses of the four "ISO load point" deposit samples.

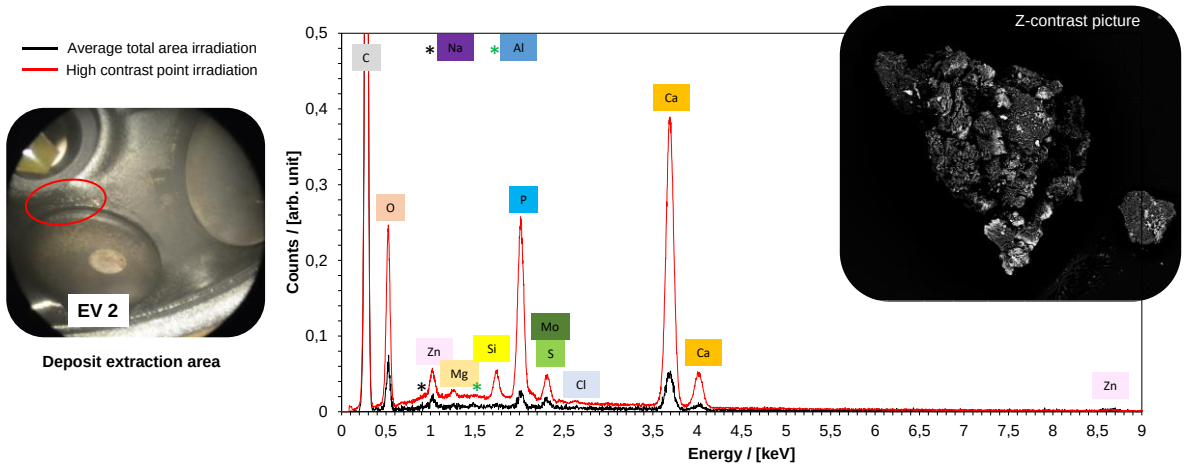

Figure 5-51: SEM BSE and EDX analysis of oil injection reference deposit.

Figure 5-52 shows the direct comparison of the SEM BSE and EDX spectroscopy analyses of the oil reference deposit to the deposits at the pool fire piston edge position (long pi series) and the deposits at the bore top/ crevice. The EDX spectra are very comparable. Thus, all deposits contain oil additive elements. The Z-contrast images show the most extensive accumulation of oil additive elements in the sample, which was involved in the initiation of the extremely long pi series. The bore top / crevice sample, on the other hand, shows only single contrast points. A correlation between oil additive components and pre-ignition potential can be assumed.

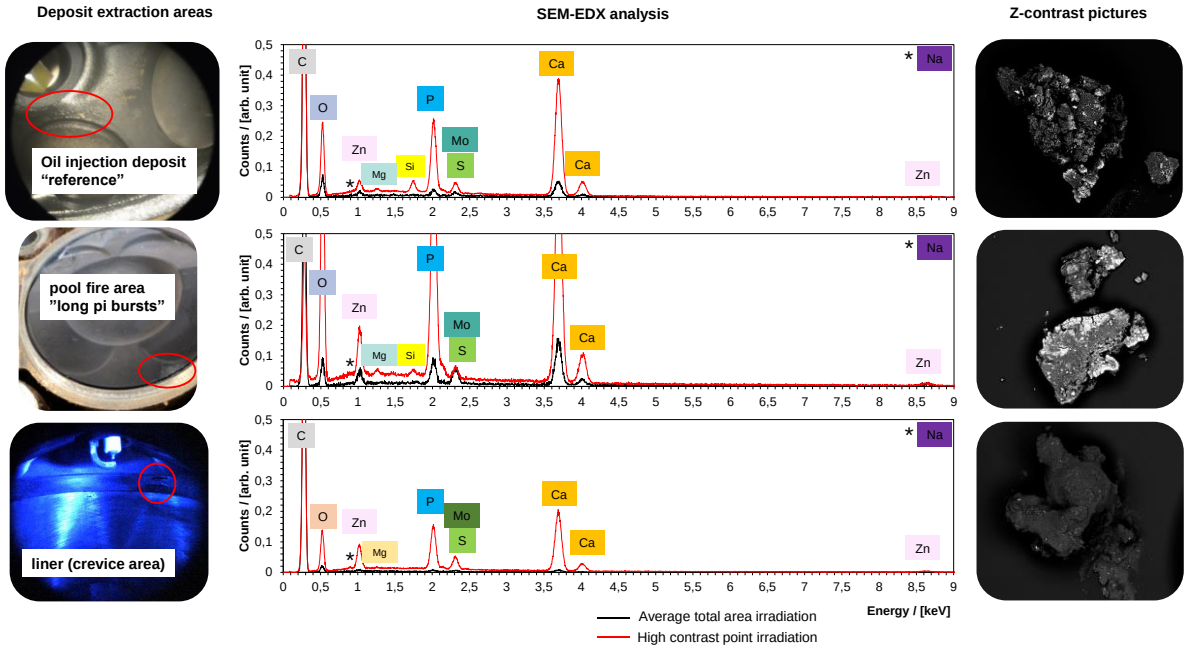

Figure 5-52: SEM BSE and EDX analysis of oil ash dominated deposits.

The deposits on the piston head and the piston crown show a completely different picture (Figure 5-53). Only in the deposit sample on the piston crown are traces of oil additive elements to be found. This could be an indication of the "physical enabling mechanism" of the fuel/ oil detachment from the piston crevice. In the deposit sample from the piston head, only elements of carbon and oxygen could be detected. The sample areas did not show any conspicuous behavior in the optical pre-ignition characterizations.

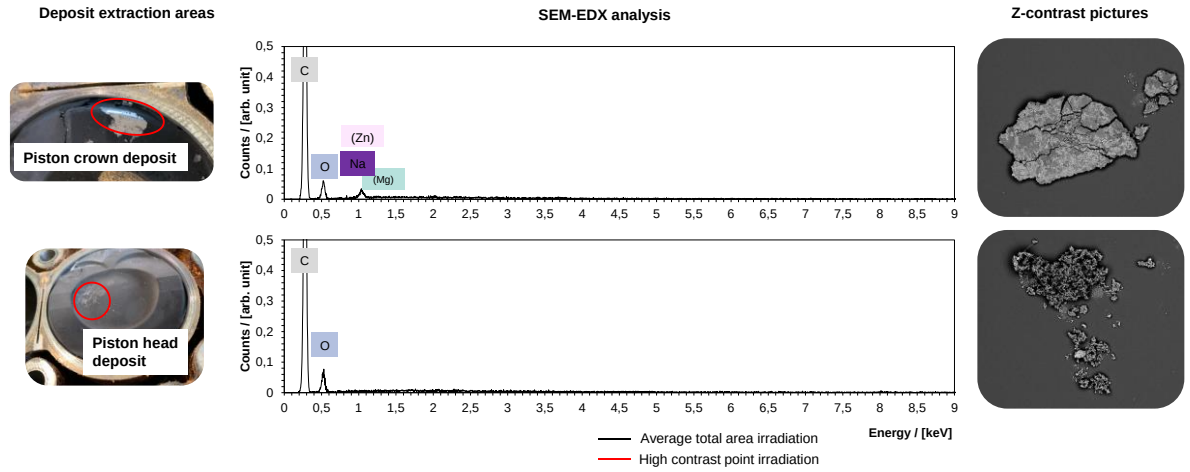

Figure 5-53: SEM BSE and EDX analysis of deposits with few oil ash components.

Overall, there is a clear correlation between deposits with oil additive components and reactive combustion chamber locations. In Figure 5-54, a correlation of pre-ignition initiating deposits, which were formed under different mechanism pathways, is shown. The EDX spectrum correspondence shows that the deposit caused by the spray/ liner interaction is also interspersed by oil additive components. This also applies to the general deposits from the bore top/ piston crevice.

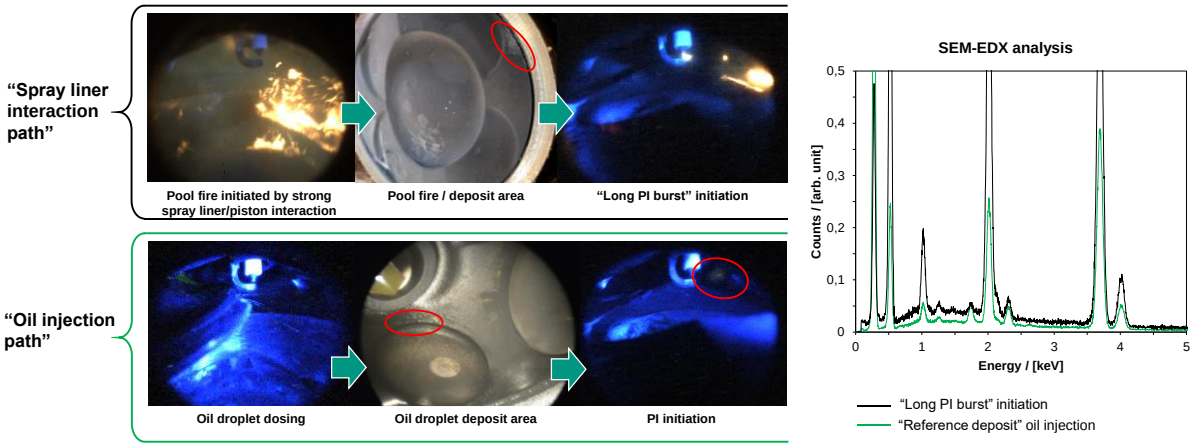

Figure 5-54: Comparison of the pre-ignitions from different deposit build-up pathways.

TGA oxidation reactivity analysis

With the help of thermal gravimetric analysis, the effect of oil additive element inclusions in the deposits on their reaction potential can be investigated. Figure 5-55 shows an oxidative reactivity difference between deposit samples containing oil additive components and a deposit sample in which only carbon and oxygen could be detected. There is a clear difference in reactivity. Deposit samples that contain oil additive components show a significantly earlier oxidation behavior. A pure influence by the deposit morphology is excluded in the T_{MAX} range of 450°C [60]. It remains to be seen which exact effect this oxidation influence is based on.

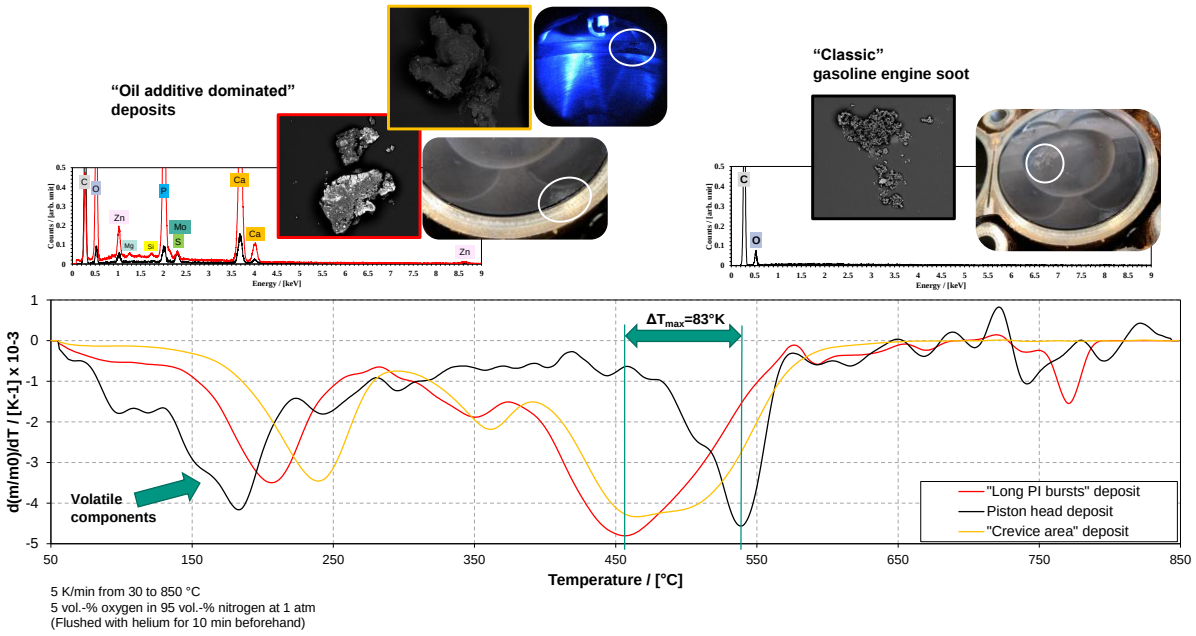

Figure 5-55: TGA comparison of deposits.

The reactive "deposit pattern" suspected in the oil injection tests can thus be confirmed. Specific combustion chamber deposits have oil additive components and thus have a greater reaction potential. This explains the occurrence of a constant deposit ignition source of extremely long PI series but also the formation of reactive particles and thus the general oil influence of the demonstrated pre-ignition mechanism.

5.3 Numerical results

5.3.1 Mixture Preparation and Wall film analysis

The goal of the simulation was to predict the fuel film formation and mixture preparation. Therefore, the simulation time could be limited to a single engine cycle without including the combustion process. The beginning of the simulation was set to 270 °CA to minimize the errors made in the initialization process. The end of the simulation was set to spark timing (724°CA).

The described spray and the fuel liquid phase models were transferred to the full engine CFD model. Activation coefficients were calculated for droplet and film evaporation using the UNIFAC method to be consistent with the fuel component selection model. The droplet-wall interaction was calculated by using the Bai-Gosman impingement model. The turbulent flow field was described using a RANS approach in combination with a k-ε RNG turbulence model.

Wall film analysis

The investigated operation point is the “ISO-operation point” described in chapter 5.2.3. Figure 5-56 shows the temporal evolution of the liquid film mass that is formed during fuel injection. Additionally, a plot of the liquid film distribution in the combustion chamber at EOI is shown.

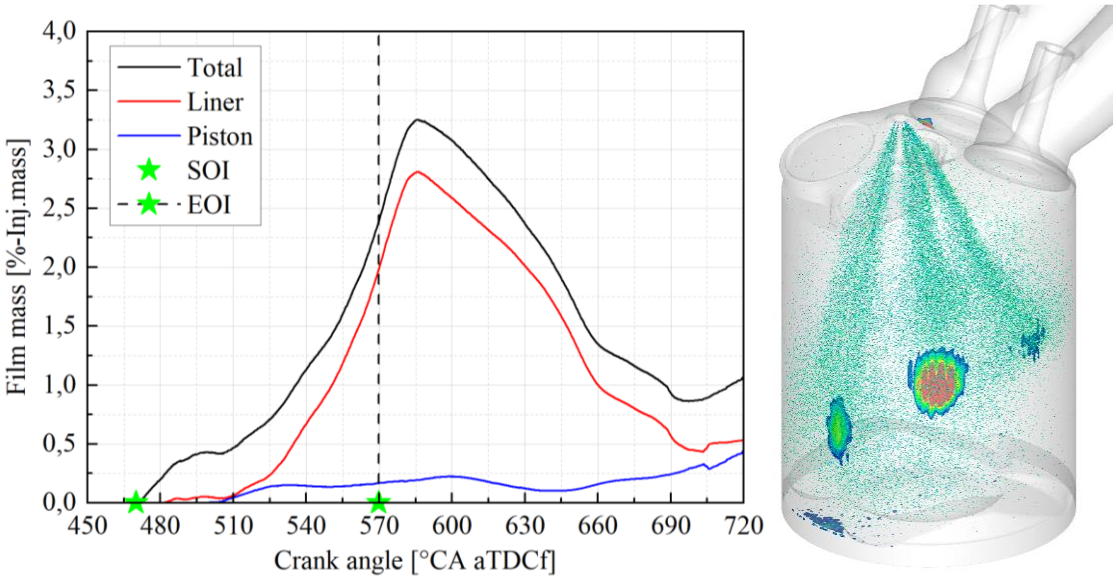

Figure 5-56: (left) Temporal evolution of the liquid film mass, (right): film distribution at EOI.

At the beginning of the injection, the intake valve lift is close to its maximum. Therefore, some droplets are hitting the valve surface and generate small amounts of film. The decreasing charge motion velocity toward BDC enables the spray to reach the cylinder liner and the piston surface. The film mass peaks shortly after EOI at 585 °CA aTDCf and decreases afterward due to evaporation. The majority of the liquid film mass is concentrated at three distinct areas on the liner and one region on the piston surface. Furthermore, it can be observed that the wetted piston area is underneath a distinct fuel-wetted liner area.

The heat transfer from the liner walls to the wetted areas is too low to evaporate the film completely. Therefore, the piston wipes off the liquid film during the compression motion. This leads to fuel accumulation in the piston crevice volume, where it survives till the end of the simulation. Near TDC, the piston deceleration forces the film back up towards the piston top land, shown in Figure 5-57. Although the simplified film model is not sophisticated enough to accurately calculate thick film motions, it indicates the trend of upward creeping liquid in the piston crevice area.

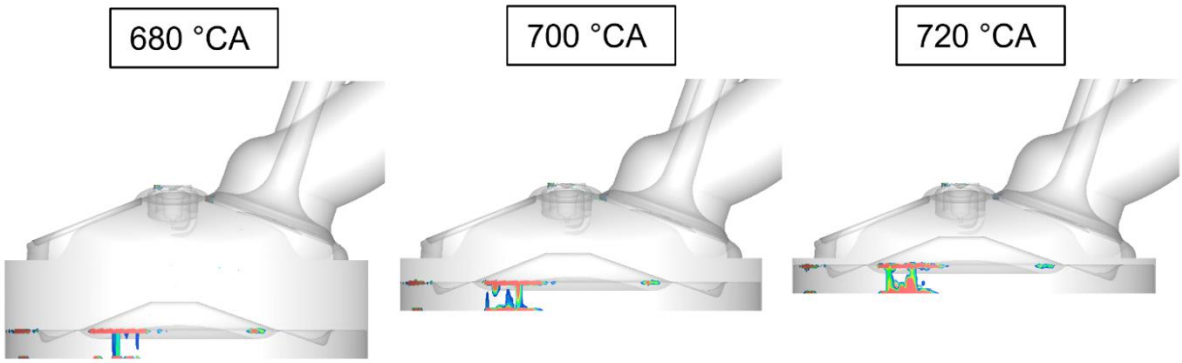

Figure 5-57: Film dynamic inside the piston crevice near TDC.

The circumstance that the piston and liner wetted areas are interacting may enforce the deposit formation process. The local reduction of the fluid viscosity due to oil/fuel-mixing inside the piston crevice may promote wetting on the piston top land. Additionally, the impingement of fuel droplets during fuel injection already cools down the piston surface, which reduces the heat transfer to the oil-fuel film. The fuel species in the fluid mixture can promote the initiation of pool fires, leading to incomplete combustion and deposit formation.

Mixture formation analysis

The appearance of surviving wall films until spark timing indicates incomplete mixture formation. Figure 5-58 shows the postprocessing result of the lambda and temperature distribution inside the combustion chamber.

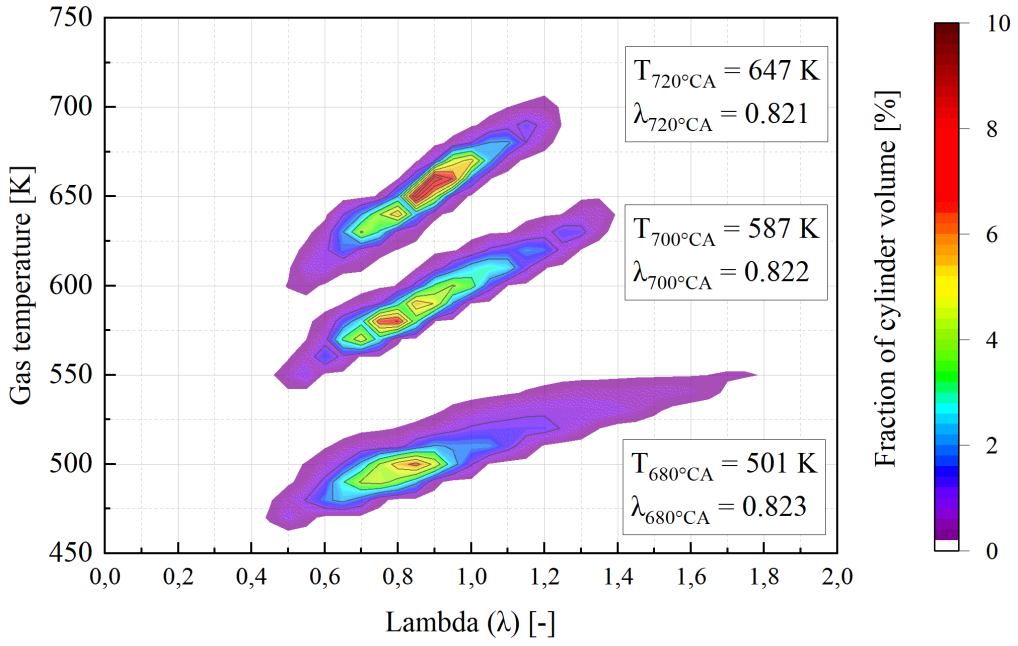

Figure 5-58: Scatter plot at 680 °CA, 700 °CA, and 720 °CA.

The scatter plot's color bar represents the volume fraction of the cylinder charge where the x- and y-axis values are fulfilled. The data is clipped at a minimum threshold of 0.2 %.

The figure displays the situation at 680 °CA, 700°CA, and TDC. In the shown timespan, the mean lambda value of 0.82 remains almost constant. Due to convective and diffusive transport, the relatively wide lambda distribution gets narrower towards TDC and ranges from 0.5 to 1.25.

The ongoing compression leads to an increase in the mean temperature level. As a result, the temperature difference between the walls and the gas phase increases, which results in the broader temperature band. Although, it has to be mentioned that the temperature bandwidth increases only by 25 K.

Furthermore, it can be observed that the displayed parameters are not entirely independent. Fuel-rich areas appear to be colder than lean regions. This is caused by the cooling effect of evaporating fuel droplets.

5.3.2 Droplet-induced ignition

5.3.2.1 Stochastic oil droplet release

In order to determine the ignition risk of a detached droplet in a detailed sub-model, the thermodynamic history of such droplets is needed. Therefore, the mixture preparation and wall film model were extended by a stochastic oil droplet release. The oil droplets were ejected at 72 points around the piston crevice with a diameter of 250 µm. This value represents a typical size of the piston crevice gap. The overall 360 released droplets were initialized with 1 m/s relative to the actual piston velocity and a spray cone angle of 90°. This slight increase compared to the piston speed was necessary because otherwise, the released droplets would get “caught” by the piston immediately after the injection.

The droplet release timing selection was based on the observations made during the mixture preparation and wall film formation simulation. Here, two possible events were identified which could lead to an oil droplet detachment. One possible event is at 630 °CA aTDCf, shown in Figure 5-59 (left). At this time, the piston wipes off the remaining fuel liquid film from the liner. The shear forces may induce perturbations which lead to droplet detachment. Additionally, the fuel mass mixed with the oil inside the piston crevice reduces the fluid viscosity and further promotes this effect. The second possible event is at 710 °CA aTDCf, shown in Figure 5-59 (right). At this time, the wall film models predict an upwards creeping trend of the liquid inside the piston crevice due to inertia forces.

These specific timings were chosen to simulate a stochastic oil droplet release. For every released oil droplet, the thermodynamic history was post-processed. Figure 5-60 shows the gas temperature and the oil vapor mass fraction in both simulated cases.

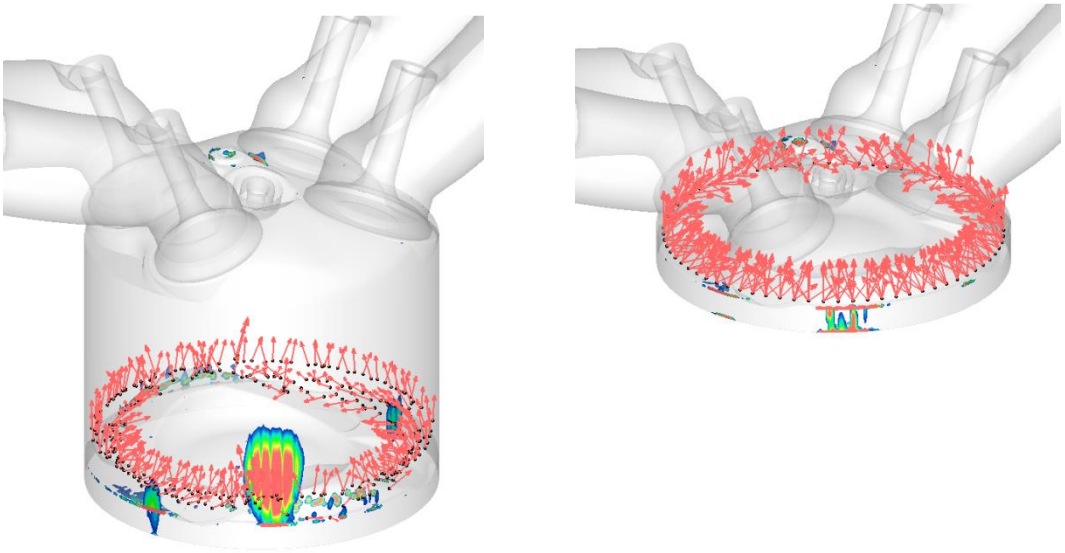

Figure 5-59: Stochastic droplet release at 630 °CA (left) and 710 °CA (right).

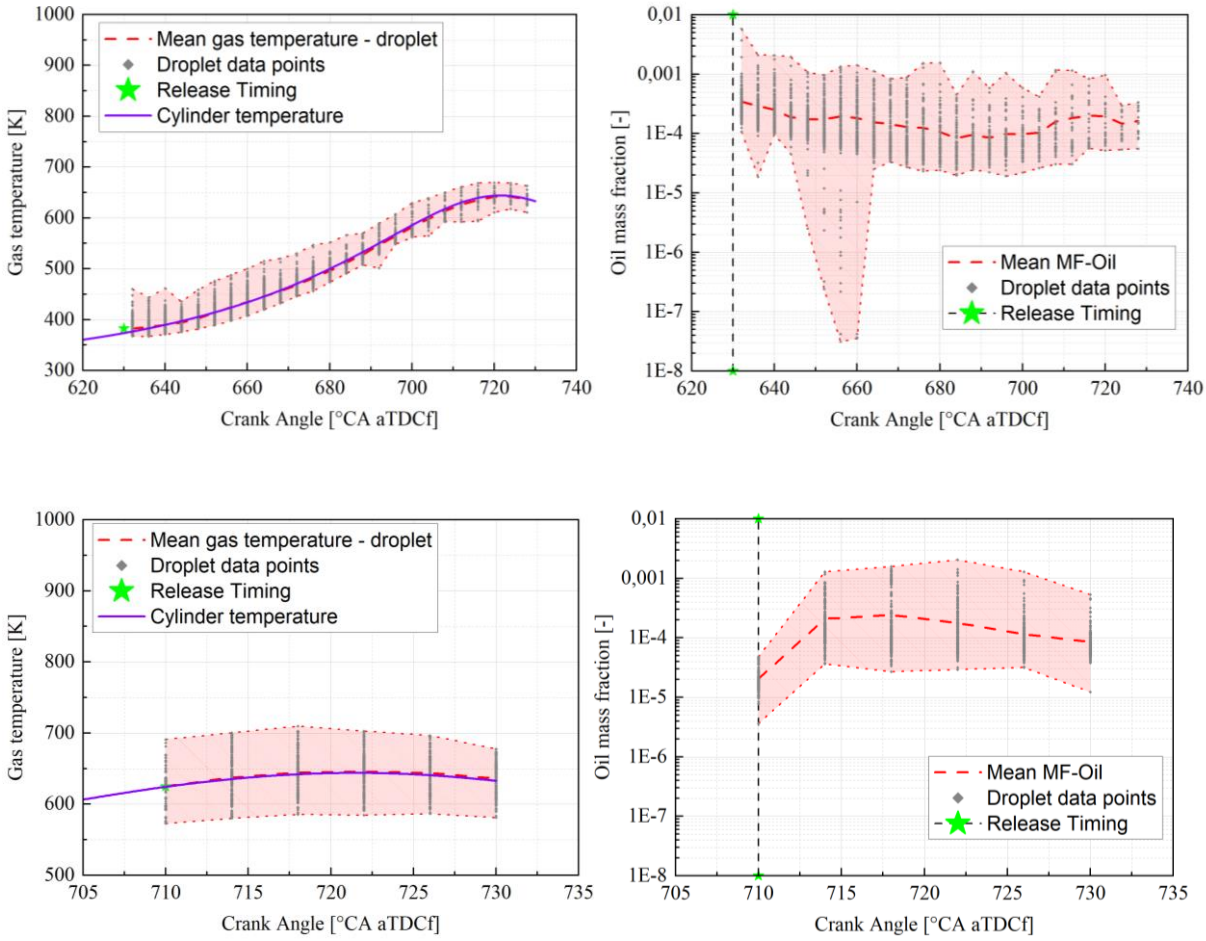

Figure 5-60: Gas temperature and oil vapor mass fraction histories.

The mean gas temperature in the vicinity of the oil droplet and the mean in-cylinder gas temperature are about the same. This indicates that the sample size (number of the released droplets) was high enough to get a good statistical representation of the possible in-cylinder pathways. Although, it has to be mentioned that the sample size constantly dropped during the simulation due to droplet-wall interactions.

Furthermore, it can be observed that the cooling effect of the evaporating droplet is almost neglectable compared to the convective heat transfer. The low vapor pressure of long-chained hydrocarbons leads to low evaporation rates. The observed maximum level of oil mass fraction in the droplet's vicinity is ~10^{-3} in both cases.

The observed temperature range is very similar to the global in-cylinder gas temperature distribution shown in chapter 5.1.1. Although, it can be observed that the late release timing simulation reaches higher maximum gas temperatures compared to the other simulation case.

5.3.2.2 Results of detailed droplet ignition simulation studies

Droplet ignition scenarios

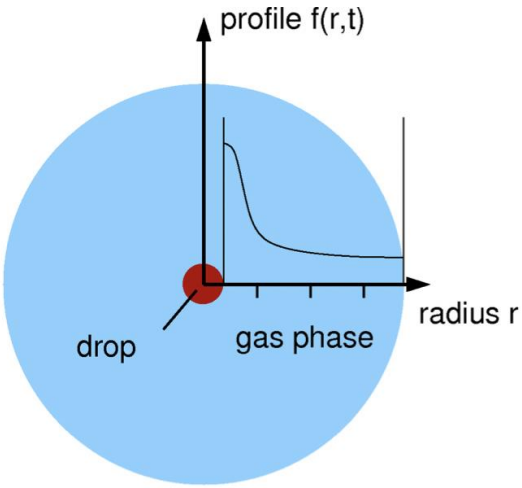

Figure 5-61 An (auto-ignition prone) droplet in a fuel/air ambiance.

Simulations are based on a model scenario in which droplets of a reactive substance (representing liquid oil or oil/fuel mixtures) are embedded into an ambient, less reactive fuel/air mixture (Figure 5-61). The situation is thus characterized by an auto-ignition-prone droplet versus the less auto-ignition-prone ambiance. The question to be answered is then under which conditions does the droplet affect auto-ignition and flame development in the ambient gas. This will depend on the physical conditions of the ambient gas, the droplet substance and on their chemical composition.

What happens at the droplet?

If we consider the droplet and ambiance first as separate entities, which are then brought into contact at time t=0, several events will occur and interact.

In engine conditions, the ambient temperature will usually be above the droplet temperature. Then, there is heat transfer between ambient gas and droplet. This will allow the droplet to evaporate, causing a flux of droplet-originating vapor from the droplet surface into the ambiance. The droplet vapor then mixes with ambient fuel/air; with increasing distance from the droplet surface, the droplet substance gets diluted with ambient gas. This mixing also affects the temperature field in the vicinity of the droplet.

In this inhomogeneous compositional and thermal field, chemical reactions can occur. In contrast to the often-used one-step representative chemical reaction step, in reality, there are multiple elementary reaction steps that occur in sequence or in parallel. This leads to the formation of radicals, chain branching.

While each of the individual elementary processes (heat transfer, evaporation, mixing, chemical reaction) is well understood, the coupled process becomes complicated by the overlap and interaction of these processes. It is probably not the elementary processes but their coupling that renders LSPI such a difficult-to-track problem.

Successful modeling of LSPI requires realistic treatment of phase change, molecular transport, chemical reaction, as well as their mutual interaction.

Processes during and after droplet ignition

Figure 5-62 shows a typical case of auto-ignition at a droplet by means of spatio-temporal profiles of temperature.

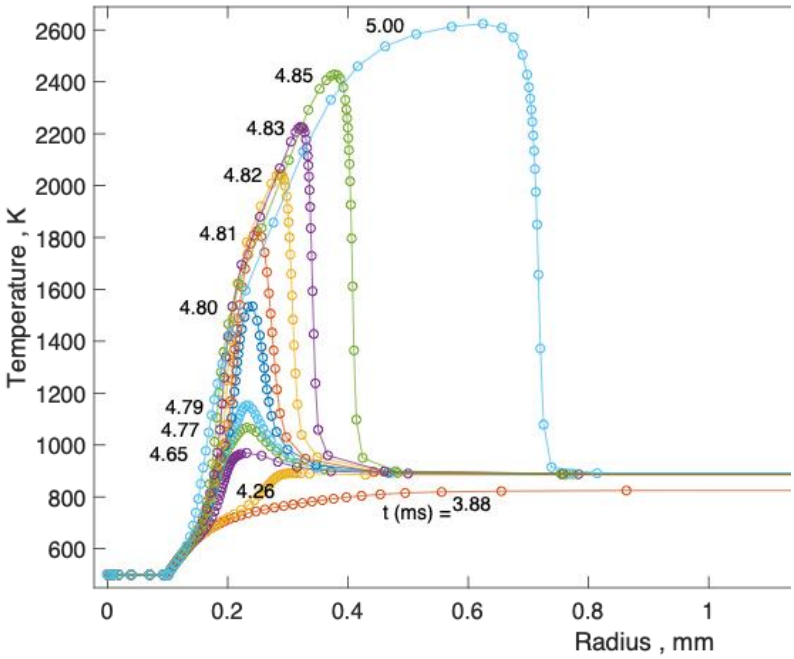

Figure 5-62 Temporal evolution of temperature profiles during the auto-ignition at a droplet with initial radius 0,1 mm. Numbers near the curves indicate the times (in milliseconds) after exposure of droplet to the gas phase.

At t = 0, the droplet gets exposed to ambient gas. The droplet begins to evaporate, and the released vapor diffuses into the ambient gas phase. The curve corresponding to t=3.88 ms corresponds to the mixing of ambient gas with the vapor released by the droplet. The temperature increases with increasing radius because the ambient gas has a higher temperature than the droplet. After some time, ignition occurs at some distance away from the droplet; this is visible first at the 4.26 ms and 4.65 ms curve. After ignition, a flame starts to spread; this is apparent by the expanding region of high temperature after about 4.85 ms in Figure 5-62. Unlike the example shown here, local ignition need not always lead to flame propagation. An important result is that the ignition can occur some distance away from the droplet. Also, ignition and flame propagation can be separated temporally from the existence of the droplet that has caused the vapor. As a consequence, despite the fact that causality between the vapor releasing droplet and the subsequent ignition/flame propagation clearly exists, there need not be clear observational evidence for this causality.

Droplet Ignition modeling studies

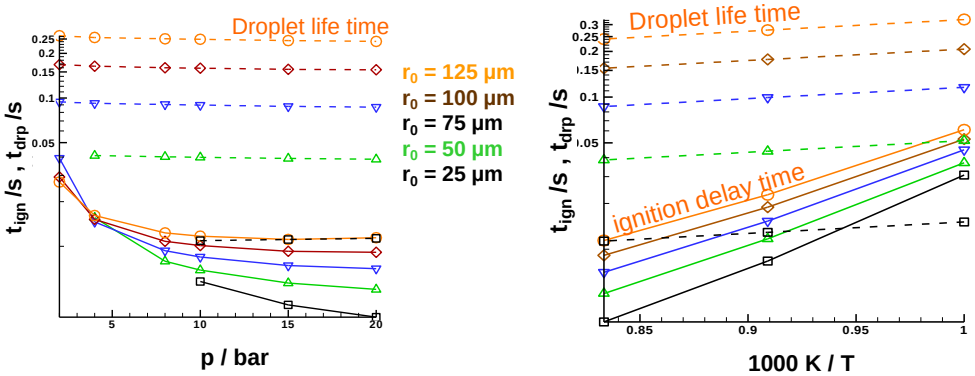

Figure 5-63 Excerpts from a droplet ignition „library“ , giving time scales of droplet life time and ignition delay as a function of gas phase temperature (right) and pressure (left).

A large parametric study of droplet ignition cases was performed. All are based on droplets embedded into an iso-octane air ambiance. Multiple simulations were run in a systematic approach to study the influence of several quantities: Gas-phase properties (temperature, pressure, equivalence ratio), droplet properties (initial droplet diameter, initial droplet temperature, droplet composition) on ignition delay times, evaporation rates and droplet lifetimes. Figure 5-63 gives an example of such a study; the extensive data allow to inspection the essential dependencies of the droplet-relevant time scales (droplet lifetime, ignition delay time, mixing times of droplet vapor and ambient gas) and their dependence on physical conditions like temperature, pressure. Importantly, analysis of the results can allow the identification of conditions where droplet ignition is sensitive or insensitive to the change of a parameter.

The results lead to multi-dimensional phase-space “maps” of these quantities. Figure 5-64 gives an illustrative example in the form a low-dimensional “cut-out” of the map for ignition delay time. The cut-out of the multidimensional map is along the sub-plane given by gas-phase temperature and equivalence ratio.

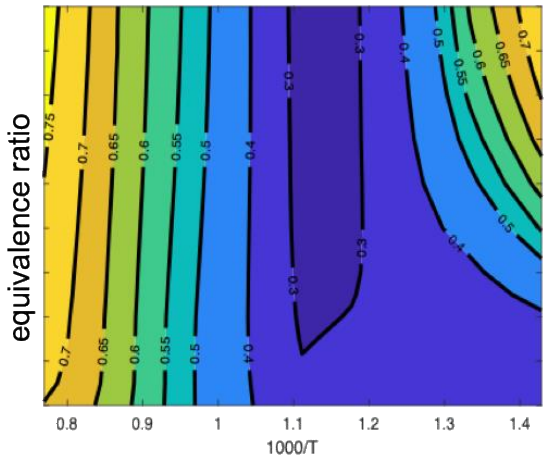

Figure 5-64 Low-dimensional “cut-out” of a map for ignition delay time.

As an important result of the analysis of the parametric ignition studies shows that for n-heptane droplets in iso-octane/air, LSPI-relevant ignition delay times were seen only at high gas temperatures (> 740 K).

Robustness of results with respect to kinetic data

The outcome of models will usually depend on the input data. For simulations of auto-ignition, values of the data for chemical kinetics are crucial. Notably, for each of the elementary reaction steps in a reaction mechanism, the values of the Arrhenius parameters describing the speed of chemical reactions can have a significant influence.

To study how strongly the data of an ignition depend on the kinetic parameters, these were “tuned” slightly, and simulations were repeated with the tuned reaction kinetics data to assess the change of ignition delay times with respect to the “unperturbed” data. The range of the tuning was chosen within the limits of the uncertainty of kinetic data.

Robustness of results with respect to oil composition

A possible source of uncertainty stems from the fact that droplet material might not consist exclusively of straight-chain hydrocarbons (of which n-heptane is a representative and which are among the fastest igniting hydrocarbons). As a plausible scenario, one may consider reacting components in the droplet, which display even faster ignition. A prominent class of such components are the Keto-hydroperoxides, a family of partially oxidized hydrocarbons. These substances might form from radical recombination reactions when hydrocarbons are exposed to the high-temperature environment of engines; Figure 5-65 gives a graphical rendition of the reaction paths that can lead to the formation of keto-hydroperoxides. Studies of droplets that were “doped” with different kinds of keto-hydroperoxides were performed to assess how the more reactive species would accelerate the ignition.

Figure 5-66 shows the result of such a study. Relative to the case of a pure n-heptane droplet at the same initial conditions, keto-hydroperoxides can accelerate the auto-ignition (and flame initiation).

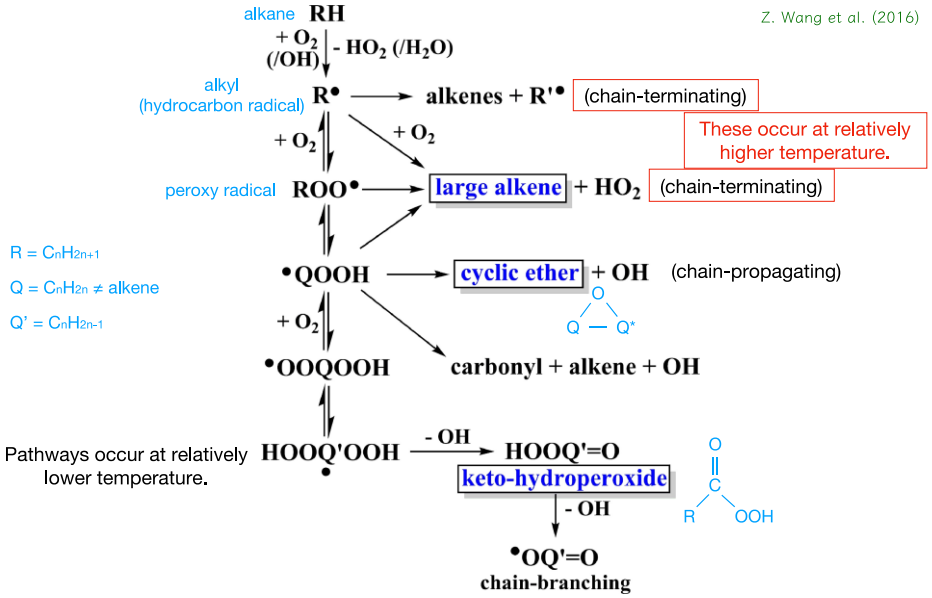

Figure 5-65 Reaction path for the formation of Keto-hydroperoxides from hydrocarbons, after Wang2016,[58].

However, even when acceleration by the presence of these reactive substances is considered, ignition delay times are too long to explain LSPI, if temperatures remain below about 740 K. At these temperature (at engine-relevant pressures), chemical kinetics is too slow.

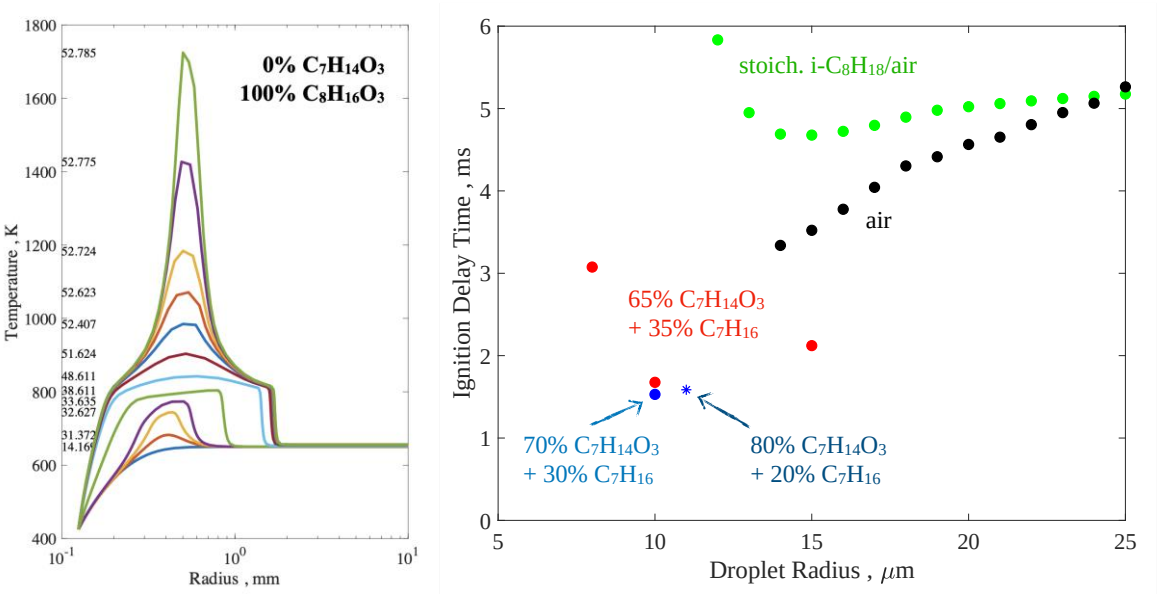

Figure 5-66 Left: Temperature profiles during auto-ignition of a keto-hydroperoxide enriched droplet. Right: Comparison of ignition delays for an n-heptane droplet embedded into atmospheres of different composition (pure air, stoichiometric iso-octane air, air with vapor of mixtures of different ketohydroperoxides).

The model studies, which assume a straight-chain hydrocarbon (n-heptane as a proxy) or keto-hydroperoxide (C7H14O3 and C8H14O3) in the droplet and iso-octane/air in the surrounding gas phase, predict long ignition delay times for these scenarios. Even if a pre-evaporation of the ketohydroperoxides, and thus an enrichment of ketohydroperoxides in the atmosphere

surrounding the droplet, is postulated, extensive ignition delay time studies (Figure 5-66) show that ignition delay times below 2 ms can be reached only for temperatures above 740 K.

With the studied conditions, faster ignition is possible only if the influence of additional, even more reactive substances is considered. Such substances, among them some that feature extremely large reactivities, may be formed by an operating engine, if not in a single cycle, then in a sequence of consecutive cycles where there is an accumulation of chemical progress. The pattern is that the “fresh” hydrocarbon forms radicals in one cycle, which recombine in “colder” regions of the combustion chamber, forming intermediate species. Some of them are potential “superfast” (in the sense of auto-ignition delay times) substances. They may survive a combustion cycle and also the gas-exchange phase, e.g., in cold crevices that are “protected” from the convective gas flow. Over several cycles, this can lead to an accumulation of highly reacting substances. The accumulated chemical progress can provide conditions that cause a sudden, violent self-ignition in one cycle, after an extended period (including a large number of cycles) of seemingly “dormant” chemical activity, as exemplified by the detailed chemistry simulation result shown in Figure 5-67.

Detailed treatment of this accumulated reaction progress is the subject of further studies; our simulations from an earlier research project already hinted at the plausibility of such a scenario.

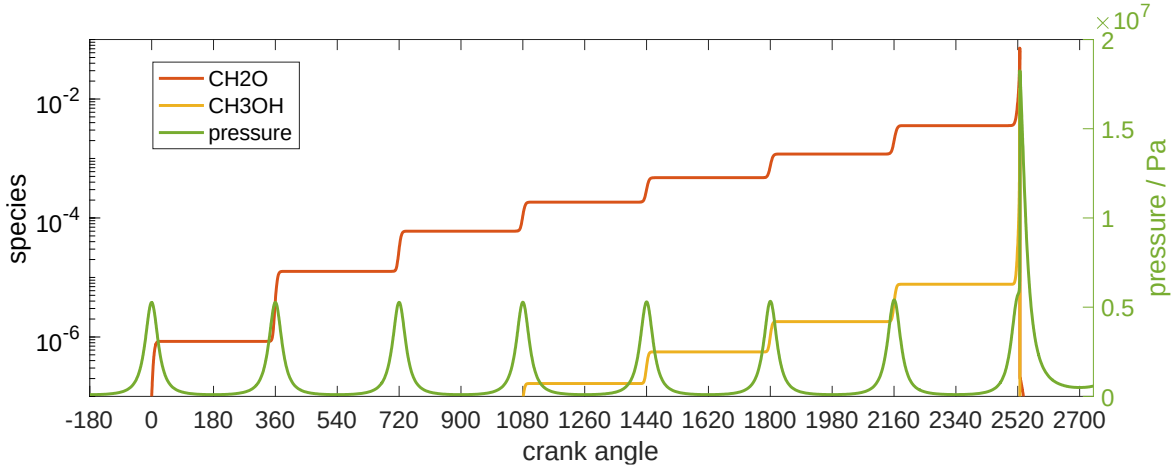

Figure 5-67 Example simulation showing the consecutive build-up of intermediate species from an initial hydrocarbon/air mixture between engine cycles. Only at the 8th compression, the formed intermediates lead to auto-ignition. Note the log scale of species: For most cycles, the amount is of intermediates is negligbly small; exponential growth „strikes“ at 8th cycle.

5.3.3 Hot particle-induced ignition

5.3.3.1 Ignition delay map

A set of pre-calculated cases was used to generate a look-up table to couple the results of the detailed hot-particle-induced ignition model with the CFD-engine model. By varying the gas temperature, gas pressure, lambda, and particle temperature, a 4D ignition delay map was generated. Table 5-2 shows the used parameter set.

Table 5-2: Parameter set of the pre-calculated cases.

Parameter	# Variations	Used values
Gas temperature	4	500 K, 575 K, 650 K, 725 K
Gas pressure	3	10 bar, 30 bar, 50 bar
Lambda – TRF	4	0.5, 0.8, 1.0, 1.2
Particle temperature	7	1000 K, 1200 K, 1300 K, 1400 K, 1500 K, 1600 K, 2000 K

The parameter range of the gas temperature, pressure, and relative air/fuel-ratio was chosen based on the performed CFD simulation of mixture preparation and wall film formation. In contrast, the particle temperatures were fairly unknown. Therefore, seven different particle temperatures were assumed to cover a wide range of conditions. As a result, 336 CFD cases were calculated and post-processed. Figure 5-68 shows an excerpt of the results.

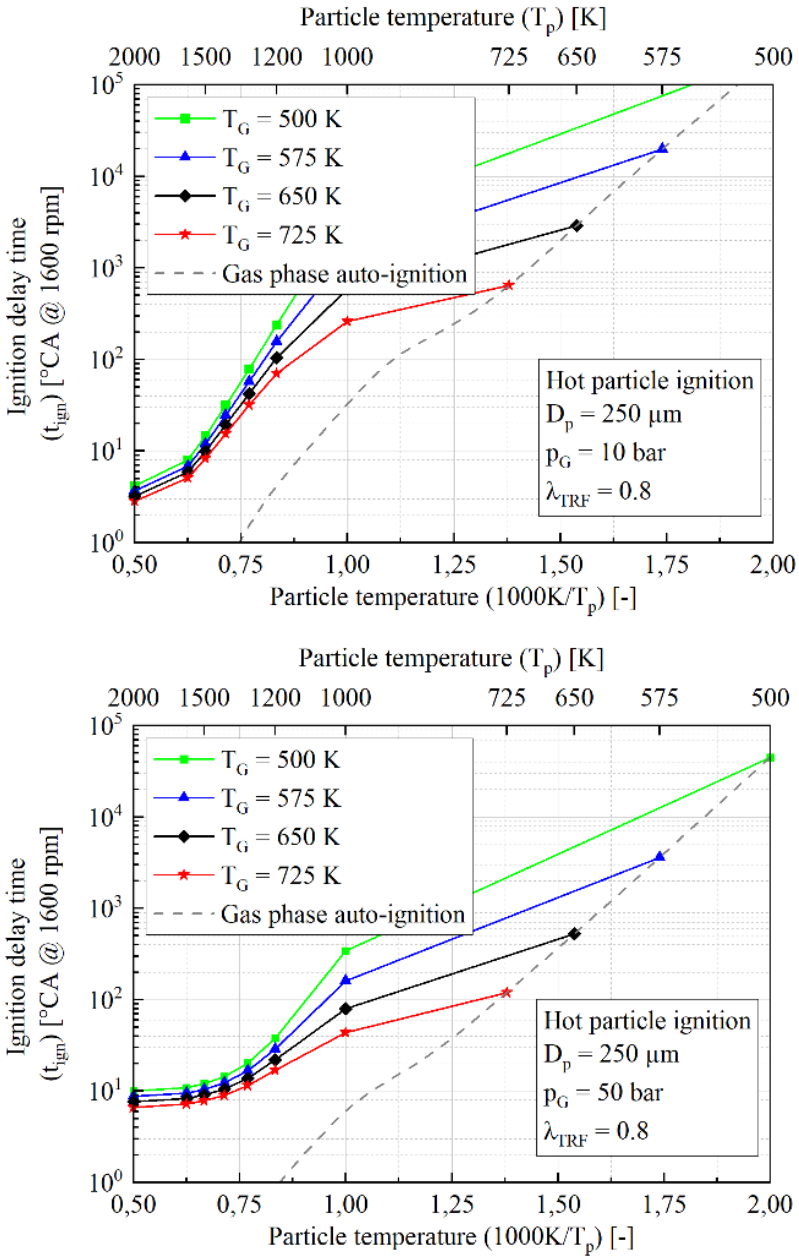

Figure 5-68: Gas and particle temperature variation at 10 bar (left) and 50 bar (right).

It can be observed that the ignition delay time converges towards 3~10 °CA for particles hotter than 1500 K. At 1500 K, an immediate ignition in the gas phase takes place that is almost independent of other parameters. The calculated ignition delay time is, as previously described, a result of the flame propagation.

For particle temperatures of 1000 K to 1400 K, a high gas pressure sensitivity can be observed. The ignition delay time gradient appears to be much higher at 10 bar compared to 50 bar.

Particles colder than 1000 K are most likely irrelevant for initiating an ignition under engine-relevant conditions. Even at a gas temperature of 725 K and a pressure of 50 bar, the calculated ignition delay time is longer than 30°CA.

The gas temperature dictates the overall reaction kinetic speed. Considering the ex-tended Arrhenius approach to calculate chemical reaction speed, it is not surprising that the gas

temperature significantly impacts the ignition delay time. Nevertheless, the overall reaction kinetic behavior does not change in the investigated temperature range.

5.3.3.2 Analytical investigation

An ignition integral was introduced to use the pre-calculated ignition delay map under transient conditions in the framework of a CFD simulation. The integral calculates the consumption of ignition delay time under the current thermodynamic conditions, see equation 3.

$$\tau_{ign} = \sum_{i=1}^{N} \left(\frac{\Delta t_{TS,\,i}}{\tau_{ign,\,i}\,(T_p,\,T_G,\,p_G,\,\lambda)} \right) \tag{3}$$

This method was used in analogy to the well-known Livengood-Wu knock integral. [61]

In order to investigate the influence of the particle temperature on the gas phase ignitability, a 0D-model was established. The model releases a particle at IVC and calculates the ignition integral under mean in-cylinder conditions until spark timing. Figure 5-69 and Figure 5-70 show the used boundary conditions and the temporal evolution of the results achieved.

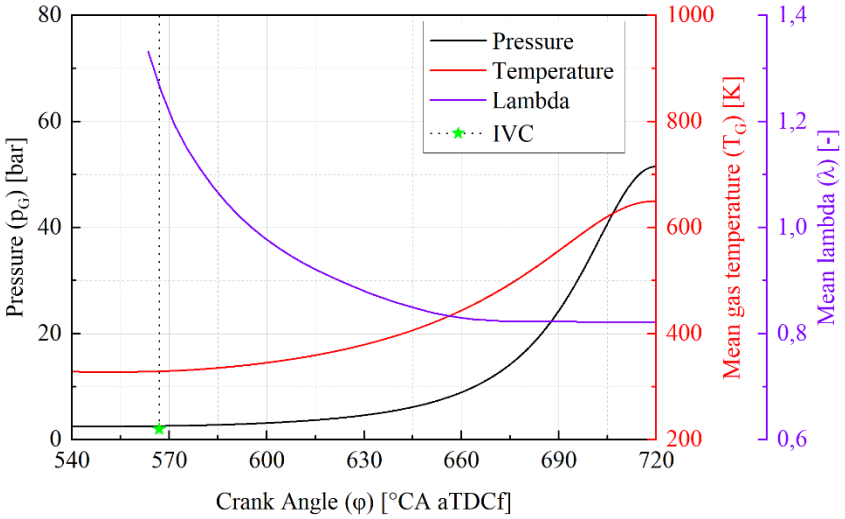

Figure 5-69: Mean thermodynamic in-cylinder boundary conditions.

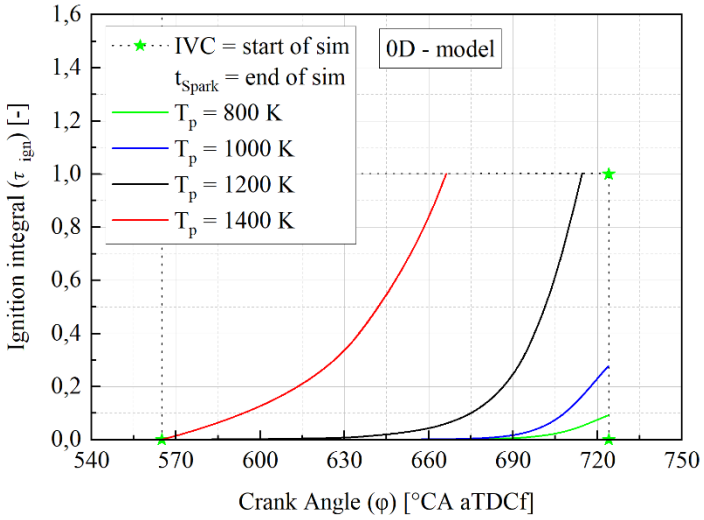

Figure 5-70: Particle temperature sensitivity on the ignition integral.

It can be observed that the ignition integral barely increases before 660 °CA. Before this time, the reactivity of the gas phase is very low due to the low pressure (< 10 bar) and gas temperature (< 450 K) levels. Only very hot particles (T_p > 1400K) are able to consume a significant amount of the ignition delay in the early phase of the compression. This effect reflects the decreasing sensitivity of thermodynamic boundary conditions of hot particles, shown in chapter 5.3.3.1.

By iterating the particle temperature, a minimum critical temperature of 1167 K can be found to induce an ignition at the end of the simulation (spark timing). This value holds true if the particle is released at IVC. Therefore, the start and end of the simulation were varied to investigate the sensitivity of the particle release and the ignition timing. The results are shown in Figure 5-71.

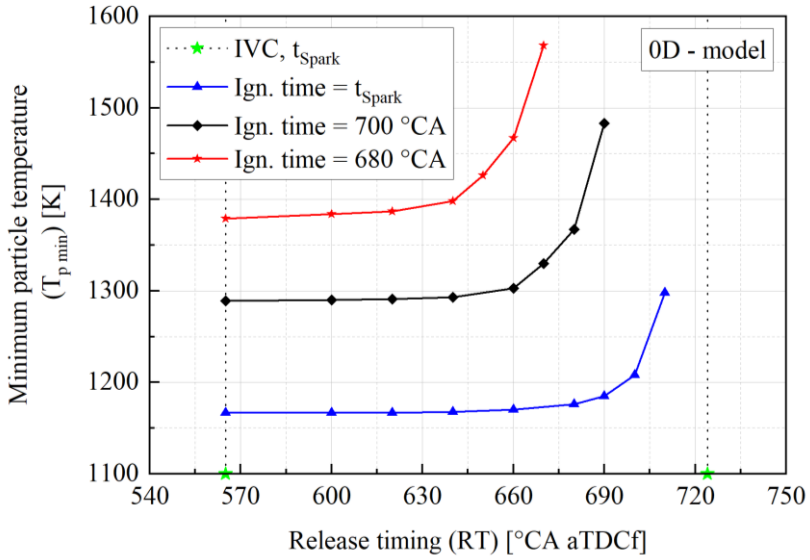

Figure 5-71: Release and ignition timing sensitivity.

The blue curve displays the results achieved by delaying the particle's release time while maintaining the previous ignition timing.

It clearly shows the minor impact of the early compression phase on the ignition timing. The critical particle temperature increases by 2 K when the release timing is shifted from IVC to 660°CA. On the other hand, an earlier ignition requirement at 700 °CA aTDCf increases the necessary particle temperature by > 100 K (black curve). With this requirement, the most reactive conditions of the compression phase are clipped away and high sensitivity to the defined ignition timing results.

5.3.3.3 The stochastic particle release model

In order to determine the ignition risk of a detached non-reactive particle, a stochastic particle release model is established. The history data obtained in the CFD simulation is used as an input to the 0D-ignition integral model shown in chapter 5.3.3.2.

The performed optical investigations suggested that detached particles can survive the gas exchange and may lead to a pre-ignition combustion in a follow-up cycle. Therefore, the CFD-engine model had to be able to simulate multiple engine cycles, including combustion. In order to model the expected partially premixed combustion conditions, the well-known G-equation approach was chosen. The calculation of the flame speed was performed using the correlation of Gülder. [62] The spark ignition was modeled by a numerical local heat release, including a ramp-up function.

A simple 1-component surrogate substituted the previously implemented detailed 11-component fuel model to avoid excessive calculation runtimes. Besides the heat of evaporation and the liquid density, the thermodynamic data of iso-octane was used. Both mentioned

parameters were set to the mean value of the unevaporated 11-component surrogate model to minimize the influence on the established spray model. Furthermore, the lower heating value was set according to the supplied fuel specification. Figure 5-72 shows the achieved high-pressure trace using the de-scribed model setup.

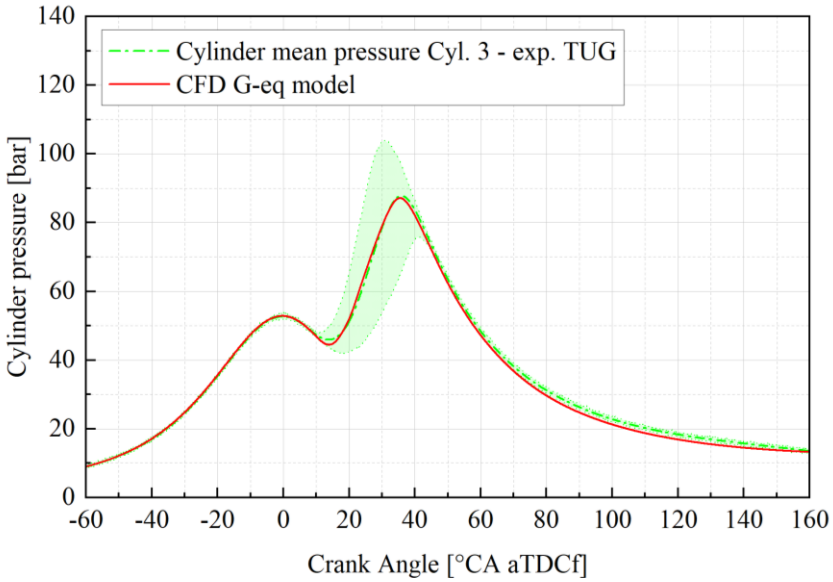

Figure 5-72: Measured vs. simulated in-cylinder pressure trace.

The released particles had to be parameterized according to the properties of solid deposits. The optical investigations showed that particle detachments occur favorably at locations where fuel wall-wetting is observed. Therefore, it can be derived that deposits are generated by incomplete combustion processes of fuel-oil mixtures. As a result, the created solids will have a carbon-based structure similar to soot or coal. This hypothesis is also confirmed by the chemical characterization analysis of scraped-off deposits.

The size of the detached particles could not be accurately measured with the used optical setup. Therefore, particle diameters ranging from 100 µm to 500 µm were initialized at fuel-wetted piston crevice locations. The lower end of the diameter spectrum represents the limit of optical visibility (resolution), and the upper end is twice the piston crevice width.

The definition of the particle release timing was set to the earliest observed detachment during the experiments to cover the most critical condition during the initial cycle. The initial particle speed is defined randomly between 1 m/s and the maximum observed initial speed.

The particles' initial temperature is assumed to be 462.5 K. This represents the average temperature of the cylinder liner and the piston surface used in the CFD simulation.

In order to get a sufficient statistical representation of the particle properties, a total amount of 10.000 particles were initialized. Table 5-3 summarizes the parameters used in the simulation, and Figure 5-73 the particle temperature history of all released particles during two engine cycles.

Table 5-3: Summary of particle properties.

Parameter	Unit	Used value	Reference
Initial Speed	m/s	1 – 7.5	Optical observation
Initial particle temperature	K	462.5	Assumption (avg piston/Liner)
Diameter classes	µm	100, 200, 300, 400, 500	Engine geometry and optical resolution
Released particle count	#	10.000 (2.000 each diameter class)	
Thermal mass $(\rho * c_p)$	kJ/m³K	1000	[63]
Density	Kg/m³	1800	[23, 64]
Conductivity	W/mK	1.06	[63]

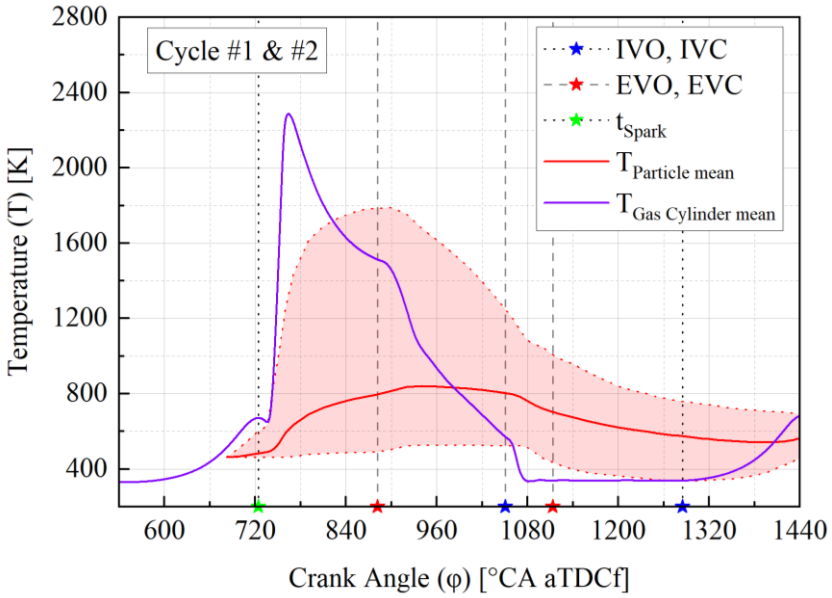

Figure 5-73: Particle temperature history considering engine cycle #1 and #2.

The solid red line represents the mean particle temperature. Additionally, the minimum and maximum values of the particle temperatures are shown. It can be noticed that the mean particle temperature does not increase significantly during the initial cycle (#1). However, the smallest particles are able to increase their temperature up to ~600 K. Therefore, it is not possible to initiate a pre-ignition for non-reactive particles, which was the assumption for this approach.

Concerning the follow-up cycle, the particles are heated up during the combustion phase. The hottest particles reach a temperature of ~1200 K at IVO. The fresh intake air cools down the particles again. Therefore, the maximum particle temperature is decreased during the following compression phase and falls below 800 K. The temperatures of all particles in the simulation are too low to initiate a pre-ignition.

This leads to the conclusion that particles that are able to initiate a pre-ignition in the follow-up cycle and especially in the initial cycle have to be reactive. Otherwise, the surface temperatures will not be sufficient. The rate of heat release (reactivity) of such detached particles is currently unknown. Especially, the influence of inorganic residues from oil additives (Ca, Mg, Zn, Mo,…) is assumed to have a significant impact. [65]

Therefore, a “reverse engineering” approach was chosen. Instead of trying to model the reactivity of the particle itself, the minimum necessary particle temperature to enable a pre-ignition

was further investigated. A particle was assumed to be reactive if the particle temperature surpassed a critical light-off temperature of 900 K. Simultaneously, the ambient gas phase's oxygen mass fraction level has to be greater than 9 %. These thresholds were chosen conservatively based upon available literature data for soot. [65, 66] If a particle surpassed these thresholds, the temperature was instantly increased to a constant “reactive” temperature.

Considering the initial cycle, none of the released particles fulfilled the particle temperature requirement. This result directly relates to the chosen initial particle temperature. It is assumed that the temperature of the deposits is controlled by the cooled in-cylinder wall temperatures. The gas-phase never exceeds the light-off temperature during the compression. Therefore, released particles must have an initial temperature above the light-off temperature to induce a pre-ignition. This is conceivable when assuming particles as residuals of liquid films that were not fully consumed during combustion. Anyway, due to the lack of quantitative data, this was not further pursued.

The particles are heated up during the combustion and expansion phase, which is relevant for the follow-up cycle. Figure 5-74 shows the temporal evolution of the particle temperature and oxygen mass fraction inside the combustion chamber from IVO to TDC of the second cycle. After IVO, the oxygen mass fraction rises rapidly due to the high boost pressure level. This steep increase enables some particularly hot particles to fulfill the requirements described above. Figure 5-75 shows the analysis of the particle count of each diameter class surviving the gas exchange and being able to satisfy the reactivity limits.

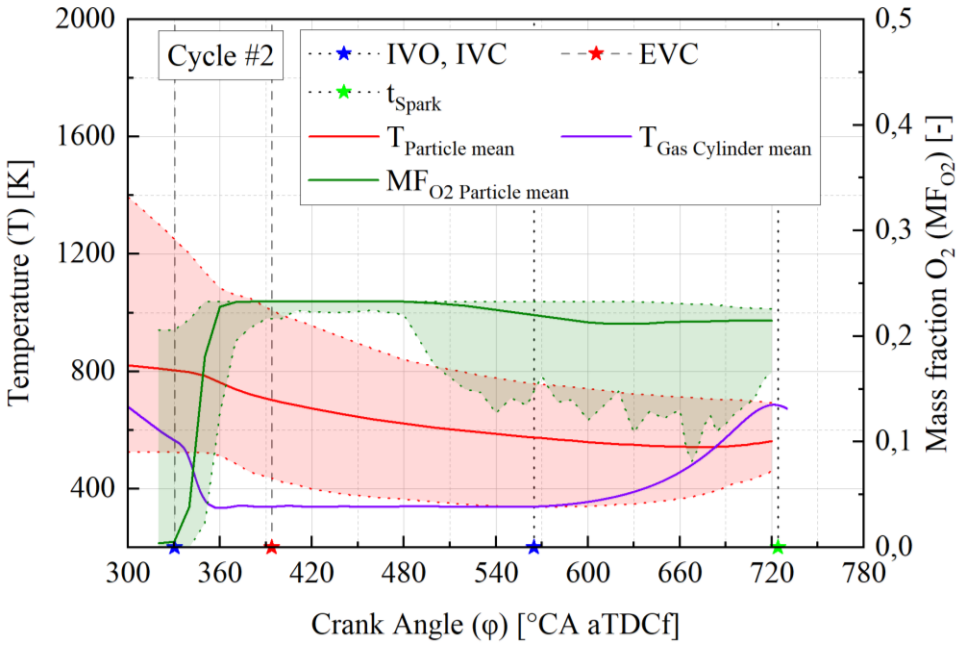

Figure 5-74: Particle temperature and O2 mass fraction - cycle #2.

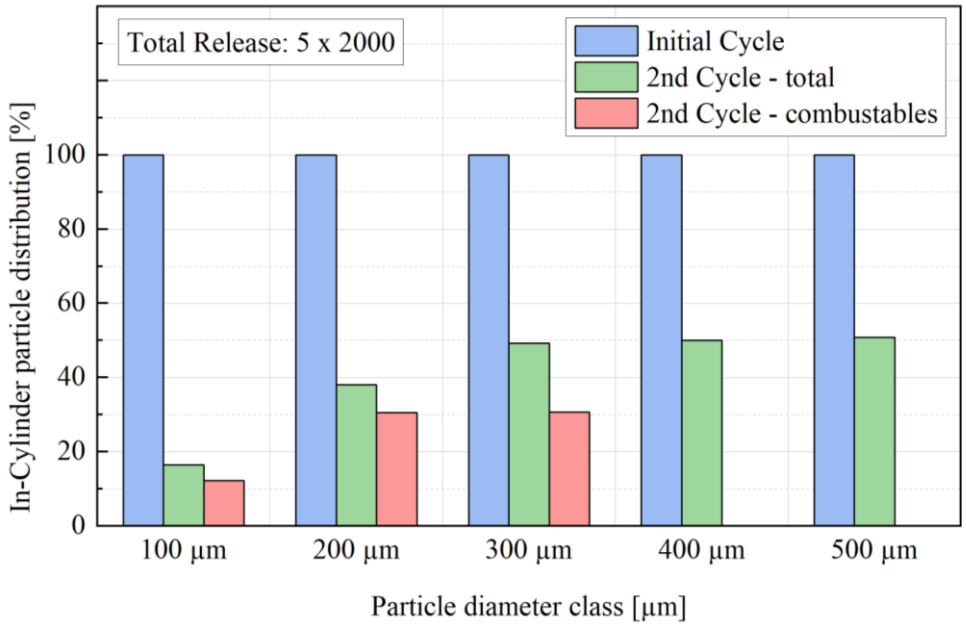

Figure 5-75: Histogram of surviving and reactive particles.

It can be observed that only particles smaller than 400 µm are able to reach a sufficiently high temperature. On the other hand, smaller particles are more likely to get flushed out during the gas exchange. This trade-off leads to a sweet spot at particle diameters of 200 µm ~ 300 µm.

The ignition delay consumption could be calculated by postprocessing and exporting the particle histories of all combustible particles during the second cycle. Figure 5-76 shows the result for a constant reactive temperature of 1200 K. Additionally, the thermodynamic conditions during the compression phase are shown in Figure 5-77.

The most critical pathway leads to a predicted ignition at 707 °CA aTDCf. Besides the most critical one, the results of the top 10 critical particles deviate about 1~2 °CA. Looking into the thermodynamic history of these top 10 particles, one can see that the particle pathways differed significantly during the early phase of the compression, whereas the deviation got smaller towards TDC. Overall, it can be observed that the most critical pathways were near the mean in-cylinder conditions. Although, a slight shift towards cooler and fuel-rich regions can be noticed.

The results showed that small particles with high mobility inside the combustion chamber are more likely to find these conditions. Concerning the diameter classes, 100 µm and 200 µm particles appeared to be the most critical ones.

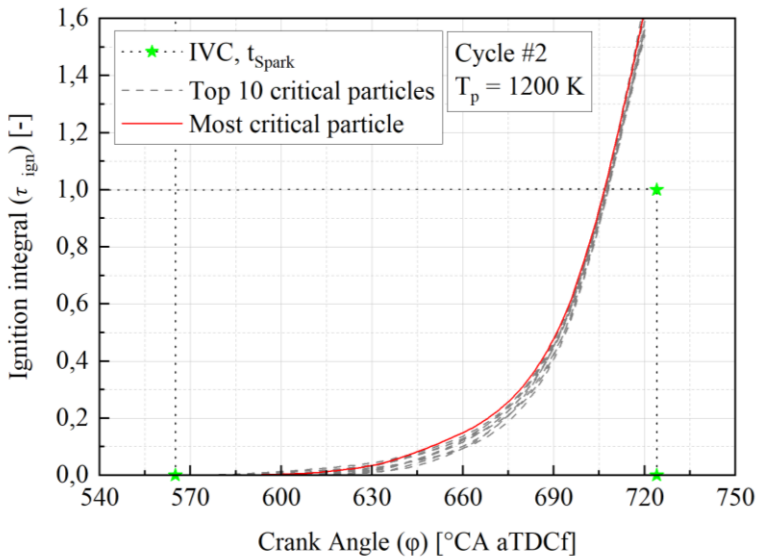

Figure 5-76: Evolution of the ignition integral of the top 10 critical particles.

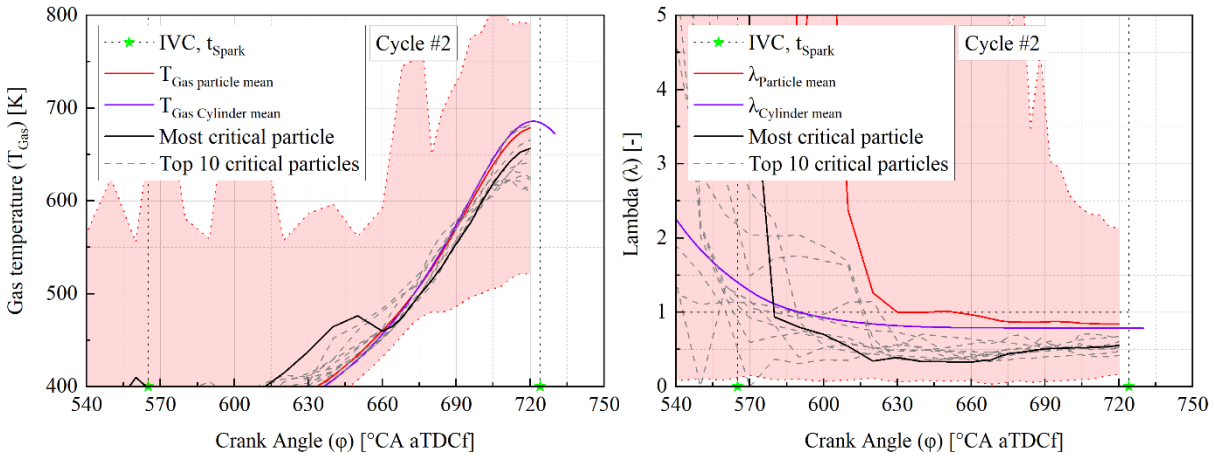

Figure 5-77: Thermodynamic history of the top 10 critical particle pathways.

6 Summary and conclusions

The overarching research goal of the project lies in explaining the fundamental mechanism, which leads to an initial pre-ignition with highly turbocharged petrol engines. Experimental investigations as well as accompanying numerical studies are performed to get a deeper insight into the stochastic nature of this irregular combustion phenomenon.

As a first step, a thermodynamic pre-ignition characterization was carried out to identify pre-ignition critical engine operation modes. The parameter variations showed a strong dependence on pre-ignition on the quality of the mixture preparation. The number LSPI increased with parameter settings, leading to a poor mixture preparation or an interaction between the injection spray and the liner. Additionally, the influence of the supplied fuel and lubricating oil was investigated. During the investigations with standard fuel Ron 95, fewer pre-ignitions could be observed compared to the Coryton high LSPI fuel. Also, the Fuchs 5W-30 oil showed an increased LSPI tendency due to a higher amount of additives, especially calcium.

The injection tests showed that a specific amount of oil transported into the combustion chamber leads to pre-ignitions. The injection key experiment also showed that the injected oil didn't react immediately after entering the combustion chamber. Always an accumulation time goes by until a pre-ignition occurred.

The thermodynamic investigations suggest that the parameters influencing the quality of mixture formation and the used lubricating oil have a significant impact on the pre-ignition frequency. In order to deepen the basic understanding of the mechanism, an optical pre-ignition characterization is performed.

The optical pre-ignition characterization revealed that the ignition initiation was caused either by glowing objects moving inside the combustion chamber or, in rarer cases, by light-emitting deposits on the in-cylinder walls. These flying objects are most likely solid substances since rebounds from the intake valve could be observed. The appearance of differences in glowing intensity and the observation of glowing particles during the intake stroke indicates a chemical reactivity. Additionally, a dynamic deposit formation behavior was observed, especially in regions of pronounced fuel spray/ liner interaction. This suggests a correlation between liquid film formation and pre-ignition frequency. As a result, the optical investigations extended the knowledge gained in the thermodynamic characterization process. Further on, there was no evidence of a droplet-induced pre-ignition.

Additional key experiments are performed to get further insight into the initiation mechanism. The modification to the CNG operation confirmed the influence of the spray/ wall interaction. No PI events could be detected while operating on gaseous fuel. By using a light-induced fuel fluorescence tracking method, the areas of deposit formation can be correlated with fuel wall-wetted regions. No droplet ignitions could be observed. The introduction of lubricating oil into the manifold could not trigger a droplet-induced PI. Although, a multi-cycle deposit formation process was observed. In the following, these deposits initiated the pre-ignition. The occurrence of glowing particles during the expansion phase and the air-fuel-ratio influence confirms the assumption of reactive particles. The increased partial pressure of oxygen enhances the particle's reactivity.

Finally, inorganic substances coming from lubricating oil additives on the reactivity of deposits are analyzed using a chemical characterization. Deposits formed from lubricating oil showed a higher reactivity compared to deposits formed from gasoline.

Besides the testbed measurements, comprehensive numerical studies are performed. The goal of the simulations is to verify the observations made during the experimental investigations. Therefore, an in-depth analysis of the possibility of oil droplets and particle-induced pre-ignition is performed. Further on, the influence of the spray/ wall interaction and mixture formation process is analyzed.

As a first step, the thermodynamic conditions inside the combustion chamber, as well as the mixture formation process, are investigated. Therefore, a CFD-engine model was generated

and validated against measurement data. Special focus was placed on applying a detailed fuel surrogate model to predict film formation on the hot combustion chamber walls accurately. Consequently, an 11-component fuel surrogate was established using a 0D-distillation model. The vapor pressure was corrected by calculated activity coefficients (UNIFAC method) to account for mixture effects. The investigation of the “ISO-operation point” showed four distinct regions where pronounced fuel wall wetting could be observed. The heat transfer from the in-cylinder walls to the liquid film was insufficient to evaporate the fuel film until TDC. The fuel-wetted locations correlated with the optical observations. As a result, pool firing events could be detected, which enhanced deposit formation due to incomplete combustion.

To determine the ignition probability of detached oil droplets in a detailed sub-model, the knowledge of the thermodynamic history of a released oil droplet is necessary. Therefore, the CFD-engine model was extended by a stochastic oil droplet release from the piston crevice. The 250 µm droplets were modeled with a 4-component surrogate oil. The selection of the four species was based on a GC-analysis. Two release timings were simulated. The first simulation initialized oil droplets at 630 °CA aTDCf. At this time, the piston starts to wipe-off the fuel film from the liner. The induced shear forces are a possible source of droplet detachment. During a second simulation, oil droplets were released at 710 °CA aTDCf. The deceleration of the piston towards TDC forces the accumulated liquid in the piston crevice to flow up toward the piston top land what indicates the possibility of a detachment. By postprocessing the thermodynamic history along the trajectories of all released oil droplets, it could be shown that the average gas temperature around the droplets is almost the same as the mean gas-phase temperature inside the combustion chamber. The low vapor pressures of the long-chained hydrocarbon species led to a low evaporation mass flux and, as a result, to a minor cooling effect. The most critical droplets experienced a maximum gas temperature of ~700 K and built up an oil mass fraction of 10-3.

Based on the calculated transient boundary conditions, the droplet ignition process was calculated in a detailed sub-model. The ignition studies show that for the putative scenario of hydrocarbon droplets embedded into a hydrocarbon air ambiance, temperatures exceeding 740 K are required to allow auto-ignition within the time scales relevant for an engine. This result also holds true if the droplet substance is a ketohydroperoxide ($C_8H_{16}O_3$ or $C_7H_{14}O_3$).

An interpretation of this finding can be given as follows: If the temperature in practical engines remains essentially below the 740 K level, the conclusion is that the studied droplet-ignition scenarios cannot explain the observed LSPI phenomenon.

In order to determine the ignition risk of detached solid particles numerically, a detailed sub-model was established to pre-calculate the ignition delay times under constant boundary conditions. Based on these results, a 0D-model was created, which uses an ignition-integral approach to transfer the static results to transient ambient conditions. By supplying mean engine conditions, a minimum particle temperature of 1167 K was calculated to initiate an ignition at spark timing. This value holds true if the particle is released at IVC and remains at that temperature level until spark timing. The requirement of ignition timing at 700 °CA aTDCf increases the minimum temperature to ~1300 K, whereas a release timing shift to 660°CA aTDCf has only a minor effect. Since the thermodynamic conditions inside the combustion chamber are inhomogeneous to some extent, a stochastic particle release model was established to capture statistical particle histories. The initialization of the particles was based upon optical observations at the testbed. It could be observed that the particle detachment is favorably at locations where fuel wall-wetting occurs.

It could be shown that non-reactive particles with a diameter ranging from 100 µm to 500 µm are not able to initiate a pre-ignition combustion within two consecutive engine cycles. This result was achieved using thermodynamic properties according to literature data of soot and coal. This leads to the conclusion that particles that are able to initiate a pre-ignition in the follow-up cycle and especially in the initial cycle have to be reactive. Otherwise, the surface temperatures will not be sufficient. As a result, the numeric simulations verify the need for reactive objects to trigger a pre-ignition found in the experiments.

As a conclusion of all the knowledge and observations gained, the pre-ignition mechanism shown in Figure 6-1 is synthesized. There was no experimental or numerical evidence of oil droplet-induced pre-ignition. All optically detected pre-ignitions show a light-emitting surface deposit or particle history. The optical and numerical results and reactivity comparison of different specific deposits and their pre-ignition correlation show that pre-ignition-initiating objects must be products of reactive deposits. Inorganic residues caused by oil additives increase the reactivity of such deposits.

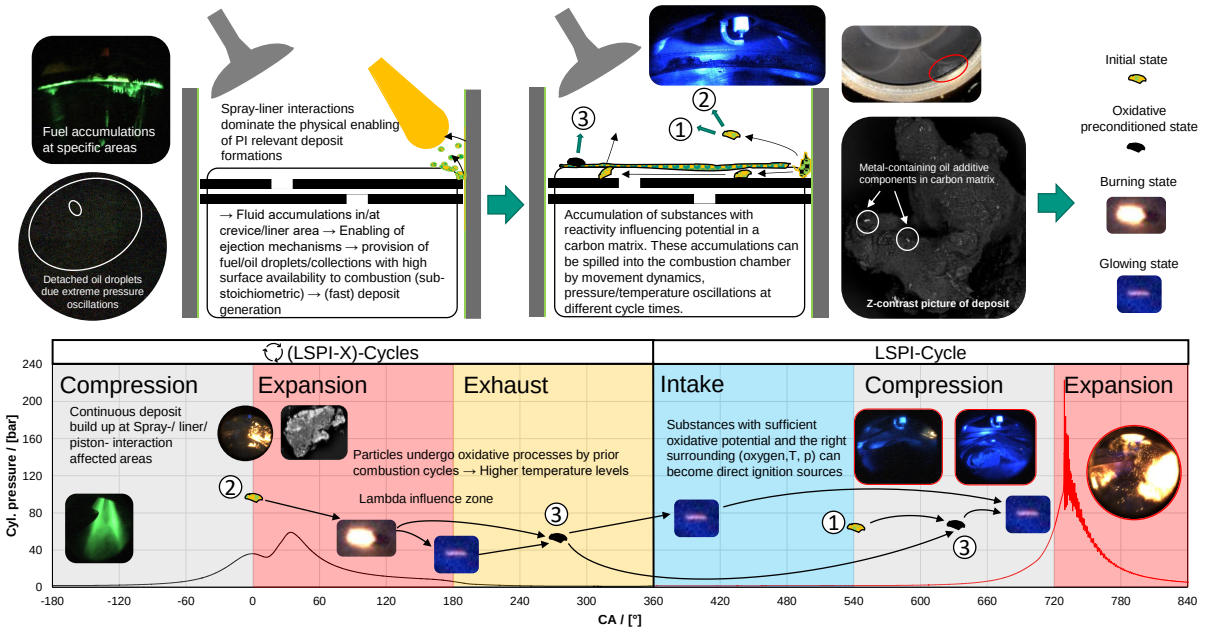

Figure 6-1: Derived pre-ignition mechanism.

The pre-ignition mechanism at hand is a complex multi-cyclic process with "physical enabling mechanisms" as a starting point. These are the initial processes that enable the subsequent formation of deposits of substances with reaction influence potential. Here, the spray/ liner interaction (oil film) is the dominant influencing factor. In particular, this enables under-stoichiometric oil combustion and thus creates the potential for reaction-influencing inorganic residues from oil additives to be deposited at piston crevice regions. Responsible for this can be liquid ejection processes or creep processes from the piston crevice due to an increased accumulation of liquid and thus a change in surface tension and viscoelastic properties.
The subsequent iterative formation process of reactive deposits (deposit detachment by pre-ignition events) created a further basis for the following pre-ignition initiations. For an efficient deposition of inorganic reaction-influencing substances from the oil additives, additional carbon deposition structures are necessary as carriers. These are formed by general sub-stoichiometric combustion of fuel and oil (pool fire areas). The fuel piston wetting point of the "ISO load point" at the piston top near the crevice area showed the highest density of reaction-influencing substances.
In the next step, these accumulations can be spilled into the combustion chamber by movement dynamics, pressure/ temperature oscillations at different cycle times. In the special case, reactive deposits placed on the piston crown and the associated good oxygen availability as well as the possibility of a temperature increase through continuous exposure to combustion, local surface pre-ignition initiations can occur (**3**). In the case of released highly reactive particles, a sufficient temperature increase with simultaneous oxygen availability can lead to pre-ignition initiation (**1**). The extent to which thermal and oxidative preconditioning is necessary, which may enable this pathway in the first place, can only be conclusively clarified with complete knowledge of the deposit composition and the associated reactivity kinetics. Occurrences of series pre-ignition events could also correspond to this path.
A further initiation path (**2**) runs via the (necessary) participation of a reactive deposit particle in regular combustion cycles before pre-ignition. Hereby thermal and oxidative preconditioning

can take place. This path thus shows a correlation between the air-fuel ratio and the probability of pre-ignition. It can also explain the often observed, intermittent subsequent pre-ignition behavior. We conclude a multi-cyclic "oil additive dominated" deposit-driven pre-ignition mechanism.
The outlined pre-ignition mechanism makes the stochastic nature of pre-ignition events comprehensible. The influence mechanisms of known "pre-ignition influencers" can also be explained. In the next step towards a complete understanding of the mechanism, the sub-mechanisms (physical enabling mechanisms, deposit building process, deposit chemistry) need to be precisely explored.

Outlook

All experimental and simulative investigations have shown that direct oil droplet ignition in the gas phase is very unlikely under the given boundary conditions. All observed pre-ignitions could be associated with air/fuel mixture ignition on highly reactive deposits and/or particles. A multi-cyclic "oil additive dominated"-deposit-driven pre-ignition mechanism is evident. The accumulation of oil and fuel (spray/ liner interaction) and their passage through multi-cyclic combustion processes leads to the accumulation of highly reactive deposits. These, in turn, can initiate pre-ignition under the right environmental conditions. Three relevant sub-mechanisms and their specific issues with the need for further investigations could be identified. As an initial condition, the so-called physical enabling mechanism for the relevant reactive deposit formation could be mentioned. Knowledge of the liquid behavior in the piston top land can help to gain new insights. What is the amount and composition of liquid accumulations in the piston crevice over time? How do droplets get detached or ejected and which influence does liquid film formation on piston have? What are the exact starting conditions for deposit formation? In the next step, the deposit formation process must be investigated in more detail. What is the influence of liquid mass and composition in top land on deposit formation and deposit composition? How are reactivity influencing substances deposited and build-up? The last sub-step involves the detailed investigation of the ignition mechanisms and the closely related particle/deposit reactivity. A detailed chemical kinetic description is needed. Through further in-depth investigations of these key points, a complete mechanism understanding can be obtained, and thus efficient countermeasures can be initiated. Only through a complete understanding of all underlying mechanisms, maximum system efficiency and power output of future gasoline engines can be achieved.

7 Appendix

7.1 Bibliography

[1] Palaveev, S.; Magar, M.; Disch, Ch.; Schießl, R.; Kubach, H. et al: Simulations and Experimental Investigations of Intermittent Pre-Ignition Series in a Turbocharged DISI-Engine. 4. IAV Tagung „Ottomotorisches Klopfen – Irreguläre Verbrennung“, 9-10. Dez. 2013, Berlin.

[2] Kuboyama, T.; Moriyoshi, Y.; Morikawa, K.: Visualization and Analysis of LSPI Mechanism Caused by Oil Droplet, Particle and Deposit in Highly Boosted SI Combustion in Low Speed Range. SAE Int. J. Engines 8 (2), 2015, S. 529–537,doi: 10.4271/2015-01-0761.

[3] Han, L.; Zhu, T.; Qiao, H.; Zhang, D. et al., Investigation of Low-Speed Pre-Ignition in Boosted Spark Ignition Engine. SAE Technical Paper 2015-01-0751, 2015, doi:10.4271/2015-01-0751.

[4] Döhler A. et al : A contribution to better understanding the pre-ignition phenomenon in highly charged internal combustion engines with direct fuel injection. 4th International Conference on Knocking in Gasoline Engines (Berlin), pp.41-61 (2013).

[5] Okada, Y., Miyashita, S., Izumi, Y., and Hayakawa, Y.: Study of Low-Speed Pre-Ignition in Boosted Spark Ignition Engine. SAE Int. J. Engines 7(2):584-594, 2014, doi:10.4271/2014-01-1218.

[6] Moriyoshi, Y., Yamada, T., Tsunoda, D., Xie, M. et al.: Numerical Simulation to Understand the Cause and Sequence of LSPI Phenomena and Suggestion of CaO Mechanism in Highly Boosted SI Combustion in Low Speed Range. SAE Technical Paper 2015-01-0755, 2015, doi:10.4271/2015-01-0755.

[7] Dingle, S. F.; Cairns, A.; Zhao, H.; Williams, J.; Williams, O.; Ali, R.: Lubricant Induced Pre-Ignition in an Optical SI Engine. SAE Technical Paper 2014-01-1222, 2014,doi: 10.4271/2014-01-1222.

[8] Lauer T. et al.: Model Approach for Pre-Ignition Mechanisms. MTZ worldwide, Vol. 75, Issue 1, pp.44-49 (2014).

[9] Kuboyama, T.; Moriyoshi, Y.; Morikawa, K.: Visualization and Analysis of LSPI Mechanism Caused by Oil Droplet, Particle and Deposit in Highly Boosted SI Combustion in Low Speed Range. SAE Int. J. Engines 8 (2), 2015, S. 529–537,doi: 10.4271/2015-01-0761.

[10] Luef, R.; Grabner, P.; Eichlseder, H.; Martin, C. et al.: Development of New Test Procedure to Determine Fuel and Oil Impact on Irregular Combustion Phenomena with Focus on Highly Boosted Downsized S.I. Engines. in: 23rd Aachen Colloquium Automobile and Engine Technology 2014, p. 1169-1204. Aachen, 2014.

[11] Takeuchi, K.; Fujimoto, K.; Hirano, S. and Yamashita, M.: Investigation of Engine Oil Effect on Abnormal Combustion in Turbocharged Direct Injection - Spark Ignition Engines. SAE Int. J. Fuels Lubr. 5(3):2012, doi:10.4271/2012-01-1615.

[12] Luo, X.; Teng, H.; Hu, T.; Miao, R.; Cao, L.: An Experimental Investigation on Low Speed Pre-Ignition in a Highly Boosted Gasoline Direct Injection Engine. SAE Int. J. Engines 8 (2), 2015, S. 520–528,doi: 10.4271/2015-01-0758.

[13] Zahdeh, A., Rothenberger, P., Nguyen, W., Anbarasu, M. et al.: Fundamental Approach to Investigate Pre-Ignition in Boosted SI Engines. SAE Int. J. Engines 4(1):246-273, 2011, doi:10.4271/2011-01-0340.

[14] Inoue, T. et al.: Abnormal Combustion in a Highly Boosted SI Engine - The Occurrence of Super Knock. SAE 2012-01-1141 (2012).

[15] Gohl, M.; Brandt, S.; Wittler, M.; Budde, M. et al., Influence of the Mixture Formation on the Lubrication Oil Emission of Combustion Engines. SAE Int. J. Fuels Lubr. 3(1):733-744, 2010, doi:10.4271/2010- 01-1275.

[16] Luef, R. 2015. Entwicklung einer Prüfmethode zur Bestimmung des Öleinflusses auf irreguläre Verbrennungsphänomene bei hochaufgeladenen DI-Ottomotoren. Dissertation, Technische Universität Graz.

[17] https://iolitec.de/en/products/ionic_liquids/catalogue, accessed 14 October 2020

[18] S. Palaveev and M. Mager, "Vorentflammung in Ottomotoren II," Abschlussbericht über das FVV-Vorhaben Nr.1051, 2014.

[19] Chauveau, C., Halter, F., Lalonde, A., Gökalp, I., “An Experimental Study on the Droplet Vaporization: Effects of Heat Conduction through the Support Fiber”, In. ILASS Technical Paper 4-1, 2008.

[20] Nomura, H. and UJiie, Y., “Experimental Study on high-pressure Droplet Evaporation using Microgravity Conditions”, In: Proceedings of the 26th Symposium (International) on Combustion, pp. 1257-1273, 1996.

[21] Tanaka, J.,”Visualization of lubricating oil droplets near ring crevice on pre-ignition of super charged SI engine”, 15th Conference “The Working Process of the Internal Combustion Engine”, September 24th/25th, 2015.

[22] Tanaka, J.,”Visualization of lubricating oil droplets from piston crown on pre-ignition of super charged SI engine”, 16th Conference “The Working Process of the Internal Combustion Engine”, September 28-29, 2017.

[23] Siemens: Methodology STAR-CD Version 4.30, 2017.

[24] Zöbinger, N. and Lauer, T., “Numerical Investigation of the Influence of Oil Dilution on the Ability to Initiate a Pre-Ignition Combustion,” SAE Int. J. Advances & Curr. Prac. in Mobility 2(4):1935-1962, 2020, doi:10.4271/2020-01-0611.

[25] ASTM D86, Standard Test Method for Distillation of Petroleum Products, 5.01 Philadelphia, PA: American Society for Testing Materials), 237-242.

[26] DIN EN ISO 3405, “Petroleum and Related Products from Natural or Synthetic Sources - Determination of Distillation Characteristics at Atmospheric Pressure (ISO/DIS 3405:2017)”.

[27] Reid, R.C., Prausnitz, J.M., and Poling, B.E., The properties of Gases and Liquids 4th Edition (New York: McGraw-Hill, Inc., 1987).

[28] Fredenslund, A., Jones, R.l., and Prausnitz, J.M., “Group-Contribution Estimation of Activity Coefficients in Nonideal Liquid Mixtures,” AIChE Journal 21:1086-1099, 1975.

[29] VDI-Gesellschaft Verfahrenstechnik und Chemieingenieurwesen, „VDI-Warmeatlas,” 11.Edition, Springer-Verlag Berlin Heidelberg, 2013.

[30] National Institute of Standards and Technology, NIST Chemistry WebBook, SRD 69, accessed August 2019, https://webbook.nist.gov/chemistry/fluid/.

[31] Lide, D.R., CRC Handbook of Chemistry and Physics (Boca Raton, FL: CRC Press, 2005).

[32] DIN 51581: Testing of Petroleum Products – Determination of Evaporation Loss.

[33] Reitz, R.D., Diwakar, R., “Effect of drop break-up on fuel sprays.” SAE Technical Paper 860469, 1986, doi:10.4271/860469.

[34] J.C.G. Andrae, P. Björnbom, R.F. Cracknell, G.T. Kalghatgi, Autoignition of toluene reference fuels at high pressures modeled with detailed chemical kinetics, Combust. Flame. 149 (2007) 2–24.

[35] J. Andrae, D. Johansson, P. Björnbom, P. Risberg, G. Kalghatgi, Co-oxidation in the auto-ignition of primary reference fuels and n-heptane/toluene blends, Combust. Flame. 140 (2005) 267–286.

[36] N. Blin-Simiand, F. Jorand, K. Keller, M. Fiderer, K. Sahetchian, Ketohydroperoxides and ignition delay in internal combustion engines, Combust. Flame. 112 (1998) 282–287.

[37] Hirschfelder JO, Curtiss CF (1949) Proc Combust Inst 3:121–127.

[38] Reid RC, Prausnitz JM, Poling BE (1989) The properties of gases and liquids. McGraw-Hill.

[39] G. Latini, G. Di Nicola, M. Pierantozzi, A Critical Survey of Thermal Conductivity Literature Data for Organic Compounds at Atmospheric Pressure and an Equation for Aromatic Compounds, Energy Procedia. 45 (2014) 616 – 625.

[40] A. Bondi, Estimation of Heat Capacity of Liquids, Ind. Eng. Chem. Fundam. 5 (1966) 442–449.

[41] L. Riedel, Kritischer Koeffizient, Dichte des gesättigten Dampfes und Verdampfungswärme. Untersuchungen über eine Erweiterung des Theorems der übereinstimmenden Zustände., Chemie Ing. Tech. 12 (1954) 679–683.

[42] Stauch R, Lipp S, Maas U (2006) Detailed numerical simulations of the auto-ignition of single n-heptane droplets in air Combustion and Flame 145 (3) 533-542.

[43] U. Maas, J. Warnatz, Ignition processes in hydrogen-oxygen mixtures, Combust. Flame 74 (1988) 53–69.

[44] Deuflhard P, Hairer E, Zugck J (1987) Numerische Mathematik 51:501–516

[45] Morgan, N., Smallbone, A., Bhave, A., Kraft, M., Cracknell, R., Kalghatgi, G.: „Mapping surrogate gasoline compositions into RON/MON space“. Combustion and Flame 157, pp.1122-1131, 2010.

[46] Andrae, J.C.G.,“HCCI experiments with toluene reference fuels modeled by a semidetailed chemical kinetic model“, Combustion and Flame 155 (2008), 696 712.

[47] Kalghatgi, G. T., Bradley, D.: „Pre-ignition and ‚super-knock‘ in turbo-charged spark-ignition engines“. International Journal of Engine Research, Vol. 13(4), pp. 399-414, 2012.

[48] Rossegger, B., Schneider, M., Leis, A., Engelmayer, M., and Wimmer, A. 2019. New Approaches to Lube Oil Consumption Measurement Based on the Tracer Method. In SAE Technical Paper Series. SAE Technical Paper Series. SAE International400 Commonwealth Drive, Warrendale, PA, United States. DOI=10.4271/2019-01-0077.

[49] Hommelwerke GmbH: Rauheitsmessung Theorie und Praxis; VS-Schwenningen, 1992.

[50] R. Ernst, R. Friedfeldt, S. L. Hons, D. Lloyd-Thomas, P. Phlips, R. Russell and T. Zenner, "The New 3 Cylinder 1.0L Gasoline Direct Injection Turbo Engine from Ford," 20th Aachen Colloquium Automobile and Engine Technology, pp. 59-60, 2011.

[51] Dahnz, C., Han, K.-M., Spicher, U., Magar, M., Schiessl, R., and Maas, U. 2010. Inves-tigations on Pre-Ignition in Highly Supercharged SI Engines. SAE Int. J. Engines 3, 1, 214–224.

[52] S. Hirano, M. Yamashita, K. Fujimoto and K. Kato, "Investigation of Engine Oil Effect on Abnormal Combustion in Turbocharged Direct Injection - Spark Ignition Engines (Part 2)," SAE International, doi:10.4271/2013-01-2569, 2013.

[53] A. Zahdeh, P. Rothenberger, W. Nguyen, M. Anbarasu, J. Schaefer, S. Schmuck-Soldan and T. Goebel, "Fundamental Approach to Investigate Pre-Ignition in Boosted SI Engines," SAE International Journal of Engines, Vol. 4, No. 1 (2011), pp. 246-273, doi:10.4271/2011-01-0340.

[54] Y. Okada, S. Miyashita, Y. Izumi and Y. Hayakawa, "Study of Low-Speed Pre-Ignition in Boosted Spark Ignition Engine," SAE Int. J. Engines 7(2):2014, doi:10.4271/2014-01-1218.

[55] K. Morikawa, Y. Moriyoshi, T. Kuboyama, Y. Imai and T. Yamada, "Investigation and Improvement of LSPI Phenomena and Study of Combustion Strategy in Highly Boosted SI Combustion in Low Speed Range," SAE Technical Paper 2015-01-0756, doi:10.4271/2015-01-0756, 2015.

[56] S. Palaveev, "Untersuchungen zu den Ursachen von stochastischen Vorentflammungen bei aufgeladenen Ottomotoren," KIT, Diss. Forschungsberichte aus dem Institut für Kolbenmaschinen, ISBN: 978-3-8325-4705-9, 01/2018.

[57] S. Pritze and A. Döhler, "A contribution to better understanding the pre-ignition phenomenon in highly charged internal combustion engines with direct fuel injection," IAV, 4th Conference on Knocking in Gasoline Engines, Berlin, 2013, pp. 41–61.

[58] Z. Wang, H. Liu and R. D. Reitz, "Knocking combustion in spark-ignition engines," Progress in Energy and Combustion Science, 2017.

[59] M. Kassai, T. Shiraishi and T. Noda, "Fundamental Mechanism Analysis on the Underlying Processes of LSPI Using Experimental and Modeling Approaches," International Conference on Knocking in Gasoline Engines pp 89-111, 2017.

[60] S. Koch, F. P. Hagen, H. Kubach, A. Velji and T. Koch, "Impact of the Injection Strategy on Soot Reactivity and Particle Properties of a GDI Engine," SAE Technical Paper 2020-01-0392, 2020, doi:10.4271/2020-01-0392.

[61] Livengood, J. C., Wu, P. C.:” Correlation of Autoignition phenomena in internal combustion engines and rapid compression machines”. Symposium (international) on combustion, volume 5, 1955.

[62] Gülder, Ö. 1984. “Correlations of laminar combustion data for alternative S.I. Engine fuels”, SAE Paper 841000.

[63] K. Nishikawi, N. Hafnan.: „The Determatoin of thermal properties of engine co bustion chamber deposits “. SAE technical paper, 2000-01-1215, 2000.

[64] K. Li, Q. Liu, et al: „ Investigation of the carbon structure of naturally graphitized coals from Central Hunan, China, by density-gradient centrifugation, X-ray difraction, and high-resolution transmission electron microscopy”. International Journal of Coal Geology 232 (2020),1036285.

[65] X. Liang, Y. Wang and K. Wang et al. : „Experimental study of impact of lubricant-derived ash on oxidation reactivity of soot generated in diesel engines“. Proceeding of the combustion institute 000, pp. 1-8, 2020.

[66] Heiss, M., Lauer, T.: “Analysis of Pre-ignition Initiation Mechanisms using a Multi Cycle CFD-Simulation”. In: International Multidimensional Engine Modeling Uer's Group Meeting (IMEM), Detroit (2014).

7.2 Nomenclature

aTDCf	After Top dead center firing
BDC	Bottom dead center
BMEP	Brake mean effective pressure
BP	Boiling point
BSE	Backscattered electron
BTDC	Befor Top dead center
Cam	Camera
CDF	Cumulated density function
CHT	Conjugated heat transfer
CNG	Compressed Natural Gas
COP	Coil on plug
DDM	Discrete droplet method
DI	Direct injection
DOHC	Dual overhead camshaft
ECU	Engine control unit
EDX	Energy dispersive X-ray
EOI	End of injection
EV	Exhaust valve
GC	Gas chromatographic
HS	High speed
IFKM	Institut für Kolbenmaschinen
IGN	Ignition
INJ	Injector
IV	Inlet valve
IVC	Intake valve closed
LIF	Light induced fluorescence
LSPI	Low speed pre-ignition
MFB	Mass fraction burned
MON	Motor octane number
$p_{cyl\ [IG]}$	Cylinder pressure at ignition
$p_{cyl\ [max]}$	Maximum cylinder pressure
P_e	Effectiv Power
PI	Pre-ignition

PS	Pressure sensor
Rc	Critical radius [m]
RON	Research octane number
Rp	Particle radius [m]
RP	Rail pressure
SEM	Scanning electron microscope
SMD	Sauter mean diameter
SOI	Start of injection
SP	Spark plug
SPM	Solid particulate matter
T	Torque
T_{Air}	Air temperature at airbox
T_{CW}	Cooling water out temperature
TDC	Top dead center
TDC	Top dead center
TGA	Thermal gravimetric analysis
T_{Oil}	Oil temperature
TPA	Three pressure analysis
TRF	Toluene reference fuel
TS	Time step
VF	Volume fraction
λ	Air-fuel ratio exhaust gas

7.3 List of figures

7.4 List of tables

FVV

Bundesministerium für Wirtschaft und Energie

Forschungsnetzwerk Mittelstand

FÖRDERGEBER
FUNDING ORGANISATIONS

Bundesministerium für Wirtschaft und Energie
Federal Ministry for Economic Affairs and Energy

Arbeitsgemeinschaft industrieller Forschungsvereinigungen
Federation of Industrial Research Associations

FKM Forschung im VDMA

VDMA

KOOPERATIONEN
PARTNER ASSOCIATIONS

Forschungskuratorium Maschinenbau
Mechanical Engineering Research Federation

Verband Deutscher Maschinen- und Anlagenbau
Mechanical Engineering Industry Association

Forschungsvereinigung
Verbrennungskraftmaschinen e.V.
Research Association
for Combustion Engines

Lyoner Strasse 18
60528 Frankfurt am Main, Germany

T +49 69 6603 1345
F +49 69 6603 2345
info@fvv-net.de

www.fvv-net.de